Conditions of Protection Against Quench and Thermal Runaway of Conduction-Cooled High Temperature Superconducting Magnets

LUO XIJIE

Conditions of Protection Against Quench and Thermal Runaway of Conduction-Cooled High Temperature Superconducting Magnets

March 2022

LUO XIJIE

Department of Electrical Engineering
Kyoto University

Contents

Chapter 1 Introduction

1.1 Superconductivity

The superconductivity phenomenon was discovered by H. Kamerlingh Onnes in 1911. At that time, while measuring the electrical resistance of mercury, he observed the disappearance of direct current (DC) electrical resistance when the temperature was less than 4.2 K. This characteristic differs from those of metals, such as copper or silver, which have residual resistance at low temperatures. The new phenomenon was named superconductivity [1.1].

Superconductors (materials, such as mercury, in which the superconductivity phenomenon can occur) may be in a normal conducting state (with DC electrical resistance) or superconducting state (without DC electrical resistance) depending on the temperature. To transition a superconductor from a normal state to a superconducting state, it must be cooled to less than a specific temperature value called critical temperature, T_c. Moreover, two other critical parameters bound the superconducting state: critical magnetic field, H_c, and critical current density, J_c. These three critical parameters constitute the boundary between superconducting and normal conducting, as shown in Figure 1.1.

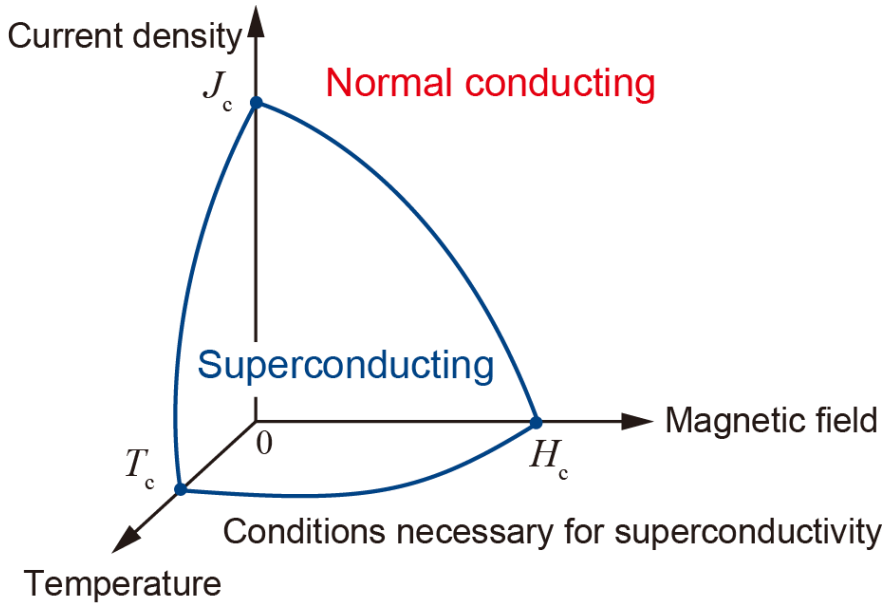

Figure 1.1 Boundary between superconducting and normal conducting.

In addition to the disappearance of electrical DC resistance, another defining characteristic of superconductivity is perfect diamagnetism, also known as Meissner effect. As shown in Figure 1.2, in a weak external magnetic field, when a superconductor is cooled below the transition temperature, T_c, the magnetic field is completely expelled from the superconductor.

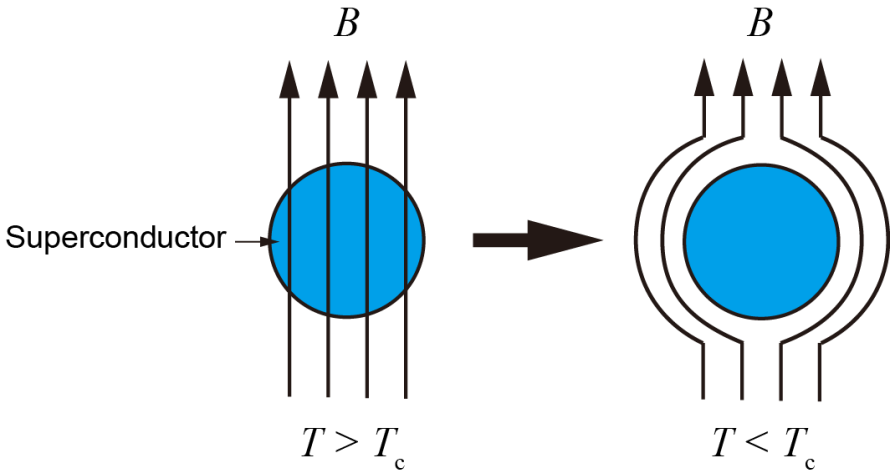

Figure 1.2 Meissner effect in superconductor.

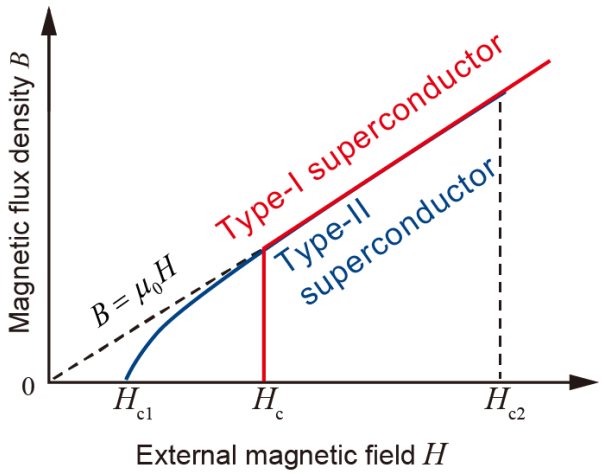

Figure 1.3 Magnetic flux density in type-I and type-II superconductors.

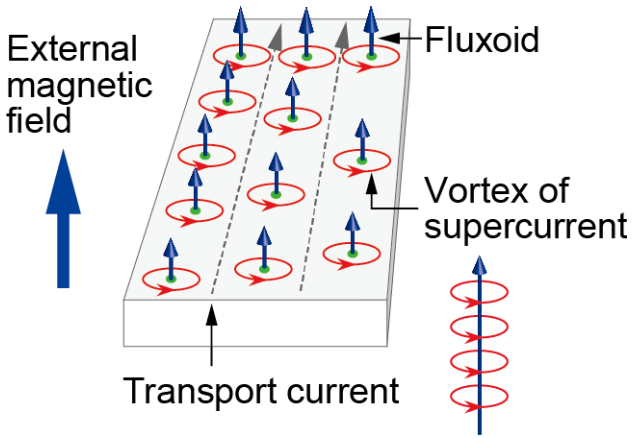

Figure 1.4 Mixed state.

Superconductors can be classified into type-I and type-II according to their magnetization characteristics. As shown in Figure 1.3, in type-I superconductors, the magnetic flux density (B) is zero when the external magnetic field, H, is less than H_c because of the Meissner effect. However, when H exceeds H_c, superconductivity is destroyed, and the superconductor exhibits the same electrical resistance characteristics as normal conductors. In contrast, in type-II superconductors, two critical fields exist: lower critical field, H_{c1}, and upper critical field, H_{c2}. When the external magnetic field is less than H_{c1}, the magnetic flux density of the superconductor is completely expelled due to the Meissner effect. When the external magnetic field exceeds H_{c1} but is less than H_{c2}, the flux line appears, as shown in Figure 1.4. Under this condition, the superconducting state coexists with the normal conducting state in a superconductor; this is called mixed state, and the flux lines are referred to as fluxoids. The number of fluxoid increases with the external magnetic field, and superconductivity is destroyed at an upper critical field, H_{c2}, at which fluxoids reach the highest density. Slightly lower than H_{c2}, there is irreversibility field H^* (not shown in Figure 1.3), at which the critical current density goes to zero. Type-I superconductors are not suitable as magnet conductor materials because of their low H_c value, *i.e.*, typically less than ~0.1 T. Accordingly, the superconductors discussed in the following sections of this thesis are all type-II superconductors.

1.2 Magnet-Grade Superconductor

This study focuses on superconductors that can be used in superconducting magnets. In the manufacture of magnets, superconductors should satisfy rigorous magnet specifications and should be readily available commercially. Magnet-grade superconductors have several typical key problems that must be resolved [1.2]:

mechanical integrity, operational reliability, and protection. First, during operation, the magnet must be structurally strong to withstand large magnetic forces. Operational reliability means that the magnet must reach and maintain its operating point (operating current, magnetic field, etc.). Finally, for protection, in the event that the magnet accidentally returns to its normal state, such change must be detected and protected (*i.e.*, remain undamaged). Currently, most magnet-grade superconductors are metallic.

1.2.1 Conventional Metallic Superconductor

At the temperature of liquid helium (4.2 K), numerous metals and alloys can transition to a superconducting state. However, over the years, only two materials have been regarded as magnet-grade superconductors: niobium–titanium (Nb–Ti) (Figure 1.5) and niobium–tin (Nb_3Sn) (Figure 1.6). The critical temperature of Nb–Ti superconductor is typically 9.6 K, and its critical magnetic flux density is 11.5 T at the temperature of liquid helium [1.3]. Depending on the applied field, the critical current density in Nb–Ti superconductor at 4.2 K may range from hundreds to several thousands of amperes per square millimeter [1.3], rendering it suitable for some magnets used in magnetic resonance imaging (MRI), particle accelerators, and maglev trains. In contrast, Nb_3Sn has higher critical temperature and critical magnetic flux density, which can be up to 18.3 K and 30 T, respectively [1.4]. Niobium–tin is prospected to be used for magnets producing a high field because of its higher critical magnetic flux density than Nb–Ti.

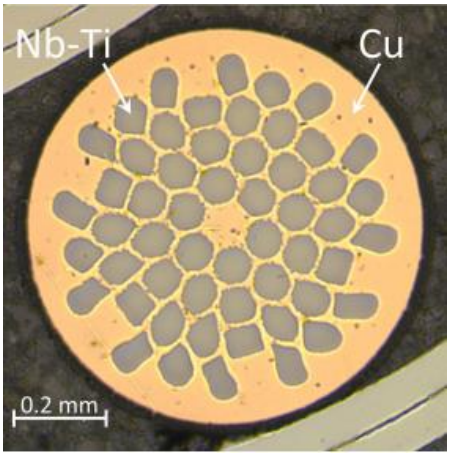

Figure 1.5 Cross-sectional image of Nb–Ti wire [1.3].

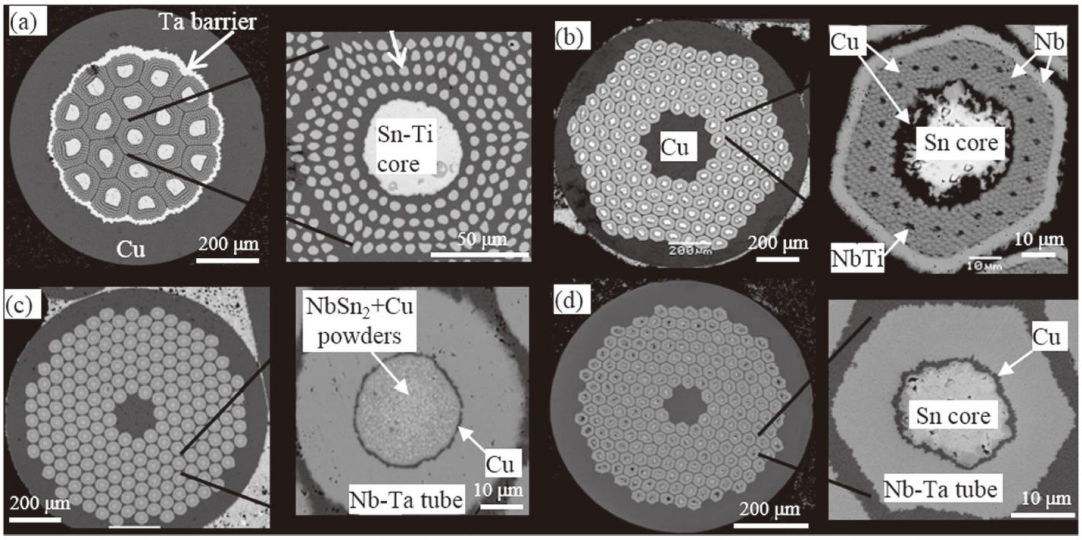

Figure 1.6 SEM images of cross-sections of (a) single-barrier internal-tin, (b) rod-restack-process, (c) powder-in-tube, and (d) tube-type Nb_3Sn strands [1.4] © 2017 IOP Publishing Ltd.

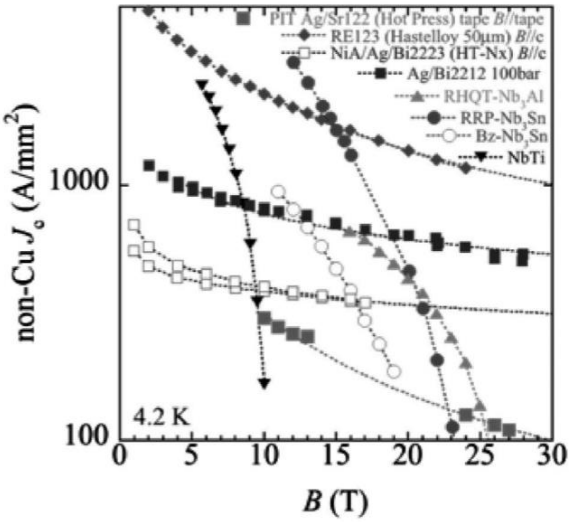

Figure 1.7 Critical current density vs magnetic field of typical magnet-grade superconductors at 4.2 K [1.5].

In recent years, high-temperature superconductors (HTSs), such as $Bi_2Sr_2CaCu_2O_{8+\delta}$ (Bi-2212) and $Bi_2Sr_2Ca_2Cu_3O_{10+\delta}$ (Bi-2223), which can be in a superconducting state at several tens of kelvins, have received considerable attention. As shown in Figure 1.7, Bi-2212 and Bi-2223 are expected to have high current density at 4.2 K; the critical current density is 1000 A/mm^2 in a magnetic field of several tesla. Typically, Bi-2212 and Bi-2223 are fabricated by the power-in-tube method [1.6], [1.7] and can have a round or tape shape, as shown in Figure 1.8.

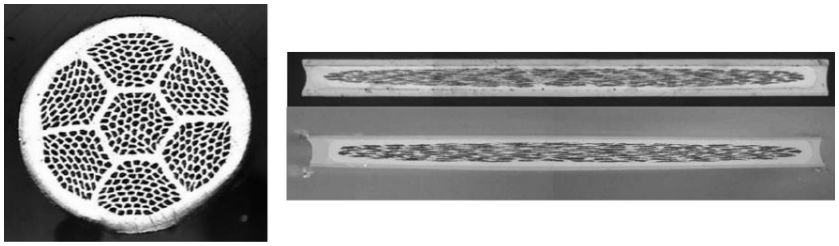

(a) (b)

Figure 1.8 Cross-sectional views of Bi-2212 and Bi-2223: (a) Bi-2212 round wire before heat treatment [1.7] © 2007 IEEE; (b) Reinforced Bi-2223 tapes [1.8] © 2009 IEEE.

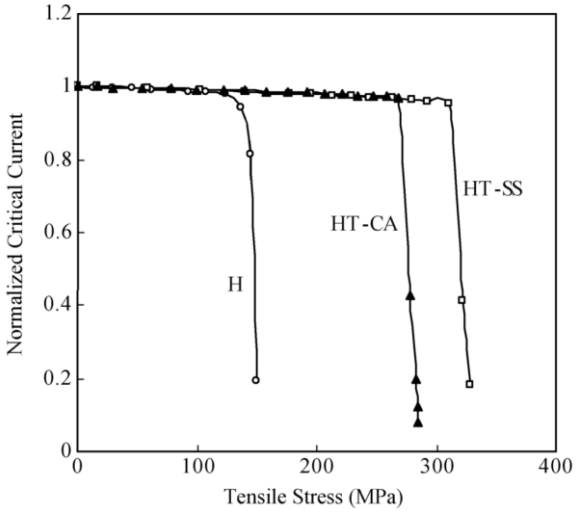

Figure 1.9 Normalized critical current of Bi-2223 as function of tensile stress at 77 K (Type H: original Bi-2223 tape; Type HT-CA: copper alloy-reinforced Bi-2223 tape; Type HT-SS: stainless steel-reinforced Bi-2223 tape) [1.8] © 2009 IEEE.

However, tensile stress is a concern in the use of Bi-2212 or Bi-2223. As shown in Figure 1.9, the normalized critical current rapidly drops when the tensile stress exceeds some certain values in the range 100–400 MPa. Recently, some stable, predictable, and training-free Bi-2212 coils have been fabricated [1.9]. Nevertheless, strain control remains an important task in a magnet wound with Bi-2212 and Bi-2223 to avoid critical current degradation.

1.2.2 Rare-Earth Barium Copper Oxide Superconductor

Rare-earth barium copper oxide superconductors (REBCO), including yttrium barium copper oxide (YBCO) and gadolinium barium copper oxide, are attractive

HTSs. As shown in Figure 1.10, their critical temperature and critical magnetic field are higher than those of other magnet-grade superconductors. Compared with low T_c superconductors, such as Nb–Ti, or high T_c superconductors, such as Bi-2212 and Bi-2223, REBCO superconductors have high critical current density (over 1000 A/mm^2) at temperature of liquid helium (4.2 K) even in high external magnetic fields (several tens of tesla), as shown in Figure 1.7.

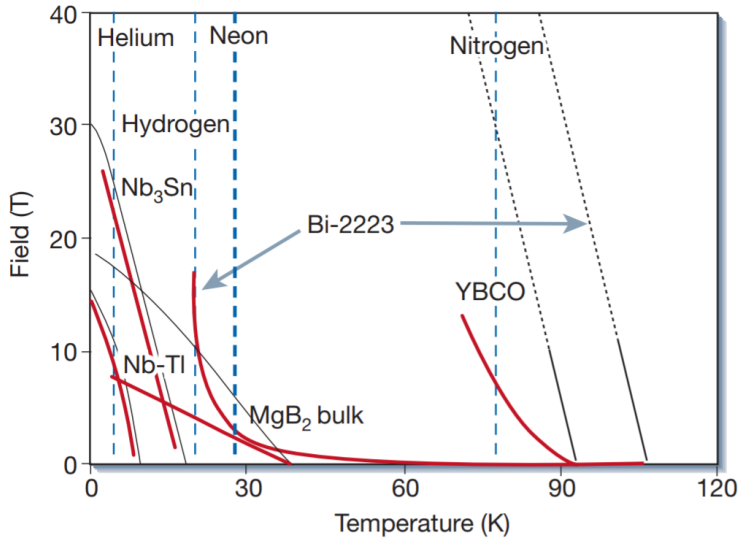

Figure 1.10 Magnetic field-temperature diagram for Nb–Ti, Nb_3Sn, MgB_2, Bi-2223 and YBCO. The upper critical field H_{c2} at which bulk superconductivity is destroyed is indicated in black, while the irreversibility field H^* at which the bulk critical current density goes to zero is indicated in red [1.10] © 2001 Macmillan Magazines Ltd.

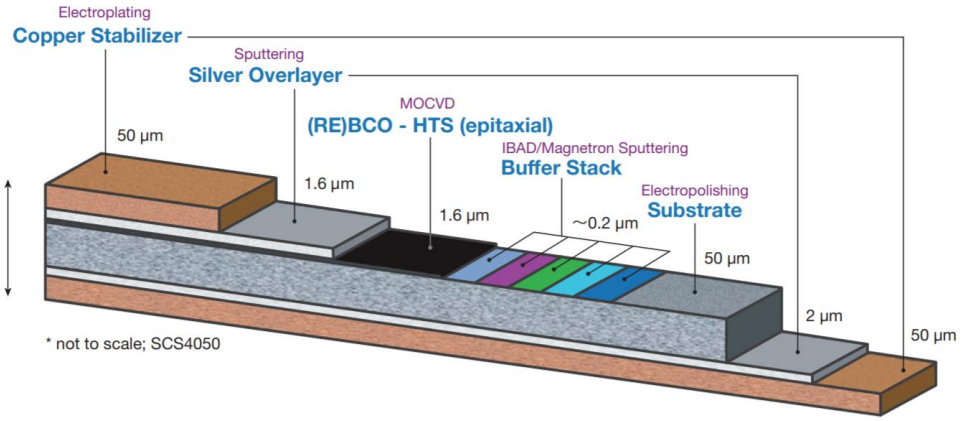

Figure 1.11 Structure of REBCO coated conductor produced by SuperPower Inc. [1.11].

Typical REBCO coated conductors have a multilayered structure, as shown in Figure 1.11. First, a substrate (mainly made by Hastelloy®) with a thickness of several tens of micrometers is prepared. On the substrate, a high-textured buffer layer (*e.g.*, MgO) is fabricated using ion beam-assisted deposition technology. Then, the superconducting layer produced by REBCO is used. Fujikura Ltd. fabricates this layer by pulsed laser deposition technology with the original hot-wall heating system [1.12]. In contrast, SuperPower Inc. utilizes metal organic chemical vapor deposition technology [1.11]. The superconducting layers produced by these two companies are similar in thickness, *i.e.*, 1–2 μm. A thin protective layer made of Ag, typically 1–2 μm thick, is provided on the superconducting layer. Around the structure, a copper stabilizer is fabricated by electroplating, varying from several to tens of micrometers. Superconducting magnets wound with REBCO coated conductors are the focus of this study because of their potential to carry considerable amounts of currents at low temperatures and high fields.

1.3 Superconducting Magnets

An electromagnet is a type of magnet whose magnetic field is produced by the flow of current in a coil. Because people can delicately control the magnetic field by regulating the operating current, electromagnets, such as motors, generators, and hard disks, are widely used in physics research, manufacturing industry, and medical care. Most of the electromagnets are made of normal conductors, such as copper (a normal conducting magnet), which is easily obtainable and well-conductive. However, because of Joule heating, the current density in such normal conducting magnets is limited (*e.g.*, some normal conducting magnets at the European Council for Nuclear Research are designed with a current density of ~5 A/mm^2 [1.13]). This means that to produce a high magnetic field, an electromagnet made of a normal conductor has to be enormous in size. In addition to its huge size, energy loss is another problem that occurs in a normal conducting magnet. In most normal conducting magnets, such as motors and generators, the electric energy is lost to the surrounding environment through Joule heating.

In some fields, such as high-energy physics and medical care, electromagnets made of superconductors (*i.e.,* superconducting magnets) are used owing to their high current density with no power consumption (except cooling power). As shown in Figure 1.7, the critical current in superconductors, such as Nb–Ti and REBCO, can be several hundreds of amperes per square millimeter (depending on the external magnetic field). This means that to produce the same magnetic field, the size of the superconducting magnet may be considerably smaller than that of the

normal conducting magnet. Because superconducting magnets have no resistance and power consumption, their use can save energy. For example, some superconducting magnets used for MRI are operated in a persistent current mode. Because it has no resistance, the current in such a superconducting magnet does not decay, and an external power supply is unnecessary to produce a magnetic field continuously.

1.3.1 Cooling Methods

Until 1990, all superconducting magnets were *wet magnets* (*i.e.*, using liquid coolants) and cooled by liquid helium (at 4.2 K) [1.2]. The discovery of HTSs and advances in cryocooler technology have rendered magnet cooling using a dry cryogenic system (dry magnet) reliable. The cooling methods for superconducting magnets can be classified into two types based on the heat transfer difference: convective (for wet magnets) and conductive (for dry magnets). Furthermore, convective cooling can be categorized as bath-cooled and force-cooled. Bath-cooled magnets are partly or entirely immersed in cryogens, such as liquid helium, liquid hydrogen, and liquid nitrogen. In force-cooled magnets, the coolants (such as liquid/gas helium and hydrogen) are forced through the winding. In the conductive cooling method, a refrigerator (cryocooler) designed to reach the cryogenic temperature is employed.

Figure 1.12 Photograph of GM cryocooler. [1.14] ©2022 SHI Cryogenics Group.

In conductive cooling, a Gifford-McMahon (GM) cryocooler is widely used [1.15], as shown in Figure. 1.12. Inside the GM cryocooler, a cooling agent moves back and forth inside a cylinder to cause the adiabatic expansion of the refrigerant gas (usually helium) to generate chill. In a vacuum cryostat, the magnet is cooled by thermal conduction, *i.e.*, the heat of the superconducting coil is transferred through current leads, supporters to the GM cryocooler. Compared with convective cooling, the conductive cooling method using a cryocooler is easier to set up and maintain. The amount of helium used in conductive cooling is considerably smaller than that used in conventional convective cooling using liquid helium. In this study, conduction cooling is applied to all experiments using the GM cryocooler.

1.3.2 Thermal Stability and Normal Transition

In this thesis, "thermal stability" is defined as the ability to maintain a superconducting magnet in a superconducting state to resist thermal disturbance or temperature increase. As shown in Figure 1.1, to maintain the superconducting state, the current, magnetic field, and temperature must be less than the critical values. The transition from the superconducting state to the normal conducting state (*i.e.*, normal transition) can only occur when one of the three aforementioned parameters accidentally exceeds its critical value. In a superconducting magnet operated at a certain current, the temperature increase must be greater than the sudden current/magnetic field increase. The increase in temperature may be caused by the frictional energy resulting from the conductor motion under the Lorentz force, deterioration of cooling, beam injection in an accelerator system, and so on.

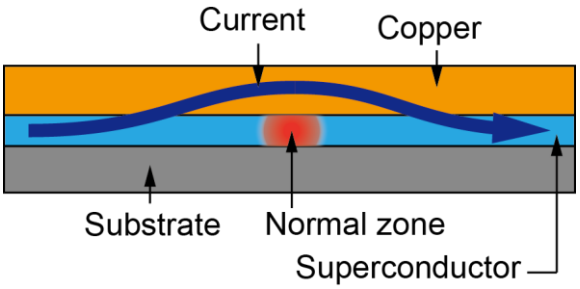

Figure 1.13 Current distribution in coated conductor with normal zone.

Figure 1.13 shows the current distribution when normal transition occurs in a coated conductor with a simple structure. When a localized increase in temperature accidentally occurs, a normal zone may appear on the superconductor. Because of the high normal zone resistance of the superconductor, the current, which can be several hundreds of amperes per square millimeter, may flow in the copper layer and induce a considerable amount of Joule heating power. When this heating power

is larger than the cooling power, the temperature of the superconductor can rise continuously. Such a phenomenon of irreversible transition from the superconducting state to the normal conducting state is called "quench" or "thermal runaway" (the differences between the two are introduced in a later section).

For an adiabatic superconducting magnet (such as a conduction-cooling superconducting magnet), a useful design parameter, called "stability margin," is given by the following:

$$\Delta e_{\mathrm{h}} = \int_{T_{\mathrm{op}}}^{T_{\mathrm{c}}(I_{\mathrm{op}})} C(T)\mathrm{d}T, \tag{1.1}$$

where Δe_{h} is the maximum energy density that the superconductor can absorb to remain in the superconducting state; I_{op} and T_{op} are the operating current and temperature, respectively; and $T_{\mathrm{c}}(I_{\mathrm{op}})$ is the operating current according to the critical temperature. The REBCO coated conductor has a considerably higher critical temperature than low-temperature superconductors (LTSs), such as Nb–Ti. Hence, superconducting magnets wound with REBCO coated conductors are considered to be more stable than those wound with LTSs, as indicated by equation (1.1). Nevertheless, in a magnet wound with the coated conductor, quench is unavoidable. Because of the high current density in the superconducting magnet, Joule heating power can be considerable when normal transition occurs. Hence, to prevent the degradation of the superconducting magnet due to rising temperature, quench/thermal runaway detection and protection methods are necessary.

1.3.3 AC Loss

When the superconductor carries AC transport current or is in an AC external magnetic field, energy loss, called AC loss, occurs in the superconductor. This loss in superconductors can be classified into hysteresis loss, coupling loss, and eddy current loss according to the electromagnetic mechanism of generation.

1) Hysteresis loss

When transport current flows inside a type-II superconductor, the flux lines experience the Lorentz force due to magnetic fields, as shown in Figure 1.4. Usually, the flux lines are "pinned," for example, by grain boundaries. However, as the transport current or external magnetic field changes, the Lorentz force might exceed the pinning force, and the flux lines start to move perpendicular to the transport current or magnetic field. The energy dissipated in this process is referred to as hysteresis loss.

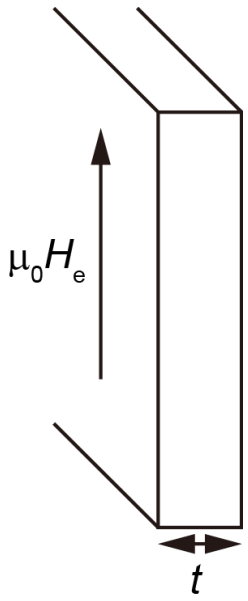

Figure 1.14 Infinitely large superconducting slab.

Consider an infinitely large superconducting slab with a thickness of t in an AC external magnetic field, H_e, parallel to both sides of the slab, as shown in Figure 1.14. According to the Bean model and Maxwell equations, the hysteresis loss in the slab with constant critical current density, J_c, can be given as follows [1.1]:

$$Q_{h,slab} = \frac{4\mu_0}{3}\frac{H_e^3}{J_c t}, H_e < \frac{J_c t}{2}, \quad (1.2)$$

$$Q_{h,slab} = t\mu_0 J_c \left(H_e - \frac{J_c t}{3}\right), H_e > \frac{J_c t}{2}, \quad (1.3)$$

where $Q_{h,slab}$ is the hysteresis loss per unit volume of slab per cycle. The equations indicate that the hysteresis loss is determined by the amplitude of the external magnetic field and is independent of the changing rate of the magnetic field. In this case, a region where $H_e > \frac{J_c t}{2}$ has practical importance, the hysteresis loss per unit volume of this region can be reduced in proportion to the slab thickness. In the case of REBCO coated conductors, it is reported that the hysteresis loss can be decreased by dividing the superconductor layer into several filaments (multifilament coated conductor) [1.16]–[1.19], as shown in Figure 1.15.

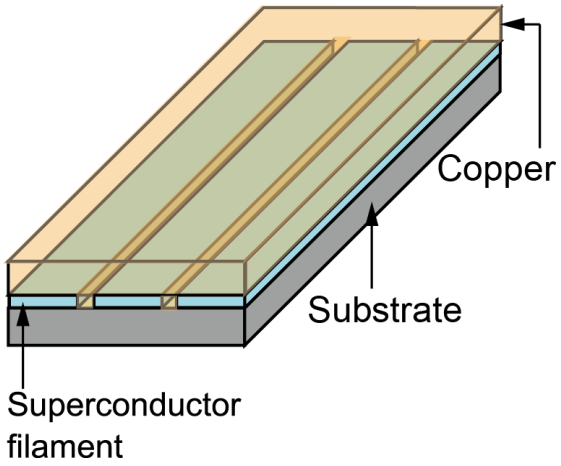

Figure 1.15 Multifilament coated conductor.

2) Coupling loss

When superconductors are embedded in normal conductors, such as those shown in Figure 1.6, current flow may be induced in the normal conductor and superconducting filaments in an AC magnetic field. In the filamentary region, the shielding current flows through a loop consisting of the normal conductor and filaments, resulting in ohmic loss in the normal conductor, *i.e.*, coupling loss.

3) Eddy current loss

When the conductor is exposed to an alternating magnetic field, current flow is induced in the normal conductor, *e.g.*, in the protective metal layer in the REBCO coated conductor. These flows cause eddy current loss.

1.3.4 Shielding-Current-Induced Field

In a tape-shaped conductor, such as REBCO coated conductor, the shielding current flows through the wide face when an alternating magnetic field perpendicular to the wide face exists, as shown in Figure 1.16. Such shielding current induces an unexpected magnetic field and affects the accuracy of the designed field. It is considered that the shielding-current-induced field can be generated in a multifilament coated conductor because the shielding current loops are small, as shown in Figure 1.16(b).

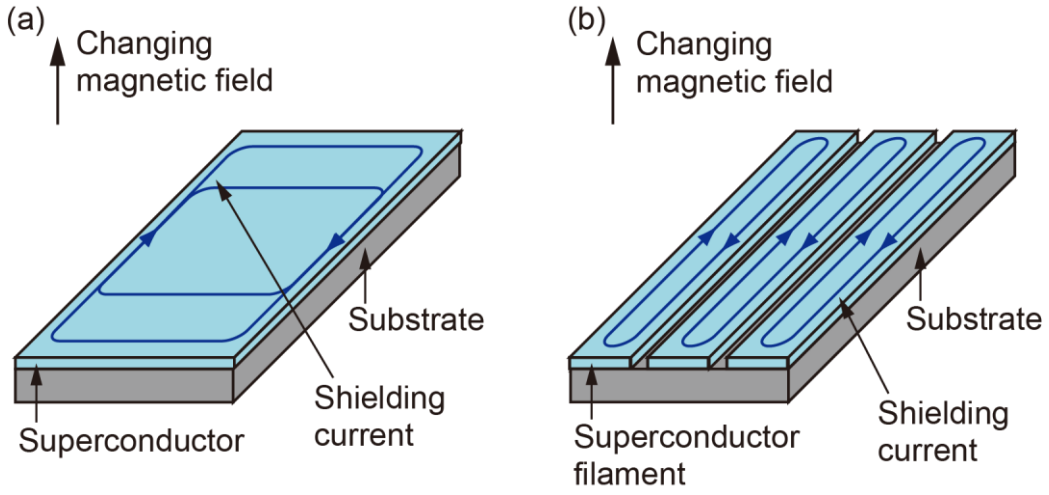

Figure 1.16 Shielding current in coated conductor without copper layer: (a) monofilament; (b) multifilament.

1.4 Background and Objectives

1.4.1 Quench/Thermal Runaway in Superconducting Magnets

The irreversible normal transition in which the temperature rises continuously if no protection is provided is called quench or thermal runaway. In this thesis, "quench" represents the normal transition induced by some local or transient thermal disturbance. Moreover, "thermal runaway" represents the normal transition induced by continuous Joule heating, which lasts for a relatively long period.

Based on equation (1.1), the critical temperature of HTSs (*e.g.*, T_c of REBCO coated conductor is ~90 K) is considerably higher than that of LTSs (*e.g.*, T_c of Nb–Ti is ~10 K). Hence, the stability margin of a magnet wound with high-temperature superconductor (HTS magnet), is substantially greater than that of a magnet wound with low temperature superconductors (LTS magnet). For example, in LTS magnets, AC loss can possibly induce quench/thermal runaway, whereas in HTS magnets, quench/thermal runaway is not easily induced because the AC loss is not sufficiently high to increase the superconductor temperature to its critical level. However, quench occurs in real coils wound with REBCO coated conductor and is difficult to predict. Some of the typical disturbances are listed in Table 1.1.

TABLE 1.1
TYPICAL DISTURBANCES

Type	Disturbances	Predictable or not
Transient	Friction under electromagnetic force	not
	Cracking of resin	not
	Flux jump	not
	Beam injection	not
Continuous	AC loss	predictable
	Joule heating near injection part	predictable
	Joule heating at local defects	not
	Radiation in some fusion magnets	predictable

Although disturbances can be transient or continuous, once quench/thermal runaway occurs in an HTS magnet, the temperature of the normal zone rapidly rises because of the high current density. In other words, the protection against the quench induced by transient disturbances and that against the thermal runaway induced by continuous disturbances are virtually the same. Moreover, because a considerable amount of current flows through the copper layer after quench/thermal runaway, the protection of magnets wound with monofilament coated or multifilament coated conductors must be the same.

Recently, the use of non-insulating windings (conductors are conductive among the turns of a coil) in which the current can bypass the normal zone through adjacent turns is proposed to solve the problem of quench/thermal runaway in HTS magnets [1.20]–[1.22]. However, non-insulating windings are not always applicable to certain types of magnets, such as those that must be rapidly ramped up (*e.g.*, magnets for synchrotron [1.23] and MRI magnets equipped with gradient coils), in which the generation of magnetic fields is time-dependent.

Although there are studies on the behaviors of HTS magnets after quench or thermal runaway [1.24]–[1.27], whether the protections against quench and thermal runaway are the same is not clarified. This research, focusing on the turn-to-turn insulated HTS magnets, one objective of this research is to investigate and compare the conditions for the successful protection against quench and thermal runaway of monofilament and multifilament coated conductors.

1.4.2 Conventional Quench/Thermal Runaway Detection and Protection Method

A conventional detection and protection method widely applied to LTS magnets is shown in Figure 1.17. The idea is to transfer most of the stored energy in the coil ($LI^2/2$) into an external dump resistor connected across the magnet terminals. The detection and protection processes are as follows:

1) quench/thermal runaway is detected when the normal voltage across the coil exceeds a certain threshold (detection voltage, v_{th});
2) the circuit breaker is opened (a delay time, t_d, is necessary to activate the breaker);
3) current starts to flow through the external dump resistor and decays exponentially with a certain time constant (time constant τ = resistance of dump resistor (R)/inductance of coil (L)).

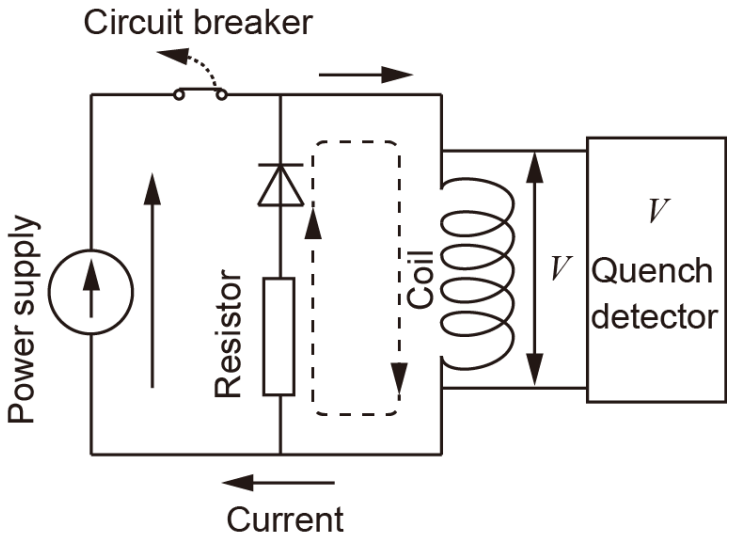

Figure 1.17 Magnet circuit for detect-and-dump active protection.

Because the normal zone is heated until the current in the coil decays to zero, the point of protection is to detect quench/thermal runaway at an early phase (low detection voltage) and quickly decrease the current (low time constant of current decay).

1.4.3 Applicability of Conventional Detection and Protection Method to HTS Magnets

Although there are differences on the characteristics (e.g. normal zone propagation velocity, thermal conduction, heat capacity, etc.) between REBCO coated conductor and low-temperature superconductor, the quench/thermal runaway

phenomenon between REBCO coated conductor and low-temperature superconductor should be essentially the same. In previous study, it is suggested that the degradation should not appear in a REBCO coil if the temperature after quench/thermal runaway can be kept under certain values [1.28], which is similar to the consideration of the protection against quench/thermal runaway in the magnets wound by low-temperature superconductor.

It is concerned that such conventional quench/thermal runaway detection and protection method may be not applicable to HTS magnets wound with REBCO coated conductors, because of the slow normal zone propagation velocity of REBCO coated conductors (a few tens of millimeter per second), which is extremely slower than that in LTS magnets (a few tens of meters per second) [1.29], [1.30]. Due to the slow normal zone propagation in HTS magnets, for the same monitored voltage, the normal zone in HTS magnets should be much smaller than that in LTS magnets, which means the resistance per unit length of normal zone in HTS magnets should be much higher than that in LTS magnets. In other words, for the same monitored voltage, the slow normal zone propagation results in high local temperature in HTS magnets [1.31], which makes the protection of HTS magnet be difficult.

Instead of detecting using voltage, some studies focusing on developing the detection method, e.g. detecting by temperature using optical fiber [1.32], [1.33] or low-temperature superconducting quench detectors (made by low-temperature superconductor) [1.34].

However, the systematical study on the protectable conditions (*i.e.*, conditions under which no degradation appears after quench/thermal runaway), when using the conventional method, is still insufficient. It is attractive if the conventional quench/thermal runaway detection and protection method is applicable because of its simplicity and well-established hardware.

In this research, such protectable conditions are systematically studied, to confirm the applicability of the conventional quench/thermal runaway detection and protection method:

1) the thresholds of the conditions (operating current, detection voltage, time constant of current decrease) for successful protection are determined;
2) the case studies of HTS magnets under the protectable conditions are performed.

1.4.4 Simulation of Quench/Thermal Runaway in High-Temperature Superconducting Magnets Using Short Sample

To determine the threshold of the successful protection of conduction-cooled HTS magnets using the conventional detection and protection method, quench/thermal runaway must be examined under various conditions. However, two problems must be resolved in investigating the conditions for protection using HTS coils. 1) Burning a number of expensive HTS coils is uneconomical, and 2) the preparation (manufacturing, winding, and so on) and cooling of large HTS coils are time-consuming.

In view of the slow propagation of the normal zone in HTS coils, this zone must be localized in a small part of the coil at the initial phase of quench/thermal runaway, as shown in Figure 1.18(a). In this case, the behaviors (temperature, voltage, *etc.*) of conductors at the normal zone must be similar to those of conductors in short stacks, as shown in Figure 1.18(b). By neglecting the effect of the normal zone transition in the transverse direction (among coil turns), Figure 1.18(b) can be simplified into Figure 1.18(c).

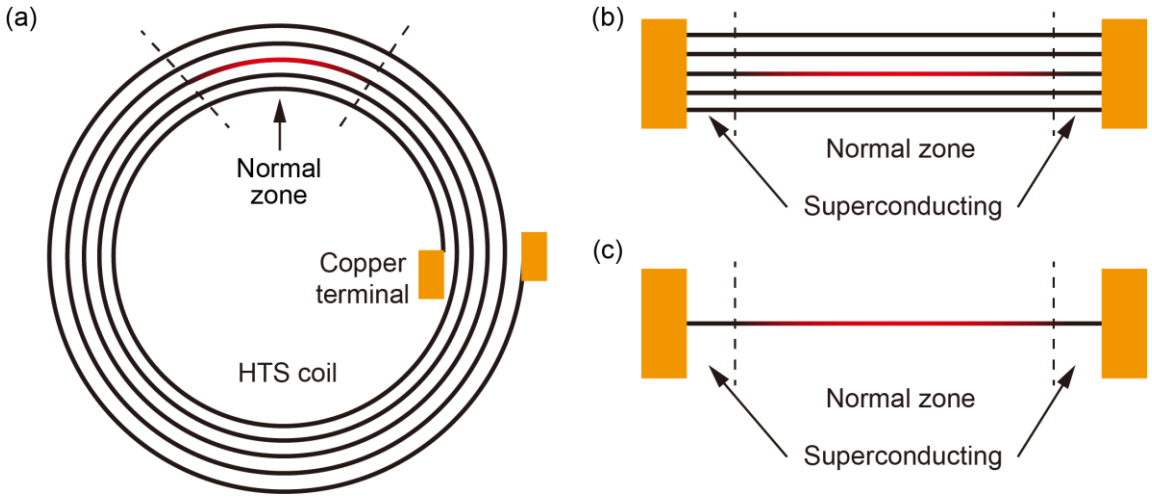

Figure 1.18 Normal zone in HTS coil and short conductor samples:
(a) pancake coil; (b) stack of short conductor; (c) single short conductor.

The cooling conditions of single short conductors must be worse than those of the conductors in coils or stacks. The latter can be cooled through the adjacent turns in the transverse direction. In contrast, the former cannot be cooled (when the sample is not fixed to a sample holder) or can only be cooled on one side (when the sample is fixed to a sample holder) in the transverse direction. Because of these differences in cooling conditions, the temperature in a single short sample must be

higher than those in coils using the same detection and protection conditions. In other words, the protectable conditions identified from the short-sample experiments must be on the safer side, *i.e.*, the temperature in real coils must be lower than that in short samples using the same detection and protection conditions.

1.4.5 Numerical Calculation of Detection and Protection Against Quench/Thermal Runaway of REBCO Coated Conductor

Based on the slow propagation of the normal zone in REBCO coated conductors, the short-turnaround short-sample experiments enabled the derivation of well-organized data regarding the protection of these conductors under various conditions. However, because the cooling conditions in real coils may differ from those in single-short samples (*e.g.*, the longitudinal/transverse thermal conduction shown in Figure 1.19), the thermal conduction effects observed in the short-sample experiments must be evaluated.

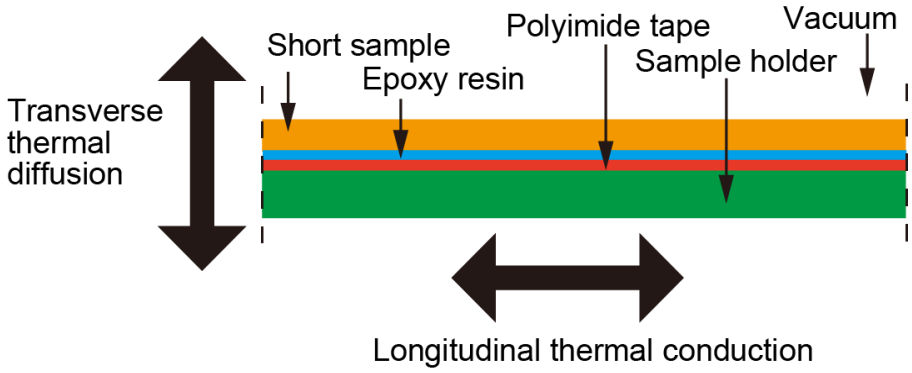

Figure 1.19 Construction of short sample across its thickness.

The cross-sectional area of a coated conductor is small (thickness: ~0.1 mm × width: several millimeters); hence, the temperature at the cross-section of the REBCO coated conductor may be assumed as uniform. Then, the temperature after quench/thermal runaway can be calculated using the following one-dimensional (1D) heat conduction equation considering the longitudinal (x direction) thermal conduction:

$$\gamma C \frac{\partial T}{\partial t} = \frac{\partial}{\partial x}\left(k \frac{\partial T}{\partial x}\right) + g, \qquad (1.2)$$

where T is temperature; x is the coordinate along the coated conductor; γC is the volumetric heat capacity (affected by the transverse thermal diffusion); k is the thermal conductivity; and g is the Joule heat generation at the normal zone. By considering the current-sharing model (current in copper (I_{Cu}) = operating current

(I_{op}) – critical current (I_c) when normal zone appears), the Joule heat generation and voltage can be calculated using the following equations:

$$g = \left[I_{op} - I_c(T)\right]^2 R(T), \tag{1.3}$$

$$V(T) = \left[I_{op} - I_c(T)\right] R(T). \tag{1.4}$$

Based on equations (1.2), (1.3), and (1.4), reproducing the quench/thermal runaway detection and protection of short samples is possible. This can be achieved by decreasing the operating current exponentially using a certain time constant when the total voltage exceeds the detection voltage. This paper discusses the relevance of short-sample experiments to real coils (focusing on thermal conduction/diffusion) using 1D numerical calculation.

1.4.6 Study Objectives

A second-generation HTS, also a REBCO coated conductor, is anticipated to be used in superconducting magnets owing to its high critical current density even in a high external magnetic field. Because REBCO coated conductors have a high critical temperature level, their stability margin can be considerable; nevertheless, the occurrence of normal transition (quench/thermal runaway) cannot be totally avoided. Due to the high current density, Joule heating may cause magnet degradation once normal transition occurs.

The conventional detection and protection method (detection using voltage and protection using a dump resistor), which is widely applied to LTS magnets, is attractive because of its simplicity and well-established hardware. However, in the case of HTS magnets with turn-to-turn insulation, the applicability of this conventional detection and protection method are unclear.

To clarify the applicability of the conventional detection and protection scheme to conduction-cooled HTS magnets, and to find the thresholds for the successful protection of HTS magnets with turn-to-turn insulation, short-sample experiments were designed. Because the normal zone must be located in a superconducting magnet wound with a REBCO coated conductor at the initial phase of quench/thermal runaway, the magnet behaviors (*e.g.*, voltage and temperature) during the protection process can be simulated using short-sample pieces instead of burning expensive coils.

The main objectives of this study are:

1) to demonstrate the applicability of the conventional detection and protection scheme to conduction-cooled HTS magnets with turn-to-turn

insulation by experiments using short monofilament samples;
2) to determine the conditions for successful quench detection and protection (detection voltage, time constant for current decrease, operating current, etc.) of conduction-cooled HTS magnets by experiments using short monofilament samples;
3) to verify whether a significant difference exists in the conditions of protection between monofilament and multifilament coated conductors;
4) to verify whether a significant difference exists in the conditions of protection between quench and thermal runaway;
5) to clarify the relevance of short-sample experiments to real HTS coils using 1D numerical calculation.

1.5 Thesis Outline

This thesis consists of the following parts.

In Chapter 2, the comparison of recent detection and protection methods against quench/thermal runaway is presented. The direct reasons for the superconductor's degradation during quench/thermal runaway detection and protection are discussed. The equations for the analysis of temperature rise and normal zone propagation are introduced.

In Chapter 3, the common experimental methods used in this thesis are introduced. A conduction-cooled cryostat was used to operate experiments using short REBCO coated conductor sample pieces (short-sample experiments). A field-programmable gate array (FPGA) module is used to monitor the voltage of samples and control the power supply output, simulating the quench detection and protection processes in a real magnet. The current-sharing model and the copper's resistivity–temperature relationship are combined to calculate the temperature of samples after the quench/thermal runaway.

In Chapter 4, the investigation of the conditions of protection against quench is elaborated. Under various conditions (*e.g.*, those related to operating current, detection threshold, and time constant of current decrease), well-organized data on hot-spot temperatures are derived. The hot-spot temperatures during the protection process were studied, focusing on four factors: operating current, time constant of current decrease, detection voltage, and copper thickness. In addition, the conditions for successful/failed quench detection and protection are experimentally studied.

In Chapter 5, the examination of the thermal runaway from a weak point (low critical current part) on REBCO coated conductor is discussed. The initiations of

thermal runaway in monofilament and multifilament coated conductors were compared. The thermal runaway experiments were conducted at various current values to identify the current threshold under which degradation does not occur after the thermal runaway. The protectable conditions against quench and thermal runaway were compared.

In Chapter 6, the relevance of short-sample experiments to real coils is elaborated. The influence of transverse thermal diffusion and longitudinal thermal conduction in the short-sample experiments is discussed using a numerical calculation based on the experimental results. The effect of short length is discussed based on the temperature distribution in the short-sample experiments and numerical calculation. The differences in degradation in the short-sample experiments and real coils are also discussed, focusing on the hot-spot temperature.

In Chapter 7, the study of factors that do not affect protection is presented. The factors affecting Joule heating are considered to dominate the hot-spot temperature during the protection process. The factors that are not supposed to affect Joule heating (such as the power of thermal disturbance, which induces quench) are experimentally confirmed not to affect the maximum hot-spot temperature.

[References]

[1.1] M. N. Wilson, Superconducting Magnets, Oxford, U.K.:Clarendon, 1983.

[1.2] Y. Iwasa, *Case Studies in Superconducting Magnets* 2nd ed. New York, NY, USA: Springer-Verlag, 2009.

[1.3] D. Patel, S. Kim, W. Qiu, M. Maeda, A. Matsumoto, G. Nishijima, H. Kumakura, S. Choi, and J. H. Kim, “Niobium-titanium (Nb-Ti) superconducting joints for persistent-mode operation”, *Sci. Rep.*, vol. 9, 2019, Art. no. 14287.

[1.4] X. Xu, “A review and prospects for Nb_3Sn superconductor development,” *Supercond. Sci. Technol.*, vol. 30, Aug. 2017, Art no. 093001.

[1.5] S. Awaji, “History and future prospect of practical superconducting material developments,” *J. Particle Accelerator Society of Japan*, vol. 16, no. 4, 2019(287-294).

[1.6] T. Shen, L. Ye, and H. Higley, “Strain control of composite superconductors to prevent degradation of superconducting magnets due to a quench: II. High-strength, laminated Ag-sheathed Bi-2223 tapes,” *Supercond. Sci. Technol.*, vol. 31, Nov. 2017, Art. no. 015012.

[1.7] K. Takahashi *et al.*, “Transport properties of Bi2212 round wires grown

in high magnetic fields," *IEEE Trans. Appl. Supercond.*, vol. 17, no. 2, Jun. 2007(3106-3108).

[1.8] N. Ayai *et al.*, "Electrical and mechanical properties of DI-BSCCO Type HT reinforced with metallic sheathes," *IEEE Trans. Appl. Supercond.*, vol. 19, no. 3, Jun. 2009(3014-3017).

[1.9] T. Shen *et al.*, "Stable, predictable and training-free operation of superconducting Bi-2212 Rutherford cable racetrack coils at the wire current density of 1000 A/mm^2," *Sci. Rep.* vol. 9, 2019, Art. no. 10170.

[1.10] D. Larbalestier, A. Gurevich, D. Feldmann, and A. Polyanskii, "High-T_c superconducting materials for electric power applications," *Nature* 414, 2001(368–377).

[1.11] SuperPower, Inc.: "Introduction of SuperPower Inc. and High Temperature Superconducting Wire" https://www.furukawa.co.jp/rd/review/fj136/fj136_05.pdf

[1.12] Fujikura, Ltd.: "Introduction of FUJIKURA RE-based HTS Wire" https://www.fujikura.co.jp/eng/products/newbusiness/superconductors/01/superconductor.pdf

[1.13] D. Tommasini, "Practical Definitions & Formulae for Normal Conducting Magnets" https://indico.cern.ch/event/683638/contributions/2801819/attachments/1563492/2533956/Magnet_analytical_design_formulae.pdf

[1.14] Sumitomo Heavy Industries, Ltd., Tokyo, Japan: "RDK-415D 4K Cryocooler Series" https://www.shicryogenics.com/product/rdk-408d2-4k-cryocooler-series/

[1.15] Sumitomo Heavy Industries, Ltd., Tokyo, Japan: "Cryocoolers" https://www.shi.co.jp/english/products/machinery/cold/index.html.

[1.16] N. Amemiya, N. Tominaga, R. Toyomoto, T. Nishimoto, Y. Sogabe, S. Yamano, and H. Sakamoto, "Coupling time constants of striated and copper-plated coated conductors and the potential of striation to reduce shieldingcurrent-induced fields in pancake coils," *Supercond. Sci. Technol.*, vol. 31, Jan. 2018, Art no. 025007.

[1.17] N. Amemiya, Y. Sogabe, S. Yamano, and H. Sakamoto, "Shielding current in a copper-plated multifilament coated conductor wound into a single pancake coil and exposed to a normal magnetic field," *Supercond. Sci. Technol.*, vol. 32, Oct. 2019, Art no. 115008.

[1.18] F. Grilli, and A. Kario, "How filaments can reduce AC losses in HTS coated conductors: a review," *Supercond. Sci. Technol.*, vol. 29, Jul.

2016, Art no. 083002.
[1.19] E. Pardo, M. Kapolka, J. Kováč, J. Šouc, F. Grilli, and A. Piqué, "Three-dimensional modeling and measurement of coupling AC loss in soldered tapes and striated coated conductors," *IEEE Trans. Appl. Supercond.*, vol. 26, no. 3, Apr. 2016, Art. no. 4700607.
[1.20] S. Hahn, D. K. Park, J. Bascunan, and Y. Iwasa, "HTS pancake coils without turn-to-turn insulation," *IEEE Trans. Appl. Supercond.*, vol. 21, no. 3, pp. 1592–1595, Jun. 2011.
[1.21] T. Oki *et al.*, "Evaluation on quench protection for no-insulation REBCO pancake coil," *IEEE Trans. Appl. Supercond.*, vol. 26, no. 4, Jun. 2016, Art no. 4702905.
[1.22] T. Lecrevisse, A. Badel, T. Benkel, X. Chaud, P. Fazilleau, and P. Tixador, "Metal-as-insulation variant of no-insulation HTS winding technique: pancake tests under high background magnetic field and high current at 4.2K," *Supercond. Sci. Technol.*, vol. 31, no. 5, May 2018, Art no. 055008.
[1.23] A. Mierau *et al.*, "Testing of series superconducting dipole magnets for the SIS100 synchrotron," *IEEE Trans. Appl. Supercond.*, vol. 29, no. 5, p. 7, Aug 2019, Art no. 4003907.
[1.24] L. Liu *et al.*, "Experimental and numerical study of quench propagation characteristics of different epoxy impregnated REBCO coated conductors," *IEEE Trans. Appl. Supercond.*, vol. 31, no. 4, pp. 1-5, Jun. 2021, Art no. 6600805.
[1.25] P. Ju, T. Ma, J. Zhang, Y. Xu and S. Dai, "Influence of Interface Resistance on Current Distribution and Inhomogeneity Effect on Quench Characteristics in REBCO Coated Conductor," *IEEE Trans. Appl. Supercond.*, vol. 32, no. 1, pp. 1-7, Jan. 2022, Art no. 5600307.
[1.26] F. Gömöry, and J. Šouc, "Stability of DC transport in HTS conductor with local critical current reduction," *Supercond. Sci. Technol.*, vol. 34, Jan. 2021, Art no. 025005.
[1.27] F. Gömöry, and J. Šouc, "Current–voltage curve of the high temperature superconductor with local reduction of critical current," *Supercond. Sci. Technol.*, vol. 34, Nov. 2021, Art no. 12LT01.
[1.28] Y. Yanagisawa *et al*., "The mechanism of thermal runaway due to continuous local disturbances in the YBCO-coated conductor coil winding," *Supercond. Sci. Technol.*, vol. 25, no. 7, Jul. 2012, Art no. 075014.
[1.29] G. Celentano *et al*., "Quench behavior of a conduction cooled

$yBa_2Cu_3O_{7-x}$ tape pancake coil," *IEEE Trans. Appl. Supercond.*, vol. 23, no. 3, Jun. 2013, Art no. 4600704.

[1.30] W. Chan, G. Flanagan, and J. Schwartz, "Spatial and temporal resolution requirements for quench detection in $(RE)Ba_2Cu_3O_x$ magnets using Rayleigh-scattering-based fiber optic distributed sensing," *Supercond. Sci. Technol.*, vol. 26, Aug. 2013, Art. no. 105015.

[1.31] P. Bruzzone *et al.*, "High temperature superconductors for fusion magnets," *Nuci. Fusion*, vol. 58, Aug. 2018, Art no. 103001.

[1.32] G. Flanagan *et al*., "Evaluation and implementation of high performance real-time signal processing for Rayleigh scattering based quench detection for high field superconducting magnets," in *Proc. Iny. Part. Accel. Conf. 2012*, New Orleans, LA, USA, 2012, pp. 3602–3604.

[1.33] F. Scurti, S. Ishmael, G. Flanagan, and J. Schwartz, "Quench detection for high temperature superconductor magnets: a novel technique based on Rayleigh-backscattering interrogated optical fibers," *Supercond. Sci. Technol.*, vol. 29, Jan. 2016, Art. no. 03LT01.

[1.34] S. Hasegawa, S. Ito, G. Nishijima and H. Hashizume, "Quench detection performance of low-temperature superconducting quench detectors for REBCO tape in magnetic fields," *IEEE Trans. Appl. Supercond.*, vol. 31, no. 5, pp. 1-5, Aug. 2021, Art no. 4701605.

Chapter 2 Knowledge Relevant to Quench/Thermal Runaway Detection and Protection

2.1 Quench and Thermal Runaway in Experiments

As introduced in **Chapter 1**, the transition from the superconducting state to the normal conducting state can be caused by factors affecting the magnetic field, current, and temperature. To discuss the factors inducing the irreversible normal transition, the normal transitions are classified into two types: quench and thermal runaway.

"Quench" refers to the normal transition caused by the temperature rise induced by local and transient thermal disturbances. For example, thermal disturbance can be caused by friction (under electromagnetic force), cracking of resin at low temperature, and beam injection in an accelerator system. To simulate the local and transient thermal disturbances, quench is induced by a heat pulse using a resistive heater in the experimental studies of this research.

"Thermal runaway" refers to the normal transition caused by continuous Joule heating when the operating current exceeds the critical current. Such Joule heating can be caused by several reasons: (a) overcurrent: the operating current may increase to a value exceeding the critical current due to some mistakes on controlling the power supply; (b) decrease in critical current: when an unexpected temperature rise occurs (caused by the cooling system or heating by radiation in the case of accelerators or fusion magnets), the critical current decreases, leading to thermal runaway. In the experimental studies conducted in this work, thermal runaway, which initiates at sections where the critical current is relatively low, is induced by increasing the operating current.

2.2 Typical Methods for Detecting Quench/Thermal Runaway

2.2.1 Normal Voltage

Monitoring the normal voltage is an efficient way to detect quench/thermal runaway. Normal resistance appears when the normal transition occurs in a superconducting magnet. However, because of self-inductance, voltage can appear in a superconducting magnet during current ramping ($L \cdot \mathrm{d}I/\mathrm{d}t$). To avoid detecting the voltage induced by self-inductance, "balance voltage" is typically used when applying quench/thermal runaway detection using normal voltage.

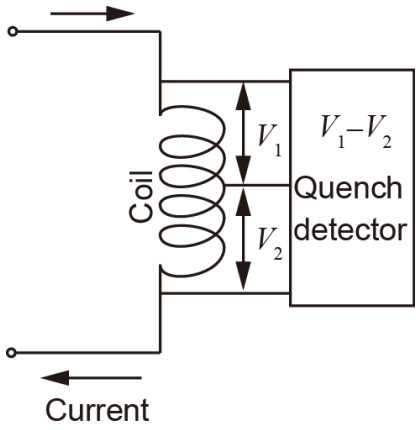

Figure 2.1 Detection using balance voltage.

The detection method using voltage is shown in Figure 2.1. Halves of the voltage (V_1 and V_2) on the coil are monitored and compared. When the balance voltage (V_1-V_2) exceeds a certain threshold (*e.g.*, detection voltage), the protection methods are activated.

2.2.2 Temperature Rise

Another parameter that appears at the initiation of quench/thermal runaway is temperature rise. The popular quench detection method based on temperature uses Rayleigh-backscattering interrogated optical fibers [2.1]. The wavelength of light reflected by the grating (*i.e.*, Bragg wavelength) is proportional to the grating period and its effective refractive index [2.2], which can provide temperature and strain information. The optical fiber is wound with the conductor in the superconducting magnet, as shown in Figure 2.2.

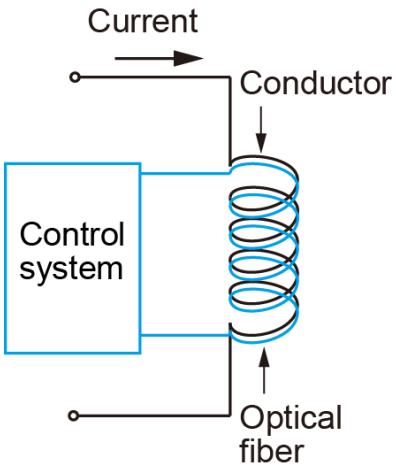

Figure 2.2 Detection by temperature using optical fiber.

Compared with detection based on voltage, the detection method by temperature is supposed to be more sensitive. By assuming that the critical current of the

superconductor linearly relates the temperature (under critical temperature), the current-sharing temperature, T_s, above which current starts to flow in the copper stabilizer of the conductor can be given as follows:

$$T_s = T_{op} + \frac{I_{op}}{I_c}\left(T_c - T_{op}\right), \tag{2.1}$$

where T_{op} and I_{op} are the operating temperature and current, respectively; and T_c and I_c denote the critical temperature and critical current, respectively. In the detection method by voltage, the quench/thermal runaway can be detected above T_s, when current starts to flow in the copper. In contrast, using an optical fiber, the quench/thermal runaway can be detected at an early phase below T_s.

The quench/thermal runaway detection method using the optical fiber is expected to achieve sensitive detection. However, compared with the detection by voltage, the detection by temperature may be more difficult to set up: (a) the optical fiber must be wound with the conductor, and (b) a complex control system is required to analyze the information.

2.3 Typical Methods for Protecting Magnet from Degradation after Quench/Thermal Runaway

2.3.1 External Resistor

The typical circuit using the protection method with a dump resistor is shown in Chapter 1, Figure 1.17 (detection using voltage). When the current starts to flow through the external resistor, the equation is as follows:

$$L\frac{dI}{dt} + I[R_n(t) + R_{ext}] = 0, \tag{2.2}$$

where R_{ext} is the resistance of the external resistor, and $R_n(t)$ is the resistance of the normal zone in the coil (possibly negligible compared with R_{ext}).

2.3.2 Coupled Secondary

In addition to the method of protection by an external resistor, two other methods are available: (a) protection by a coupled secondary; (b) protection by subdivision [2.3].

The typical circuit using the protection method by a coupled secondary is shown in Figure 2.3. The coupled short-circuited secondary winding can consume the energy after quench/thermal runaway and reduce the maximum temperature of the superconducting magnet.

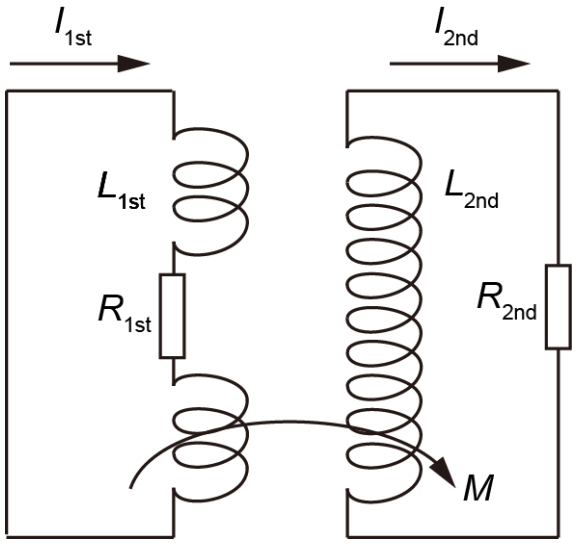

Figure 2.3 Protection by coupled short-circuited secondary.

When quench occurs in the superconducting magnet of the 1st circuit shown in Figure 2.3, the normal resistance, R_n, occurs, and the currents change according to following equations:

$$L_{1st}\frac{dI_{1st}}{dt} + I_{1st}R_n(t) + M\frac{dI_{2nd}}{dt} = 0, \tag{2.3}$$

$$L_{2nd}\frac{dI_{2nd}}{dt} + I_{2nd}R_{2nd} + M\frac{dI_{1st}}{dt} = 0. \tag{2.4}$$

2.3.3 Subdivision

The typical circuit using the protection method by subdivision is shown in Figure 2.4. It is similar to a circuit with an external resistor, as shown in Figure 1.17. However, the superconducting magnet is divided into several sections with their own dump resistors.

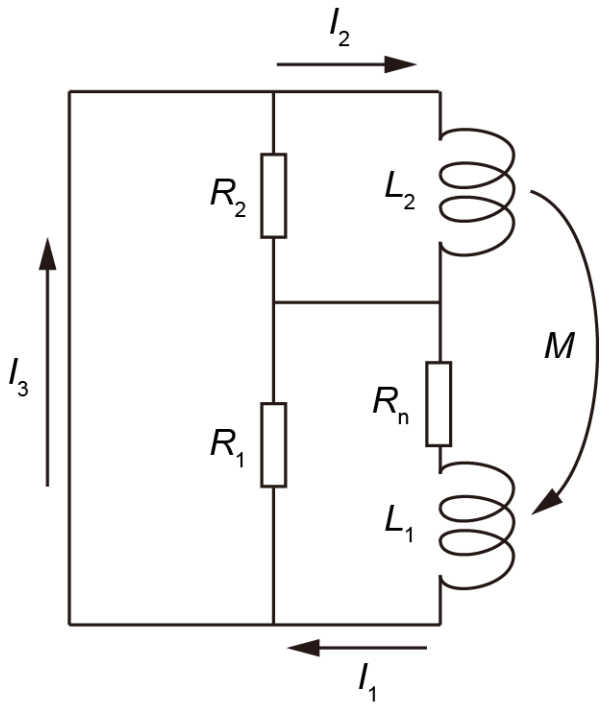

Figure 2.4 Protection by subdivision into two sections.

The circuit equations of the protection method by subdivision shown in Figure 2.4 are as follows:

$$(I_3 - I_1)R_1 + (I_3 - I_2)R_2 = 0, \tag{2.5}$$

$$L_2 \frac{\mathrm{d}I_2}{\mathrm{d}t} + M_{12} \frac{\mathrm{d}I_1}{\mathrm{d}t} + (I_2 - I_3)R_2 = 0, \tag{2.6}$$

$$L_1 \frac{\mathrm{d}I_1}{\mathrm{d}t} + M_{12} \frac{\mathrm{d}I_2}{\mathrm{d}t} + (I_1 - I_3)R_1 + I_1 R_{\mathrm{n}}(t) = 0. \tag{2.7}$$

As shown in equations (2.3) and (2.7), in using the protection method by secondary or subdivision, the speed of current decay in the superconducting magnet depends in some way on the resistance of the normal zone, $R_{\mathrm{n}}(t)$. It may be affected by the duration of thermal disturbance, inducing quench/thermal runaway and rendering the design of the protection circuit difficult.

2.4 Causes of Degradation after Quench/Thermal Runaway

When quench/thermal runaway occurs in a superconducting magnet, irreversible degradation (*e.g.*, irreversible decrease of critical current, disappearance of superconductivity, and burn out) may occur owing to the high temperature induced by Joule heating. Some of the typical reasons for the degradation in superconducting magnets wound with coated conductors are listed in Table 2.1.

TABLE 2.1 TYPICAL REASONS FOR DEGRADATION AFTER QUENCH/THERMAL RUNAWAY

Reasons	Relation to the temperature rise	Voltage–current characteristic
Burn out	Directly	(Current cannot flow)
Solder melting	Directly	・Decrease of I_c ・Disappearence of cuperconductivity
Oxygen desorption from REBCO	Directly	・Decrease of Ic ・Disappearence of cuperconductivity
Delamination of the layer (caused by temperature induced stress)	Indirectly	・Decrease of Ic ・Disappearence of cuperconductivity
Buckling of the conductor (caused by temperature induced stress)	Indirectly	・Decrease of Ic ・Disappearence of cuperconductivity

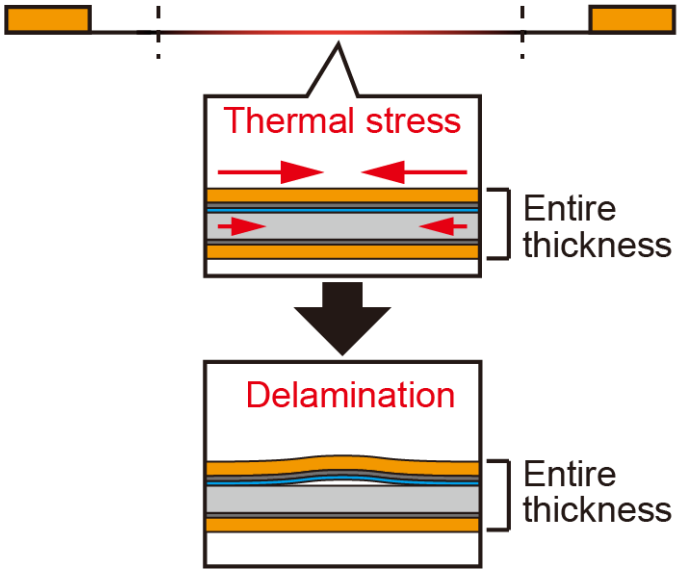

Figure 2.5 Delamination after quench/thermal runaway.

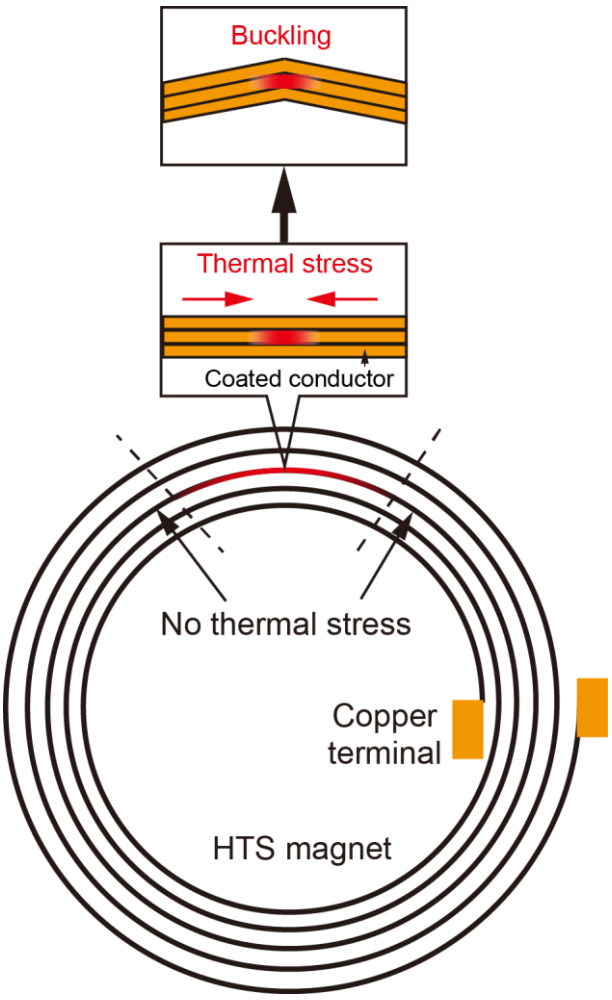

Figure 2.6 Buckling in pancake coil.

After quench/thermal runaway, the rise in temperature can directly cause burnout, solder melting, and oxygen desorption from REBCO. Moreover, temperature rise can indirectly induce stress, which may result in degradation. Because of the multilayer structure of coated conductors, the layers suffer different heat stresses after quench/thermal runaway, resulting in delamination, as shown in Figure 2.5. In a superconducting coil, after quench/thermal runaway, the heat stress appears among the coated conductor layers, as shown in Figure 2.6. It may cause buckling because heat is distributed among the layers.

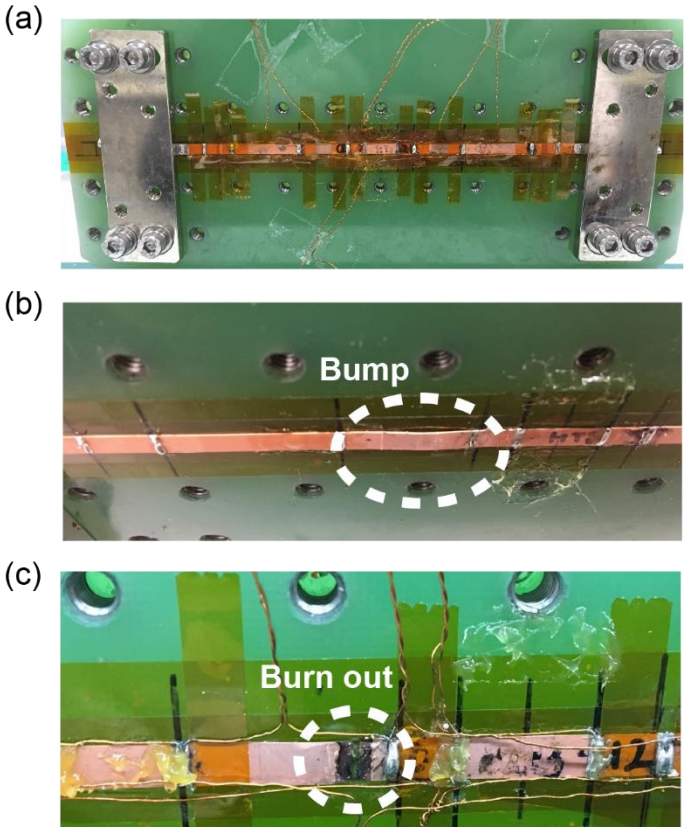

Figure 2.7 Photographs of degraded samples after quench: (a) no visible damage on conductor; (b) sample with bump; (c) sample with burn-out.

Examples of degraded samples are shown in Figure 2.7. In Figure 2.7(a), no visible damage on the conductor is observed; however, the measured critical current decreased. The high temperature after the quench is considered as the possible cause of delamination among the layers of the coated conductor. In Figure 2.7(b), the linear voltage–current characteristics (normal conducting) are measured after the quench; a section with a bump, possibly induced by thermal stress, is observed on the conductor. When the temperature is extremely high after the quench, part of the conductor may melt, as shown in Figure 2.7(c). Although the degradation modes (*e.g.*, bumping and burning out) after quench/thermal runaway differ, the degradation is directly or indirectly induced by the temperature rise. The discussion in the following sections focuses on the maximum temperature after quench/thermal runaway to elaborate on the conditions for protection.

2.5 Useful Equations for the Analysis of Quench/Thermal Runaway

2.5.1 Equations for Calculating Temperature Rise After Quench/Thermal Runaway

In the case of a conduction-cooled coated conductor in adiabatic conduction (no transverse thermal diffusion), the conductor temperature when quench occurs can be calculated using the following 1D heat conduction equation [2.3]:

$$\gamma C_{\mathrm{c}} \frac{\partial T}{\partial t} = \frac{\partial}{\partial x}\left(k_{\mathrm{c}} \frac{\partial T}{\partial x}\right) + \frac{p_{\mathrm{ds}}}{L_{\mathrm{ds}} w t_{\mathrm{c}}} + g, \tag{2.8}$$

where T is temperature; x is the coordinate along the conductor; γC_{c} is the volumetric specific heat of the conductor (γ is density); k_{c} is the thermal conductivity of the conductor; p_{ds} and L_{ds} are the power and length of thermal disturbance (which initiates quench), respectively; w is the width of the conductor; t_{c} is the thickness of the conductor; and g refers to the generation of Joule heating.

By ignoring thermal conduction for a brief period, the foregoing equation can be as (2.9):

$$\gamma C_{\mathrm{c}} \frac{\partial T}{\partial t} = \frac{\partial}{\partial x}\left(k_{\mathrm{c}} \frac{\partial T}{\partial x}\right) + \frac{p_{\mathrm{ds}}}{L_{\mathrm{ds}} w t_{\mathrm{c}}}. \tag{2.9}$$

Because the thermal disturbance that induces quench is usually transient, equation (2.9) may be similar to equation (2.10). This may be observed after the end of the thermal disturbance in which the temperature rise is induced by Joule heating and thermal conduction is negligible:

$$g = \frac{I(t)^2 R(t)}{V} = \gamma C(T(t)) \frac{\mathrm{d}T}{\mathrm{d}t}. \tag{2.10}$$

Because resistance $R(t)$ is related to temperature, when the temperature at time t is equal to T, $R(t)$ must be equivalent to $R(T)$, and equation (2.10) can be transformed into equation (2.11):

$$\frac{I(t)^2}{V} \mathrm{d}t = \frac{\gamma C(T)}{R(T)} \mathrm{d}T. \tag{2.11}$$

Based on equation (2.11), the temperature at a certain time can be calculated through integration [2.4]:

$$\int_{t_0}^{t} \frac{I(t\prime)^2}{V} \mathrm{d}t' = \int_{T_0}^{T} \frac{\gamma C(T\prime)}{R(T\prime)} \mathrm{d}T\prime, \tag{2.12}$$

where t_0 is the time when the temperature of the conductor is T_0; V is the volume of the conductor; $I(t)$ is the operating current; and $C(T)$ and $R(T)$ are the heat capacity and resistance of the conductor, respectively.

In this study, a 1D quench simulation was performed based on equation (2.8). The experimental results were compared with the simulation results and those calculated by ignoring the thermal conduction in equation (2.12).

2.5.2 Equations for Calculating Normal Zone Propagation

When the normal zone (*i.e.*, the zone in a normal state) appears in a superconducting magnet, Joule heating occurs near the normal zone. If the Joule heating power exceeds the cooling power (convective and/or conductive), then the superconductors near the normal zone transition from the superconducting state to the normal state as the temperature rises. The normal zone propagation velocity (NZPV) is a parameter for evaluating the speed of the spread of the normal zone. The fast spread of the normal zone enables the easy detection of quench because the normal voltage rapidly increases and is easy to detect. Depending on the operating current/critical current density, the NZPV in LTSs (e.g., Nb–Ti) can be several tens of meters per second, which is a hundred times faster than that in REBCO coated conductors.

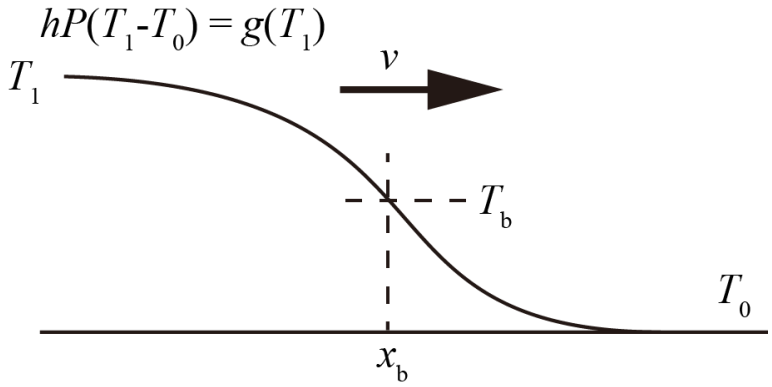

Figure 2.8 Temperature profile at boundary of normal zone advancing from left to right (x_b: boundary of normal zone; T_1: temperature at which cooling power equals Joule heating power; T_b: temperature at boundary of normal zone; T_0: initial temperature; h: heat transfer coefficient; P: wetted perimeter; and g: Joule heat generation).

Assume that the boundary, x_b, of the normal zone moves at a constant velocity, v, and this point is considered as the origin of a new coordinate, $\epsilon = x - x_b = x - vT$. Consequently, $\partial T/\partial t = -v\,\partial T/\partial \epsilon$, and the 1D thermal conduction equation, (2.8), becomes (2.11) at the end of the thermal disturbance ($p_{ds} = 0$) [2.3]:

$$\frac{d^2T}{d\epsilon^2} + \frac{v\gamma C}{k}\frac{dT}{d\epsilon} - \frac{hP}{kA}(T - T_0) + \frac{g}{k} = 0, \tag{2.13}$$

where A is the cross-sectional area of the conductor.

With the boundary conditions $T = T_b$ at $x = x_b$, $T = T_1$ as $x \to -\infty$, and $T = T_0$ as $x \to \infty$ (Figure 2.8), the solutions for T_r and T_l (the temperature values on the left and right sides of the boundary of normal zone, respectively) are [2.3]

$$T_l = T_1 - (T_1 - T_b)e^{\alpha_1 \epsilon}, \tag{2.14}$$

$$T_r = T_0 + (T_b - T_0)e^{\alpha_2 \epsilon}, \tag{2.15}$$

where

$$\alpha_1 = \frac{1}{2}[(v\gamma C/k)^2 + 4hP/kA]^{\frac{1}{2}} - v\gamma C/2k, \tag{2.16}$$

$$\alpha_2 = -\frac{1}{2}[(v\gamma C/k)^2 + 4hP/kA]^{\frac{1}{2}} - v\gamma C/2k, \tag{2.17}$$

$$T_1 = T_0 + g(-\infty)/hP. \tag{2.18}$$

The heat flow at the interface between the left and right of x_g must be continuous:

$$-k\frac{dT_l}{d\epsilon}\bigg|_{\epsilon=0} = -k\frac{dT_r}{d\epsilon}\bigg|_{\epsilon=0} + vQ_L, \tag{2.19}$$

where Q_L is the latent heat of transition between the superconducting and normal states of Type I superconductors.

By combining equations (2.14)–(2.19), the propagation velocity can be derived as follows:

$$v = \left(\frac{khP}{A}\right)^{\frac{1}{2}} \frac{[T_1 - T_0 - 2(T_b - T_0)]}{[Q_L^2 + Q_L\gamma C(T_1 - T_0) + \gamma^2 C^2 (T_b - T_0)(T_1 - T_b)]^{\frac{1}{2}}}. \tag{2.20}$$

By assuming that $hP(T_1 - T_0) = g(T_1) = J^2\rho A$, where J is the overall current density, and ρ is resistivity, equation (2.20) may be written in the following form. The first two terms in equation (2.21) denote the adiabatic propagation velocity for the conductors that are not cooled [2.1]:

$$v = \frac{J}{\gamma C}\left(\frac{\rho k}{T_b - T_0}\right)^{\frac{1}{2}} \frac{(1 - 2y)}{[yz^2 + z + 1 - y]^{\frac{1}{2}}}. \tag{2.21}$$

Based on the Wiedemann–Franz–Lorentz law, ρk may be found at some

appropriate mean temperature. If $\rho k = L_0 T_s$ and $T_s = (T_b + T_c)/2$ are assumed, and the transverse thermal diffusion (adiabatic propagation velocity) is ignored, then the NZPV could be calculated using the following equation:

$$v = \frac{J}{\gamma C}\left\{\frac{L_0(T_g+T_c)}{T_g+T_c-2T_0}\right\}^{\frac{1}{2}}, \tag{2.22}$$

where J represents the overall current density; L_0 is the Lorentz number (2.45×10^{-8} W·Ω·K^{-2}) from the Wiedemann–Franz–Lorentz law; T_g is the temperature at which heat is generated; T_c is the critical temperature; and T_0 is the initial temperature (operating temperature).

By assuming that J_c and T have a linear relationship, parameter T_g can be expressed as follows:

$$T_g = T_c - (T_c - T_0)\frac{J}{J_{c0}}, \tag{2.23}$$

where J_{c0} is the overall critical current density at the initial temperature. The volumetric specific heat, γC, is calculated by considering the mean over the temperature range of transition, as follows:

$$\gamma C = \left\{\frac{T_c^4 - T_0^4}{4T_0^3(T_c - T_0)}\right\}\sum_n \lambda_n \gamma_n C_{0n}, \tag{2.24}$$

where λ_n is the proportion of the nth component; γ_n is its density; C_{0n} is its specific heat at T_0; and C is assumed to vary with T^3.

[References]

[2.1] G. Flanagan *et al*., "Evaluation and implementation of high performance real-time signal processing for Rayleigh scattering based quench detection for high field superconducting magnets," in *Proc. Iny. Part. Accel. Conf. 2012*, New Orleans, LA, USA, 2012, pp. 3602–3604.

[2.2] F. Scurti, S. Ishmael, G. Flanagan, and J. Schwartz, "Quench detection for high temperature superconductor magnets: a novel technique based on Rayleigh-backscattering interrogated optical fibers," *Supercond. Sci. Technol.*, vol. 29, Jan. 2016, Art. no. 03LT01.

[2.3] M. N. Wilson, Superconducting Magnets, Oxford, U.K.:Clarendon, 1983.

[2.4] T. Ogitsu, "Superconducting magnets technologies for large accelerator," *J. Particle Accelerator Society of Japan*, vol. 14, no. 2, pp. 66–73, 2017.

Chapter 3 Common Experimental Methods in This Study

3.1 Setup of Short-Sample Experiments

This study only considers the longitudinal propagation of quench (*i.e.*, transverse quench propagation is neglected). Rather than burning expensive REBCO coils, the experiments were conducted using short samples of REBCO coated conductors (short-sample experiments). Owing to their slow NZPV, the use of a short coated conductor sample was considered possible to simulate the initiation phase of REBCO coils. Fast-turnaround experiments using short samples enabled the derivation of well-organized data on hot-spot temperature under various conditions in addition to the conditions for successful/failed quench detection and protection.

The typical experimental setup and schematic of the short sample are shown in Figures 3.1 and 3.2, respectively. The sample is fixed at the bottom of a vacuum cryostat and cooled using a GM cryocooler by conductive cooling. In the experiments using a single straight coated conductor, the sample is fixed using epoxy resin (EP-270 produced by Kyowa Electronic Instruments Company) on a polyimide tape adhered to a glass fiber-reinforced plastic (GFRP) block. Another side of the sample faces a vacuum; Cernox temperature sensors (shown as CX in the figures), a resistive quench heater (shown as HT1), and thermocouples (shown as TC in the figures) are attached to this side. Each end of the sample is soldered to a copper terminal on which another copper block is fixed with screws. The copper block is connected to a current busbar by a braided copper wire, as shown in Figure 3.2. Because the thermal conductivity of the GFRP is low, the sample is primarily cooled via the copper terminals connected to the current busbars, which are cooled by the cryocooler. The cryostat in which the sample is installed is inserted into a room-temperature bore of a conduction-cooled superconducting magnet that can apply a magnetic field (from $\mu_0 H$ up to 2 T) normal to the sample tape.

Some structures in this cryostat aid in cooling the sample to a low temperature level. To decrease the conduction heat, HTSs are used as part of the current leads between the 1st and 2nd stages of cryocooler, as shown in Figure 3.3. These reduce the heat transfer through the copper current leads from the room-temperature side to the low-temperature side in the cryostat. As shown in Figure 3.4, an inner shield made by copper, which is cooled by the cryocooler, is provided. The low-temperature inner shield with multilayer insulation decreases the radiant heat. This dry cryostat (cooled only using cryocooler) enables the conduct of experiments from 10 to 75 K using a temperature control heater near the sample holder.

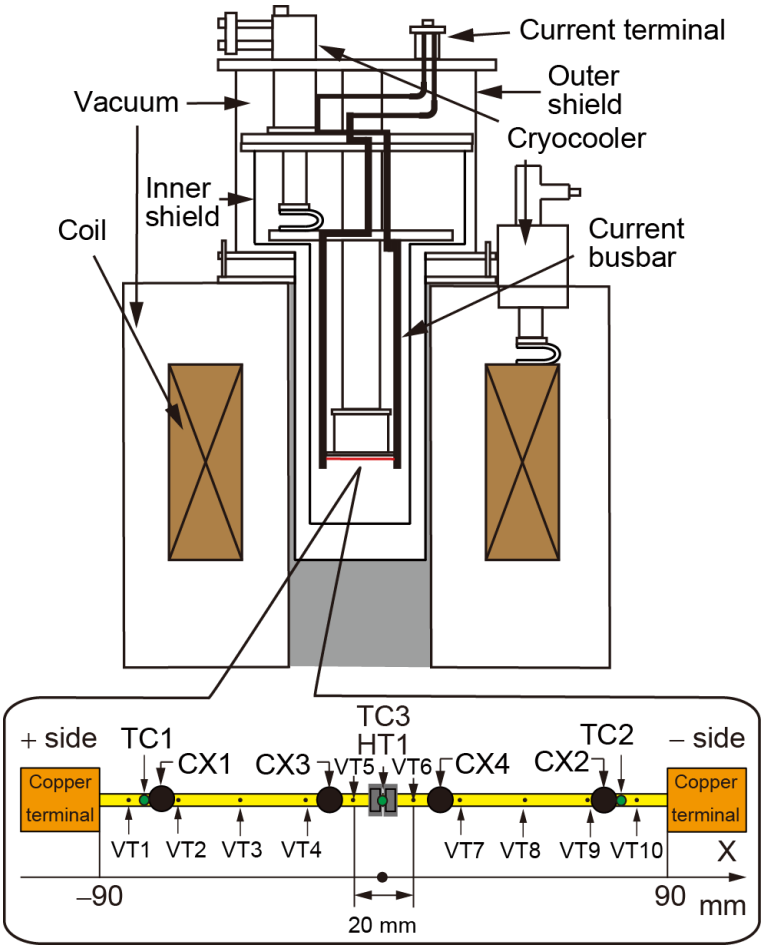

Figure 3.1 Typical experimental setup using single REBCO coated conductor (VT: voltage tap; TC: thermocouple; CX: Cernox temperature sensor; HT1: resistive quench heater) [3.1] © 2019 IEEE.

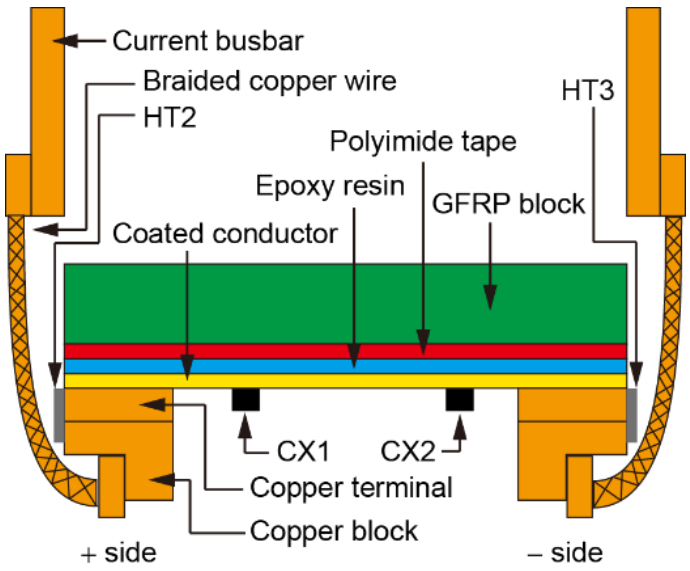

Figure 3.2 Schematic of short sample [3.1] © 2019 IEEE.

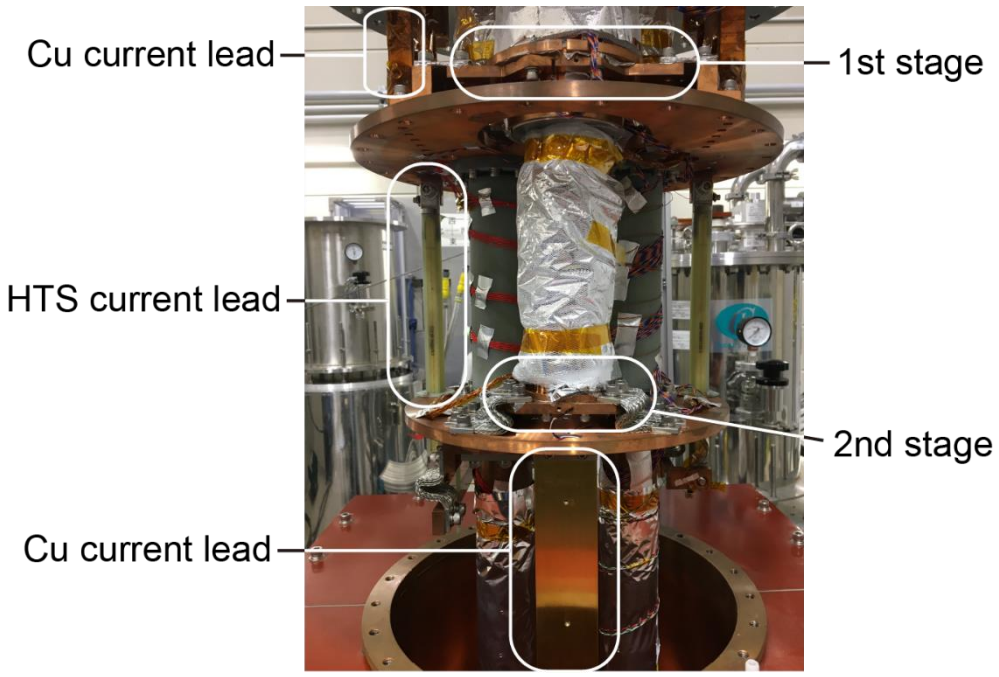

Figure 3.3 Photograph of conduction-cooled cryostat near the 1st and 2nd stages of cryocooler (current leads are insulated from cryostat using thin sapphire plates).

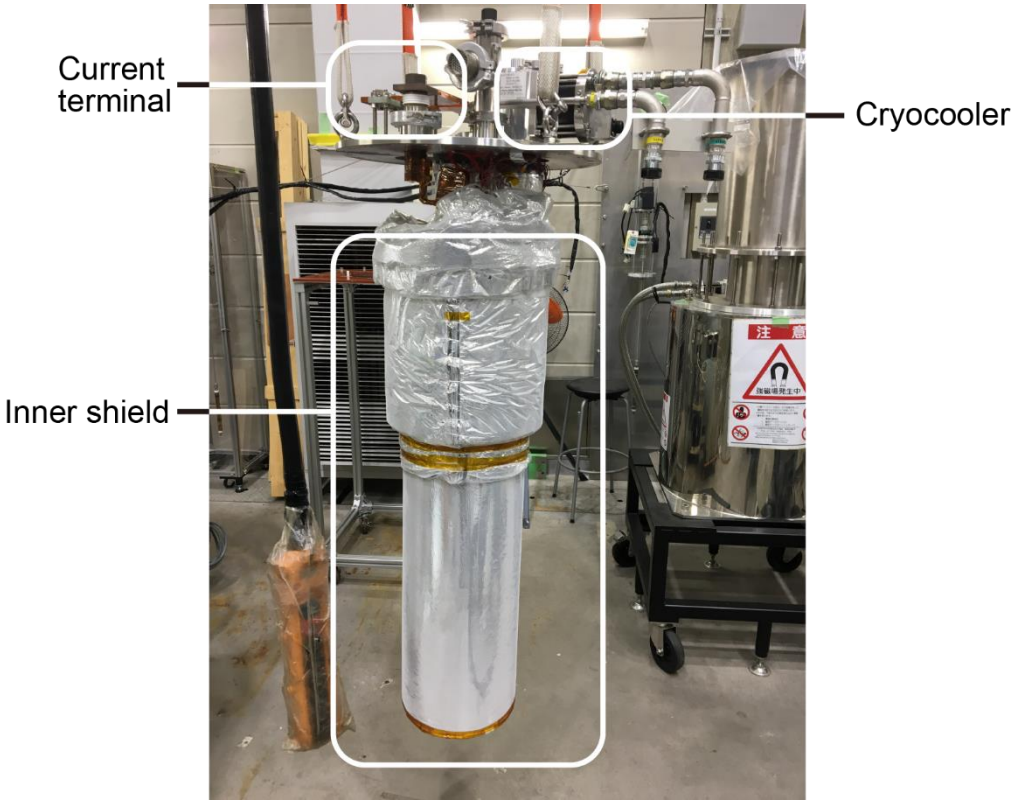

Figure 3.4 Photograph of inner shield (with multi-layer insulation) of conduction-cooled cryostat.

3.2 Quench/Thermal Runaway Detection and Protection Circuit

In **Chapter 2**, Figure 2.2 shows the quench detection method using balance voltage. Because the normal zone rarely appears at the exact center of a magnet when quench occurs, the detection and protection circuit can be simplified into Figure 3.5(a). In the short-sample experiments, the quench detection and protection processes are simulated using an FPGA module that controls the sample current and monitors the voltage of an entire sample and the high-speed power supply, as shown in Figure 3.5(b). Once the monitored voltage of the entire sample reaches a detection voltage (simulating quench detection) after a delay time (simulating the time required for detection in a real coil and time required to activate the circuit breaker), the sample current decreases exponentially (simulating current decay by the dump resistor while neglecting normal resistance).

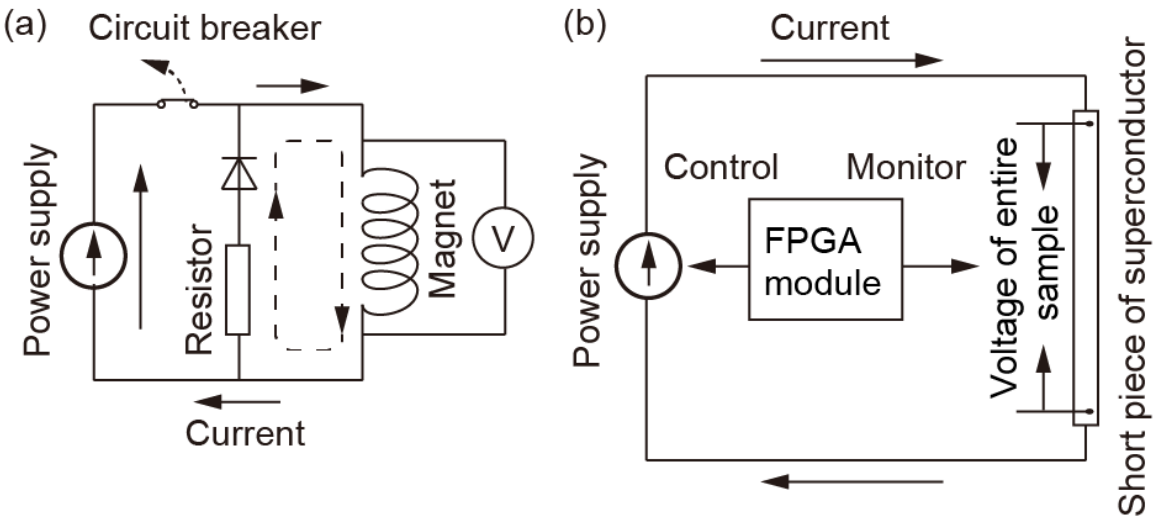

Figure 3.5 Quench detection and protection circuits: (a) Conventional quench detection and protection circuits of magnets using external dump resistor; (b) Circuit for short-sample experiments using FPGA module to simulate quench detection and protection of magnets [3.1] © 2019 IEEE.

3.3 Hot-spot Temperature Measurement

Because the temperature during the quench detection and protection processes directly depends on whether a superconducting magnet degrades after the quench, estimating the hot-spot temperature, which is the highest temperature in the superconducting magnet, is important. In the experimental study, the hot-spot temperature due to the voltage near the location where quench was initiated was determined. As shown in Figure 3.6, assuming that current sharing between the superconductor and copper occurs, the relationship between normal voltage and

temperature can be determined from the critical current (I_c), temperature (T) characteristic of the sample, and temperature dependence of the resistivity of the plated copper. In the calculation, the current-sharing model is used. In this model, the current flowing through the copper is as follows ($T < T_c$):

$$I_{Cu}(T) = I_{op} - I_c(T). \tag{3.4}$$

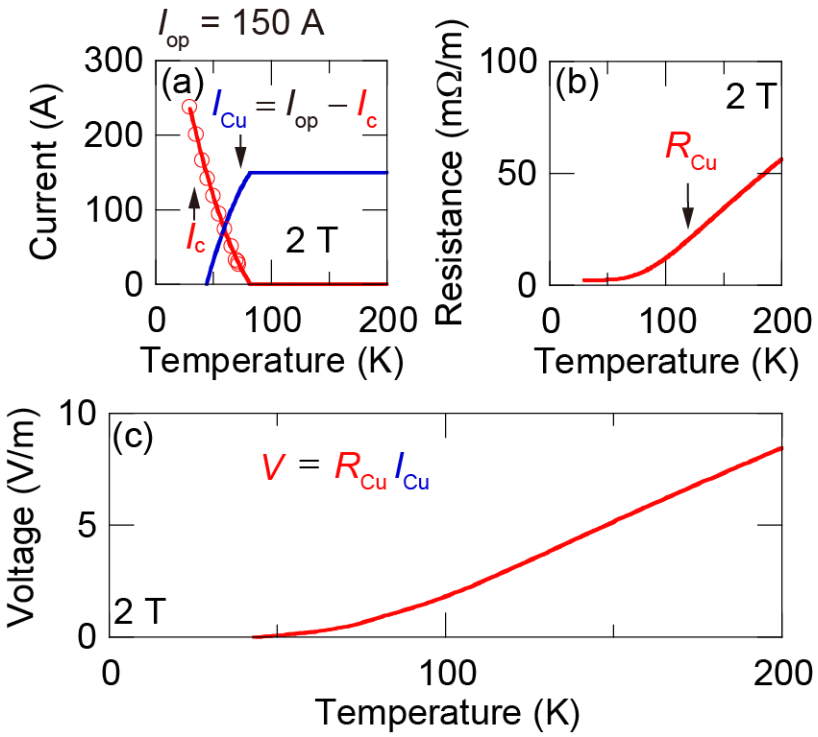

Figure 3.6 Voltage–temperature relationship calculated by current-sharing model: (a) Critical current (I_c) and current flow in copper stabilizer (I_{Cu}) vs temperature, where $I_{Cu} = I_{op}–I_c$ (I_{op} = 150 A); (b) copper stabilizer resistance (R_{Cu}) vs temperature (RRR = 50, S_{Cu} = 0.26 mm^2); (c) Voltage (V) vs temperature, where $V = R_{Cu}I_{Cu}$ [3.1] © 2019 IEEE.

[References]

[3.1] X. Luo, S. Inoue, and N. Amemiya, “Experimental study on quench detection and protection conditions of copper-stabilized coated conductors using short samples,” *IEEE Trans. Appl. Supercond.*, vol. 29, no. 8, Dec. 2019, Art. no. 4703511.

Chapter 4 Protection Conditions Against Quench Induced by Local and Transient Thermal Disturbances

4.1 Chapter Background and Objective

It has been reported that the quench protection of magnets fabricated using a $REBa_2Cu_3O_y$ (RE-123) coated conductor is more difficult than that of LTS magnets [4.1] because the NZPV of RE-123 coils is significantly slower [4.2], [4.3]. A practical solution to this problem is non-insulation winding (the conductors are conductive among the turns of a coil) [4.4]–[4.6]; however, this solution is not always applicable to certain types of magnets. Such magnets include those that must be ramped up relatively rapidly (*e.g.*, magnets for synchrotron [4.7] and MRI magnets) that are equipped with gradient coils, which generate time-dependent magnetic fields. Another possible solution is sensitive quench detection, which enables the magnet current to be shut down before the formation of a crucial hot spot. For example, a novel quench detection method using Rayleigh-backscattering interrogated optical fibers [4.8], [4.9] and another novel method measuring non-uniform currents caused by normal transitions [4.10] have been proposed. However, if the conventional quench detection and protection scheme (*i.e.*, quench detection quench using voltage taps (VTs) and dumping the stored energy in an external dump resistor) is applicable, then it is a useful and attractive option because of its simplicity and well-established hardware.

Many experimental studies have been performed to investigate the quench characteristics of REBCO coated conductors that include NZPV and hot-spot temperature [4.11]–[4.14]. However, these previous experimental studies have primarily focused on quench behaviors and have not directly discussed the conditions under which the conventional quench detection and protection scheme can be applied. Such conditions have been studied theoretically [4.15]–[4.18]; however, they have not been well clarified experimentally for conduction-cooled REBCO coils. Herein, the conditions of the conventional quench detection and protection scheme are primarily represented by the time constant for the energy dump (*i.e.*, the time constant of the current decay and voltage threshold for quench detection (detection voltage)).

In addition to the conditions of the quench detection and protection scheme, the amount of copper stabilizer in the cross-section of a superconductor must be a significant parameter in the context of quench protection because it directly impacts Joule heating in the quench process [4.19]. In the early stage of the development of

RE-123 coated conductors, their superconductor layers were covered only with several-micrometer-thick silver layers [4.20]. Recently, attaching copper stabilizers has become common in commercially available coated conductors; however, their cross-sections are still relatively small [4.21]–[4.22]. For example, in the case of a 4-mm-wide coated conductor plated with 20-μm-thick copper carrying 200 A of current, the current density in the event of quench is 1250 A/mm^2.

The objectives of this chapter are as follows:

1) to demonstrate the applicability of the conventional quench detection and protection scheme to conduction-cooled REBCO coils. The conditions for successful quench detection and protection (such as those related to detection voltage, time constant current decrease, and operating current) are experimentally determined;
2) to understand the impact of using copper stabilizer on quench protection. Quench detection and protection experiments are performed at various operating currents using the conventional quench detection and protection scheme (*i.e.*, detecting quench using voltage and dumping the stored energy in an external dump resistor).

4.2 Sample Information

To study the conditions for successful quench detection and protection (detection voltage, time constant for current decrease, operating current, etc.), a standard coated conductor fabricated by SuperPower Inc. (SCS4050) is used; its specifications are listed in Table 4.1. Furthermore, the critical current of the sample measured at various temperatures under a magnetic field of 2 T is shown in Figure 4.1.

To study the impact of copper stabilizer on quench protection, several samples with different copper thicknesses are used. These include coated conductors fabricated by Fujikura and SuperPower Inc.; specifications are listed in Table 4.1. The thicknesses of Hastelloy substrates in FYSC-SCH04 and FYSC-SCH04(40) are the same; however, the copper stabilizer in FYSC-SCH04(40) is thicker. Moreover, the plated copper thicknesses of FYSC-SCH04 and SCS4050 are the same; however, the Hastelloy substrate in FYSC-CSH04 is thicker. The measured critical current values of samples at various temperatures are depicted in Figure 4.2.

The entire length of the sample, including the length attached to the copper current terminals (25 mm each), is 230 mm. The arrangement of VTs and temperature sensors is shown in Figures 4.3 and 4.4. Positions of VT, resistive quench heater (HT1), Cernox temperature sensors (CX), and thermocouples (TC)

on the short sample are shown in Figure 4.4. The voltage between VT1 and VT10 ($v_{1–10}$) was considered as the voltage of the entire sample, and the voltage between VT5 and VT6 ($v_{5–6}$) was used to calculate the hot-spot temperature. The temperature of the sample (T_i) is PID (proportional–integral–derivative)-controlled at 30 K using the temperature of samples measured by two Cernox sensors (CX1 and CX2) and resistive heaters for temperature control (HT2 and HT3) attached to the copper terminals and copper blocks, as shown in Figure 3.2. The temperature of 30 K was selected to reduce the critical current (*i.e.*, to increase the load ratio (operating current/critical current) to a practical level) under the maximum magnetic field that can be generated by the magnet (2 T).

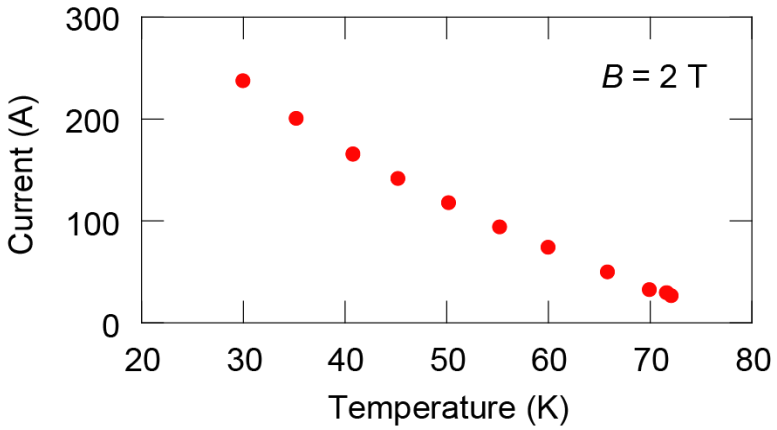

Figure 4.1 Critical current of SCS4050 measured at various temperatures (B = 2 T perpendicular to tape; E_0 = 100 μV/m) [4.23] © 2019 IEEE.

TABLE 4.1
SPECIFICATIONS OF SAMPLE

Properties	FYSC-SCH04 (Fujikura)	FYSC-SCH04(40) (Fujikura)	SCS4050 (SuperPower)
Width	4 mm	4 mm	4 mm
Entire thickness	0.13 mm	0.17 mm	0.1 mm
Plated-copper thickness (Total copper thickness)	20 μm (40 μm)	40 μm (80 μm)	20 μm (40 μm)
Thickness of Hastelloy substrate	75 μm	75 μm	50 μm
Critical current (77 K, self field)	~ 249 A	~ 241 A	~ 99 A

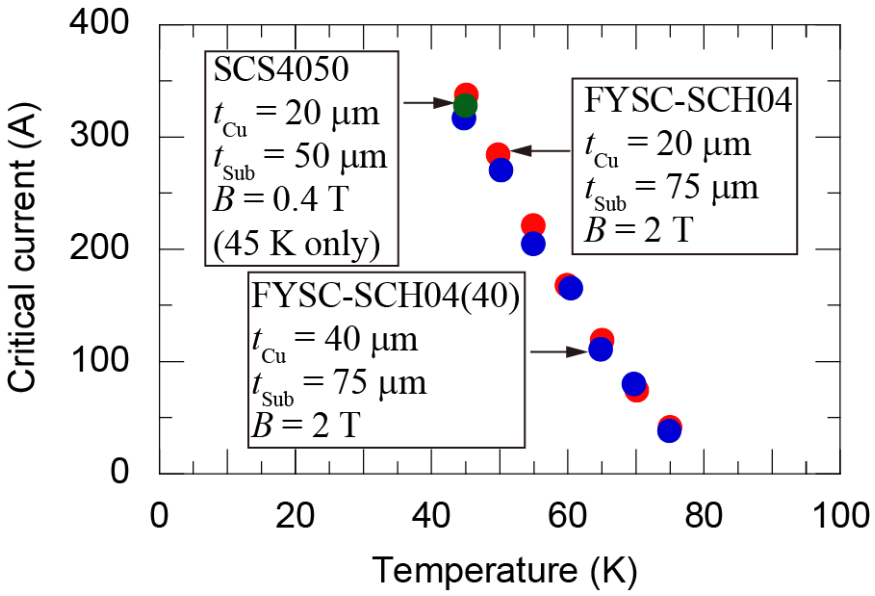

Figure 4.2 Critical current of samples measured at various temperatures (magnetic field is perpendicular to tape; E_0 = 100 μV/m) [4.24] © 2020 IEEE.

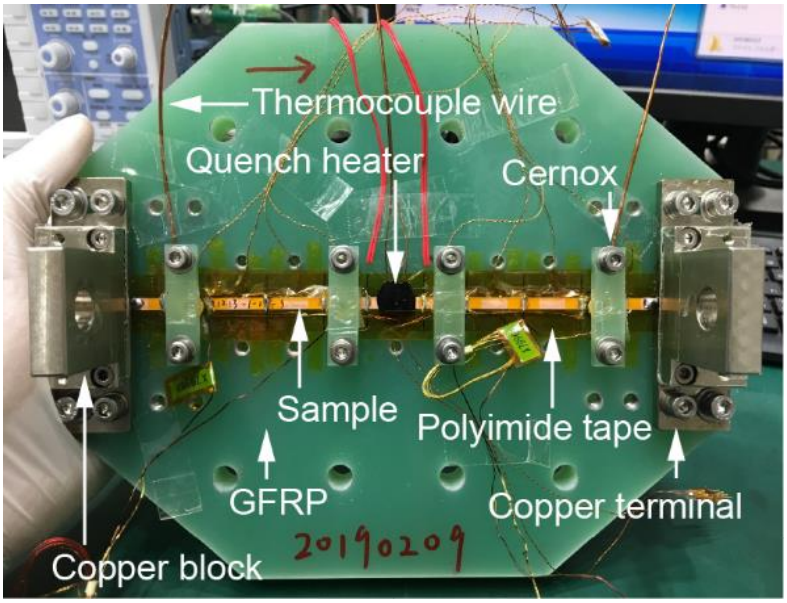

Figure 4.3 Photograph of short sample on GFRP block [4.23] © 2019 IEEE.

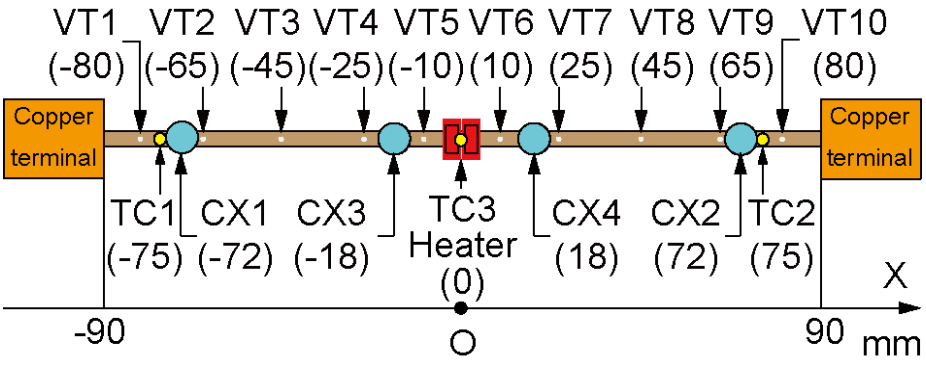

Figure 4.4 Positions of VTs and temperature sensors (VT: voltage tap; TC: thermocouple; CX: Cernox temperature sensor). Numbers in brackets indicate relative positions (in mm) to sample center in longitudinal direction [4.23] © 2019 IEEE.

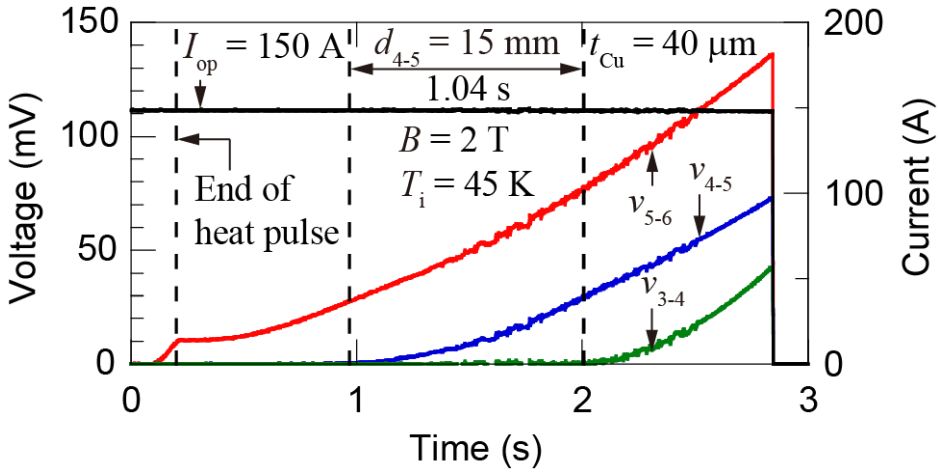

Figure 4.5 Example of NZPV measurement (T_i = 45 K, B = 2 T, I_{op} = 150 A, FYSC-SCH04(40); v_{m-n}: voltage between VTm and VTn; d_{m-n}: distance between VTm and VTn) [4.24] © 2020 IEEE.

The NZPVs of samples manufactured by Fujikura were measured and compared before the quench detection and protection experiments. Figure 4.5 depicts the voltage and current waveforms in an example of NZPV measurement. The time when v_{4-5} (voltage between VT4 and VT5) and v_{3-4} (voltage between VT3 and VT4) reach 1 mV as well as d_{4-5} (distance between VT4 and VT5: 15 mm) is used to estimate the NZPV. In the case shown in Figure 4.5, the NZPV of FYSC-SCH04(40) when T_i = 45 K, B = 2 T, and I_{op} = 150 A is 15 mm/1.04 s = 14.4 mm/s.

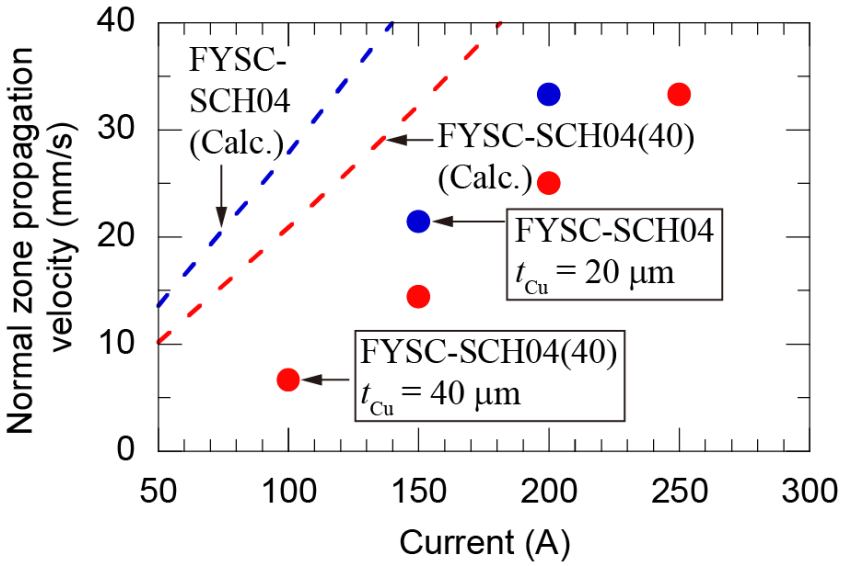

Figure 4.6 NZPV vs current in coated conductors with different copper thicknesses (T_i = 45 K; B = 2 T; I_c = ~320 A) [4.24] © 2020 IEEE.

Using the calculation method introduced in **Chapter 2**, the NZPVs of FYSC-SCH04 and FYSC-SCH04(40) can be computed. The calculated NZPVs are represented as dashed lines in Figure 4.6. The measured NZPVs were lower than the calculated results; this might be attributed to the transverse thermal diffusion in the experiments. Moreover, certain assumptions on the physical properties (C varies as T^3, ignoring the effect of magnetic field) might have some influence on such differences between the calculated and measured results. Both the calculated and experimental results indicate that increasing the thickness of plated copper in a coated conductor causes a decrease in the propagation velocity. In a previous study, it was reported that increasing the heat capacity is the main reason for the decrease in the NZPV when the copper thickness is increased [4.25]. However, based on equation (2.4), because these two samples have virtually the same T_g, T_c, and T_0 values, and the difference in the heat capacity, γC, between these two coated conductors is not considerable, the decrease in the overall current density, J (achieved by increasing the thickness of the copper stabilizer), is the main reason for this decrease in NZPV.

4.3 Typical Data of Quench Detection and Protection

Figure 4.7(a) shows the typical current and voltage waveforms using SCS4050 in the experiments in which the heat pulse starts at t = 0 at an initial current (hereafter referred to as operating current), I_{op} = 150 A. When the total voltage of the sample reaches the detection voltage (100 mV in this case) after a delay of 0.1 s, the sample

current decreases exponentially (time constant of current decrease = 1 s). In this process, virtually no voltage appears at VT2–VT3 and VT3–VT4, which are located far from the heater. In all the experiments reported herein, the delay was set at 0.1 s, and the heat pulse duration was 200 ms, whereas the detection voltage and time constant of the current decrease were varied. Figure 4.7(b) shows the electric field I–current (I) curves before and after the quench shown in Figure 4.7(a). As shown in Figure 4.7(b), the critical current and n values before and after each quench are measured to determine whether the sample has degraded.

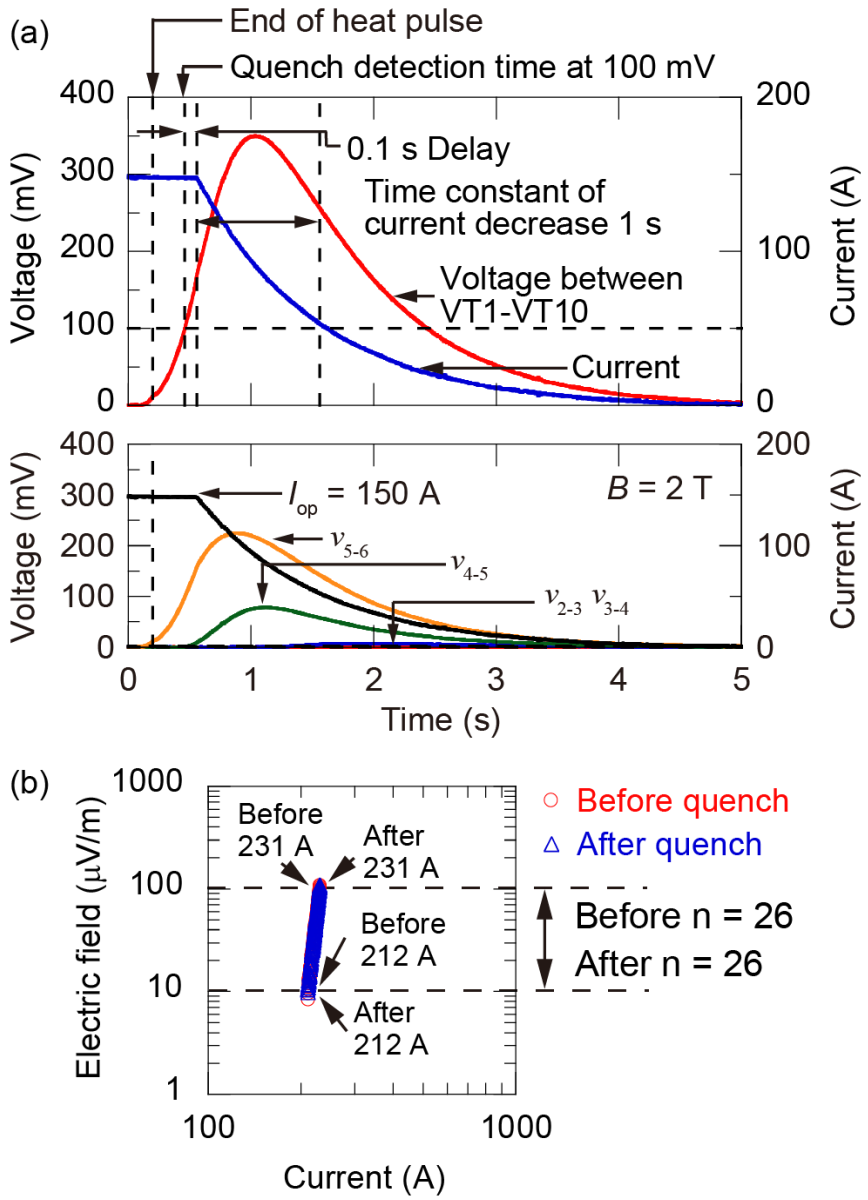

Figure 4.7 Typical data of quench shot using SCS4050: (a) voltage and current waveforms during quench detection and protection processes ($v_{m–n}$: voltage between VTm and VTn); (b) electric field (E)–current (I) curves before and after quench [4.23] © 2019 IEEE.

4.4 Hot-Spot Temperatures under Various Conditions

4.4.1 Operating Current

Figure 4.8 shows the hot-spot temperature and current waveforms of the sample when the operating current is varied. The quench was detected when the total voltage exceeded 100 mV (v_{th} = 100 mV) after a delay of 0.1 s (t_d = 100 ms); the operating current decreased exponentially with a time constant of 1 s (*i.e.*, τ = 1 s). When the operating current was less than 160 A, degradation was not observed after the quench detection and protection processes. The current below which the conductor can be protected is called the *protectable current*.

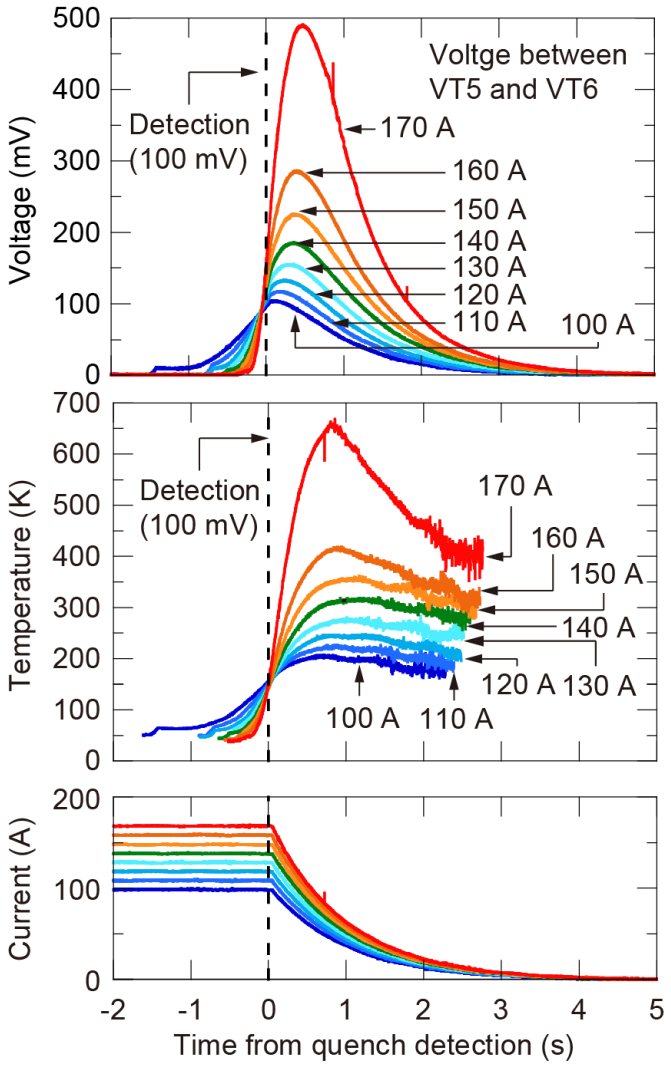

Figure 4.8 Hot-spot temperature derived from $v_{5–6}$ and current waveforms at various operating currents using SCS4050 (B = 2 T, T_i = 30 K, v_{th} = 100 mV, t_d = 100 ms, and τ = 1 s; quench shots implemented using the same short sample).

4.4.2 Time Constant of Current Decrease after Quench

Figure 4.9 shows the hot-spot temperature and current waveforms of the sample when the time constant of the current decrease is varied (the operating current is 100 A). The experiments were performed using a short sample whose critical current was approximately 240 A at 2 T. The heater power (p_{ds}) values in all the experiments shown in Figure 4.9 are identical.

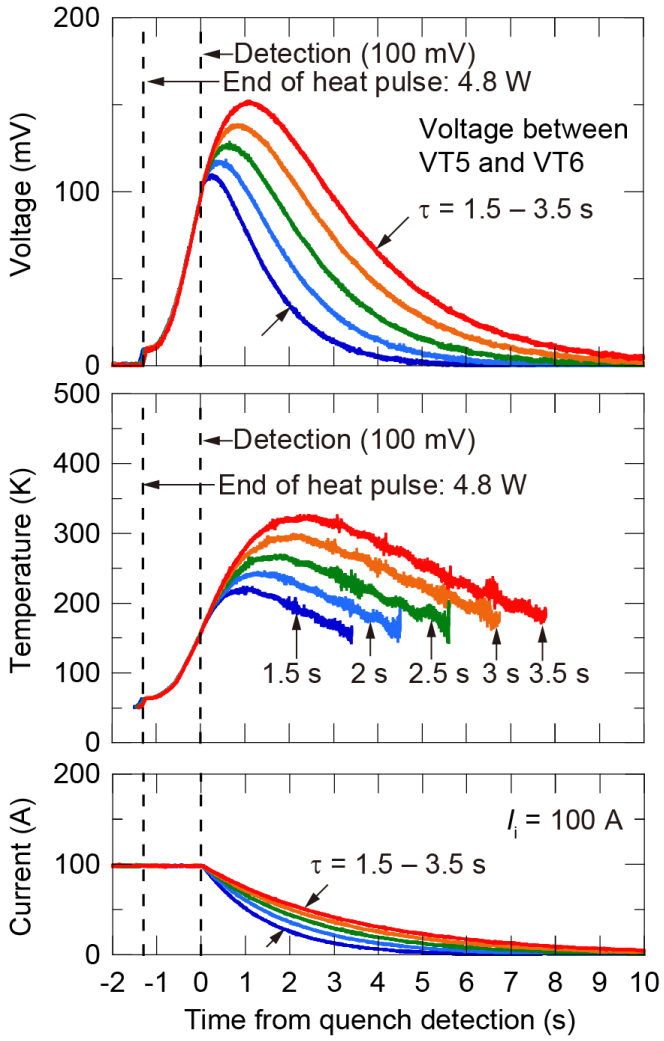

Figure 4.9 Hot-spot temperature derived from $v_{5–6}$ and current waveforms at various time constants of current decrease using SCS4050 (B = 2 T, T_i = 30 K, v_{th} = 100 mV, and t_d = 100 ms; heater power initiating quench is constant; five quench shots are implemented with same short sample) [4.23] © 2019 IEEE.

The time constant of the current decrease was reduced, and the hot-spot temperature was measured. As shown in Figure 4.10, the maximum hot-spot

temperature increases with the time constant of the current decrease. The results when the detection voltage is set at 100 mV is shown by the plots in Figure 4.10(a). When the operating current values are 100, 125, and 150 A, degradation is not observed below 5.5, 2.25, and 1.25 s, respectively. Figure 4.10(b) shows the plots when the detection voltage is set at 20 mV. When the operating current values are 125 and 150 A, degradation is not observed below 3.75 and 2 s, respectively.

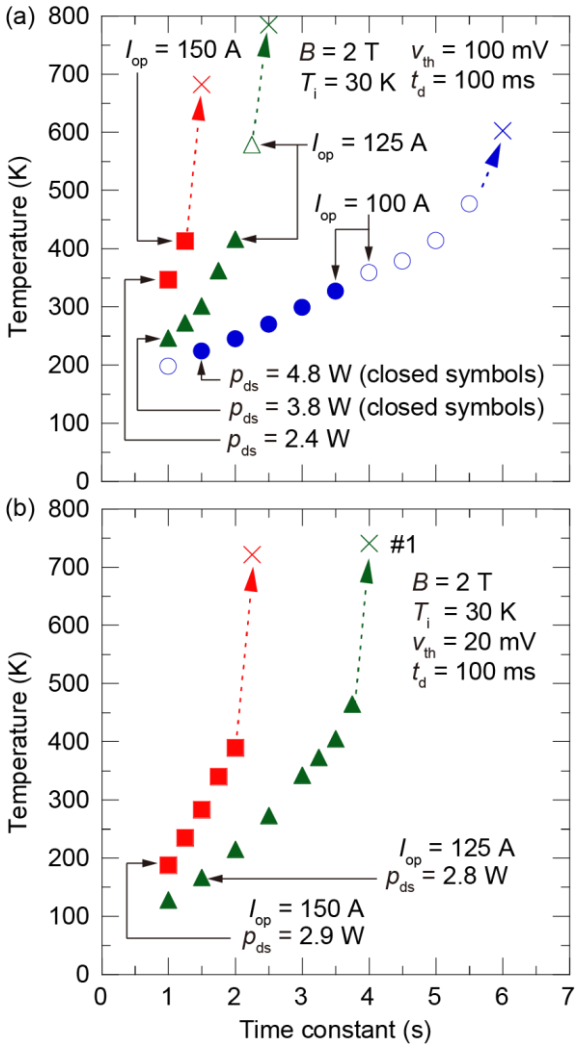

Figure 4.10 Maximum hot-spot temperature vs time constant at different operating currents using SCS4050: (a) detection voltage = 100 mV; (b) detection voltage = 20 mV. Closed/open symbols represent quench not leading to degradation, and crosses represent quench leading to degradation. Heater power of quench shots represented by closed/open symbols are constant/different. Different colors represent various operating currents (different samples). In quench shot of #1 in (b), v_{5-6} was calculated by assuming symmetric voltage distribution along sample because solder at VT5 was melted [4.23]

4.4.3 Threshold Voltage for Quench Detection

Figure 4.11 shows the hot-spot temperature and current waveforms of the sample when the detection voltage is varied. Experiments were performed using a short sample whose critical current was approximately 240 A at 2 T. The heater power values in all the experiments shown in Figure 4.11 are identical.

The detection voltage was increased, and the hot-spot temperature was measured. As shown in Figure 4.12, the maximum hot-spot temperature increases with the detection voltage; however, degradation is not observed when this voltage is less than 175 mV and the operating current is 150 A.

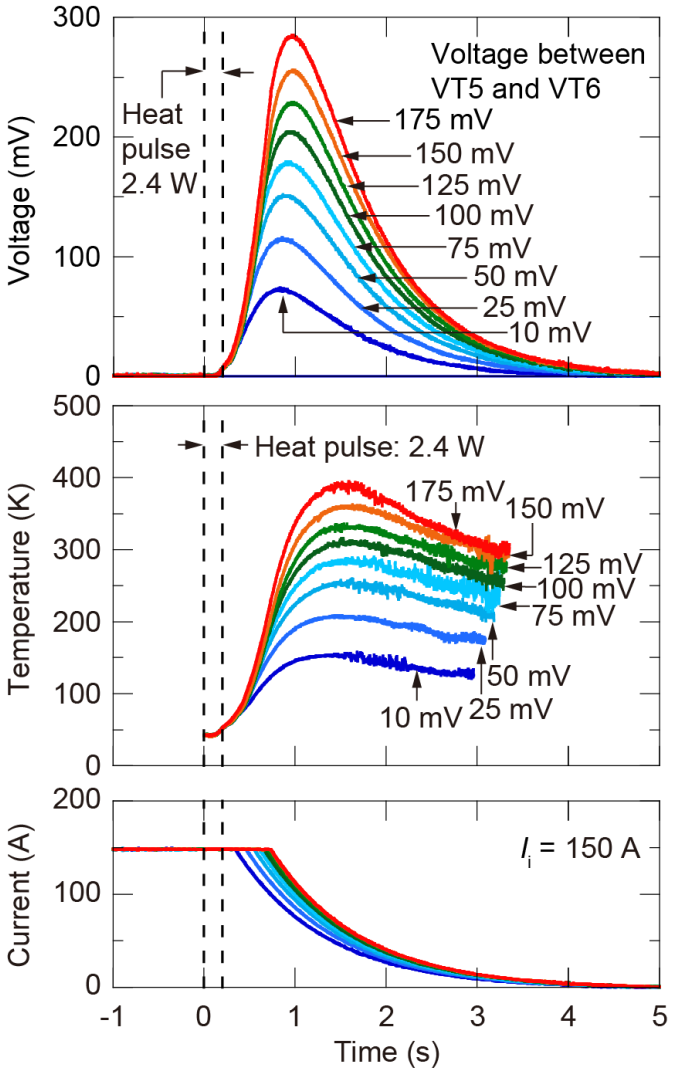

Figure 4.11 Hot-spot temperature derived from $v_{5–6}$ and current waveforms at various detection voltage values using SCS4050 (B = 2 T, T_i = 30 K, t_d = 100 ms, and τ = 1 s; heater power initiating quench constant; eight quench shots are implemented with same short sample) [4.23] © 2019 IEEE.

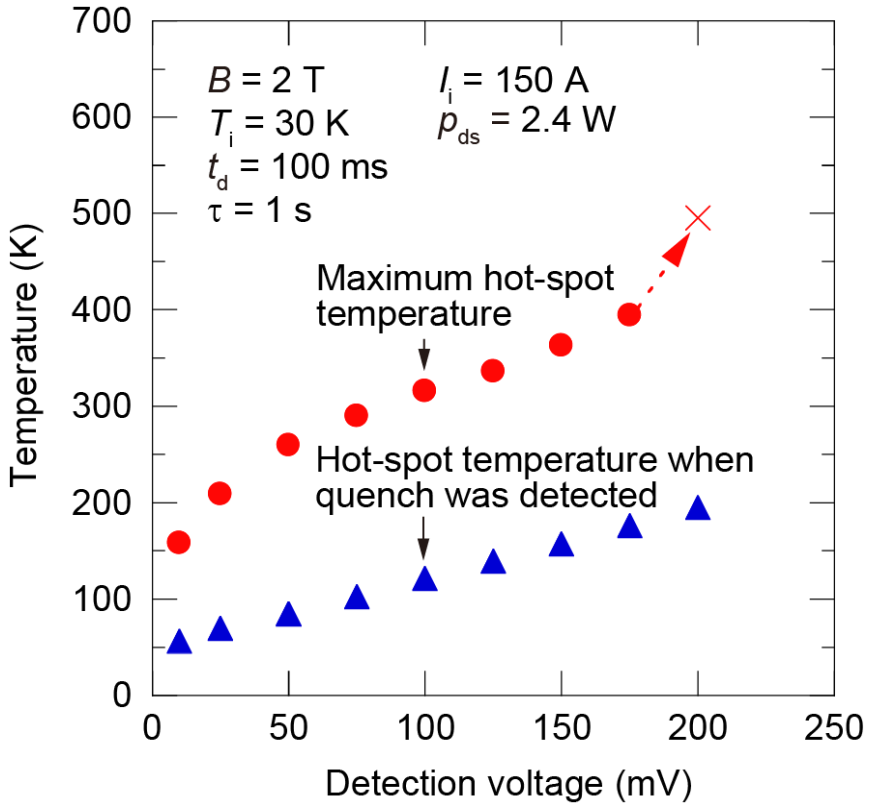

Figure 4.12 Hot-spot temperature derived from v_{5-6} vs detection voltage using SCS4050. Closed symbols represent quench not leading to degradation, and crosses represent quench leading to degradation. Heater power of quench shots represented by closed symbols is constant.

4.4.4 Copper Thickness of Coated Conductor

Figure 4.13 illustrates an example of hot-spot temperature and current waveforms during the quench detection and protection processes using samples with various copper thicknesses. The figure suggests that increasing the copper thickness decreases the maximum hot-spot temperature during the quench detection and protection processes. The experiments were conducted at various operating currents and time constants.

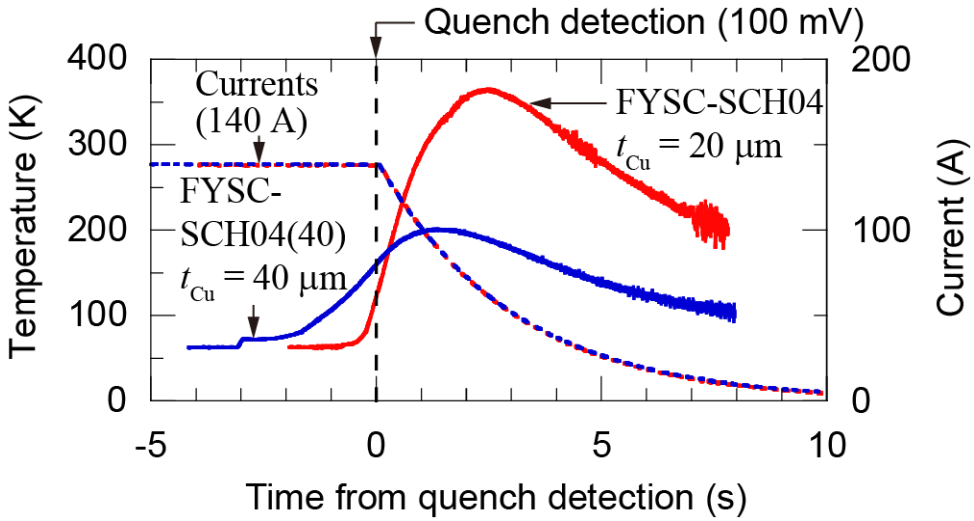

Figure 4.13 Hot-spot temperature and current waveforms of samples with different copper thicknesses (T_i = 45 K, B = 2 T, I_c = ~320 A, I_{op} = 140 A, v_{th} = 100 mV, t_d = 100 ms, and τ = 3 s) [4.24] © 2020 IEEE.

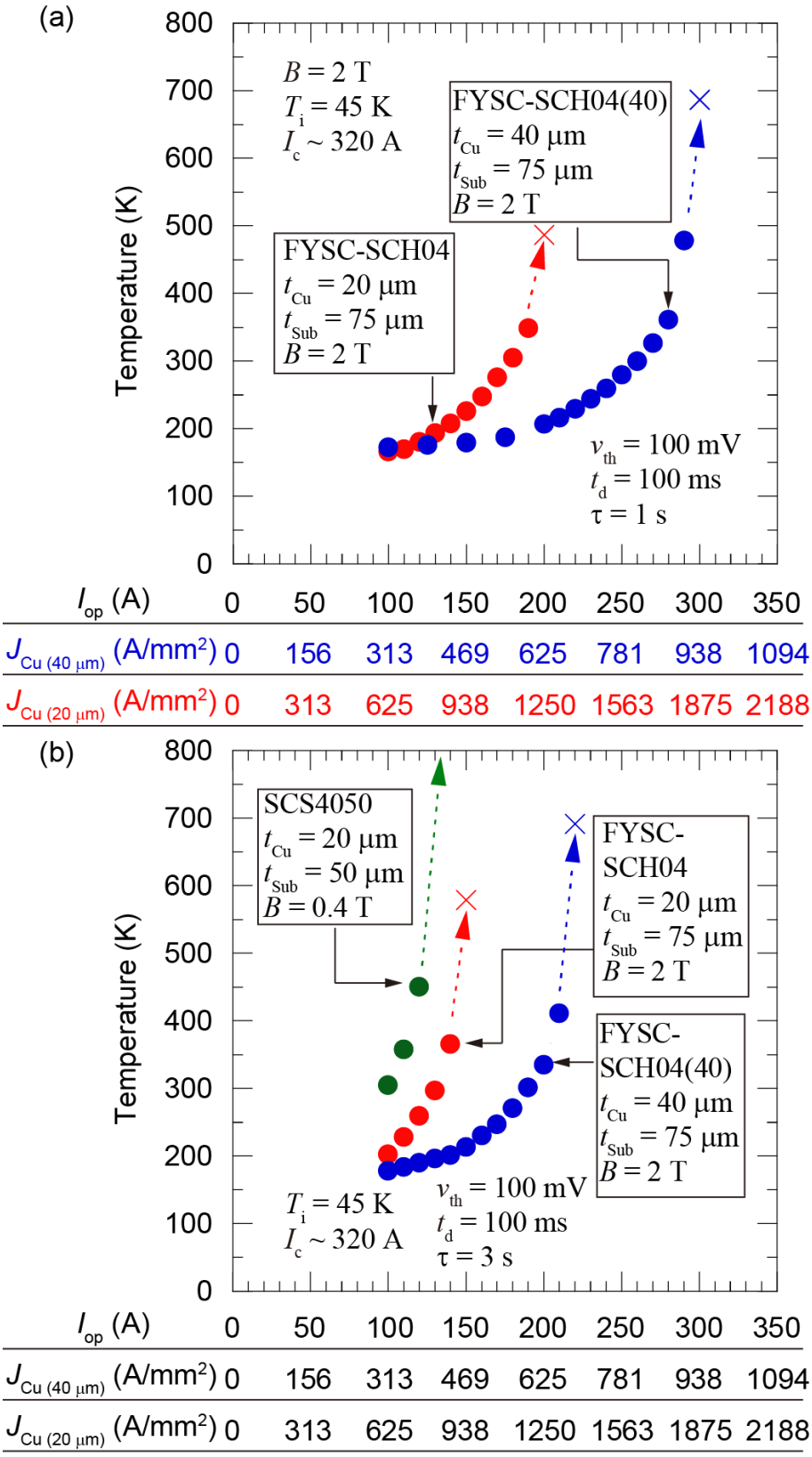

Figure 4.14 Maximum hot-spot temperature vs operating current/current density using samples with different copper thicknesses (T_i = 45 K; t_d = 100 ms): (a) τ = 1 s; (b) τ = 3 s [4.24] © 2020 IEEE.

As depicted in Figure 4.14(a), the experiments are initially performed using FYSC-SCH04 and FYSC-SCH04(40). The time constant of the current decrease is set as 1 s; the current at the first shot is 100 A and then raised incrementally. It is clear that at the same operating current, the maximum hot-spot temperature is lower in FYSC-SCH04(40). For example, at 150 A, the maximum hot-spot temperature in FYSC-SCH04 was 225 K (J_{Cu} = 938 A/mm^2), whereas the maximum hot-spot temperature in FYSC-SCH04(40) was 179 K (J_{Cu} = 469 A/mm^2). As depicted in Figure 4.14(b), similar experiments are conducted when the time constant is set to 3 s using FYSC-SCH04, FYSC-SCH04(40), and SCS4050. Note that in the experiments using SCS4050, the magnetic field was set to 0.4 T to allow the critical current to approach the current values of the other two types of coated conductors. In Figure 4.14, (a) and (b), the experimental results of FYSC-SCH04 and FYSC-SCH04(40) demonstrate the impact of increasing the copper thickness on decreasing the maximum hot-spot temperature owing to the decrease in copper current density as well as the increase in heat capacity. Further, the experimental results of FYSC-SCH04 and SCS4050 suggest that increasing the Hastelloy substrate thickness remarkably impacts the maximum hot-spot temperature (*e.g.*, 202 K in FYSC-SCH04; 305 K in SCS4050 at 100 A) owing to the increase in heat capacity.

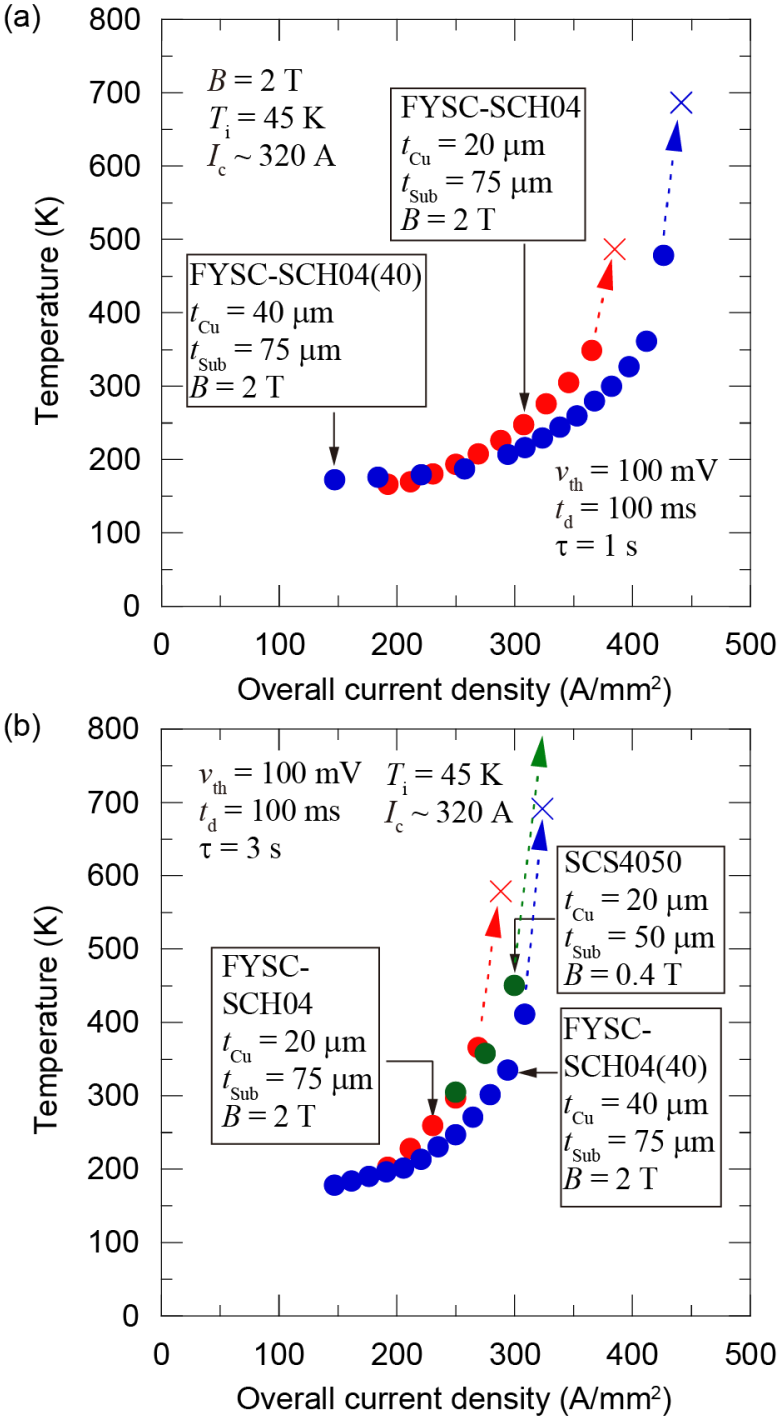

Figure 4.15 Maximum hot-spot temperature vs copper current density using samples with different copper thicknesses (T_i = 45 K; t_d = 100 ms): (a) τ = 1 s; (b) τ = 3 s [4.24] © 2020 IEEE.

Figure 4.14 indicates that increasing the copper thickness of a coated conductor reduces the copper current density and maximum hot-spot temperature. However, increasing the copper thickness of a coated conductor can also reduce the overall current density, which is required to be high in a real magnet. To understand

whether increasing the copper thickness is beneficial, considering the overall current density, the maximum hot-spot temperature values at various overall current densities using various samples are compared, as depicted in Figure 4.15. The experimental results for FYSC-SCH04 and FYSC-SCH04(40), depicted in Figure 4.15, suggest that at the same overall current density, the hot-spot temperature of a coated conductor with a thicker copper stabilizer (40 μm) can be considerably lower. However, as depicted in Figure 4.15(b), the results of FYSC-SCH04 and SCS4050 suggest that the relationship between hot-spot temperature and overall current density does not change substantially by changing the thickness of the Hastelloy substrate.

4.4.5 Monofilament and Multifilament Coated Conductors

Multifilament coated conductors are intrinsically inferior to monofilament coated conductors in terms of robustness against quench/thermal runaway. The quench detection and protection conditions of monofilament coated conductors have been studied using short straight samples. This section describes the comparison of the maximum hot-spot temperature during the quench detection and protection process of multifilament coated conductors with that of monofilament coated conductors at various operating currents. The hot-spot temperature values during the protection process of monofilament sample SCS4050 listed in Table 4.1 are compared with those of the four-filament sample manufactured based on SCS4050 (the specifications are the same as those of monofilament sample SCS4050).

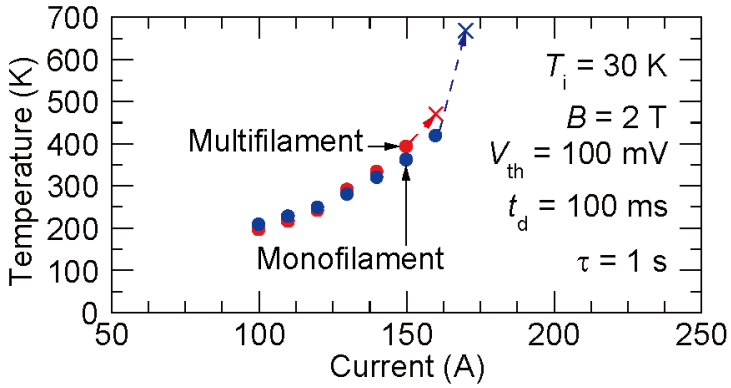

Figure 4.16 Maximum hot-spot temperature of monofilament and multifilament samples at various currents using SCS4050.

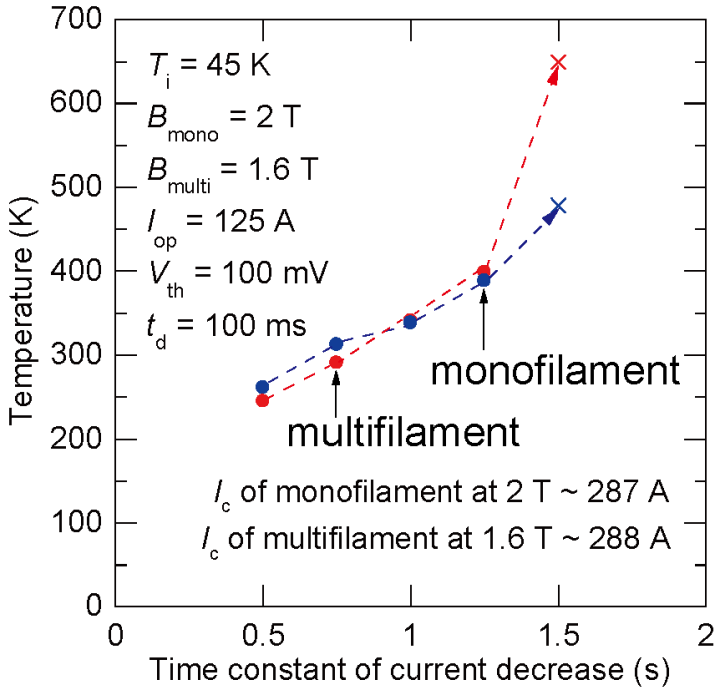

Figure 4.17 Maximum hot-spot temperature of monofilament and multifilament samples with various time constants of current decrease using SCS4030 (substrate thickness: 30 μm).

To understand whether the maximum hot-spot temperatures between monofilament and multifilament coated conductors differ, the maximum hot-spot temperature values are compared at various operating currents, as depicted in Figure 4.16. No significant difference is observed between copper-plated multifilament coated conductors and monofilament coated conductors. The multifilament and monofilament samples degraded at 160 and 170 A, respectively.

Figure 4.17 shows the maximum hot-spot temperature of monofilament and multifilament samples when the operating current is 125 A; the time constant of current decrease, one of the protection conditions, is also varied. In the experiments shown in Figure 4.17, the SCS4030 monofilament and five-filament samples are used (SCS4050 and SCS4030 differ in terms of substrate thickness: SCS4030 is 30 μm thick). In this case, both monofilament and multifilament samples were protected (no degradation was observed after quench) under the time constant of 1.25 s. Moreover, no significant difference in the maximum hot-spot temperature under 1.25 s was observed. Figure 4.16 shows the experimental results, and Figure 4.17 indicates that dividing the superconductor into filaments does not affect the maximum hot-spot temperature during the protection process. In other words, the protection conditions between monofilament and multifilament coated conductors only slightly differ.

4.5 Protectable Conditions for Single Short Sample

In this section, the experimental results of SCS4050 are summarized, and data regarding the conditions for successful quench detection and protection are collated. As mentioned in the previous section, the conditions for the conventional quench detection and protection scheme are represented primarily by the time constant of the current decrease, τ, and the detection voltage, v_{th}. The effect of critical current on quench detection and protection has also attracted interest. This study investigates the effects of these parameters. It focuses on the non-degrading current, I_{nd}, which is the maximum operating current that does not cause degradation after quench, and I_{300K}, at which the maximum hot-spot temperature reaches 300 K. The former is the current at which a particular sample does not degrade; however, this may not apply to the case of real coils. Note that the estimated hot-spot temperatures only directly pertain to coils whose transverse thermal diffusion conditions are similar to those of short-sample experiments.

In Figure 4.18–19, the operating currents (I_{op}) of various quench experiments are shown with circles representing no degradation after quench and crosses representing degradation after quench. Notably, in all the experiments, the delay time before current decrease is 0.1 s, and the initial temperature before quench is 30 K. The axes on the right represent the copper current density (J_{Cu}) (assuming that current flows in the copper during quench) and the overall current density of the coated conductor (J_{op}). Degradation has various modes, such as critical current degradation and burn out. In each figure, two dashed lines, representing I_{nd} and I_{300K}, are drawn.

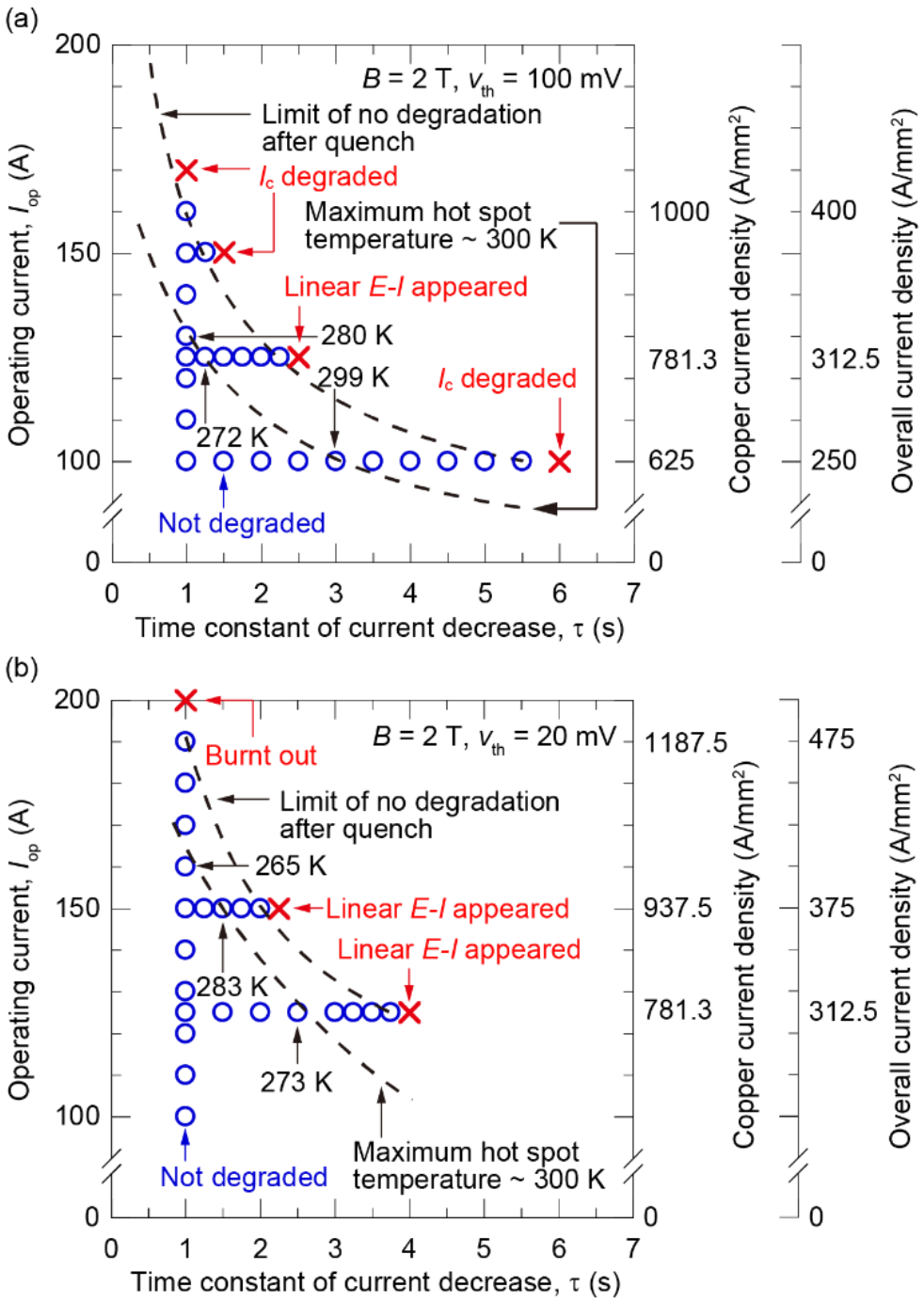

Figure 4.18 Quench experiments at various time constants of current decrease when detection voltage is fixed at 100 mV or 20 mV using SCS4050: (a) detection voltage = 100 mV; (b) detection voltage = 20 mV. Circles represent quench not leading to degradation, and crosses represent quench leading to degradation [4.26].

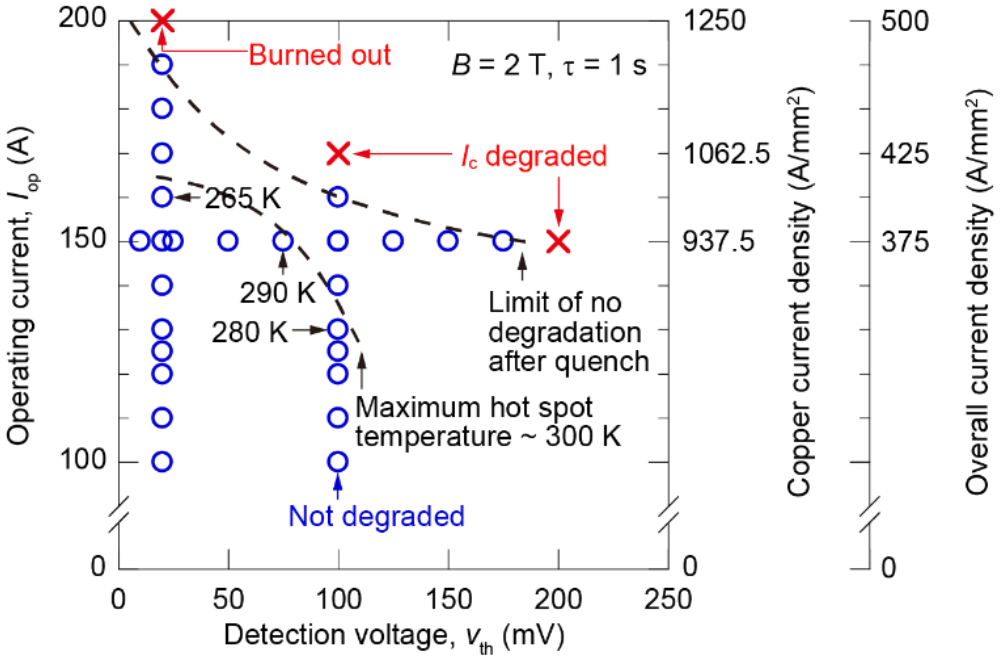

Figure 4.19 Quench experiments at various detection voltages when time constant of current decrease is fixed at 1 s using SCS4050. Circles represent quench not leading to degradation, and crosses represent quench leading to degradation [4.23] © 2019 IEEE.

In Figure 4.18(a), the operating current values (represented by circles and crosses) utilized in the quench experiments are plotted against the time constant of current decrease, where v_{th} = 100 mV, and the critical current is ~240 A at 30 K and 2 T in all the quench experiments. When I_{op} = 100 A (J_{op} = 250 A/mm^2; J_{Cu} = 625 A/mm^2), no degradation is observed after quench if τ is less than 5.5 s; the maximum hot-spot temperature is less than 300 K if τ is below 3 s. Meanwhile, when τ is 1 s, no degradation is observed after quench if I_{op} is less than 160 A (J_{op} = 400 A/mm^2; J_{Cu} = 1000 A/mm^2); the maximum hot-spot temperature is less than 300 K if I_{op} is below 130 A (J_{op} = 325 A/mm^2; J_{Cu} = 812.5 A/mm^2). Figure 4.18(b) shows the same figure but with v_{th} = 20 mV. In this case, at τ of 1 s, no degradation is observed after quench if I_{op} is less than 190 A (J_{op} = 475 A/mm^2; J_{Cu} = 1187.5 A/mm^2); the maximum hot-spot temperature is less than 300 K if I_{op} is below 160 A (J_{op} = 400 A/mm^2; J_{Cu} = 1000 A/mm^2).

As shown in Figure 4.19, the operating currents of quench experiments (circles and crosses) are plotted against the detection voltage, where τ = 1 s, and the critical current is ~240 A at 30 K and 2 T in all the quench experiments. When I_{op} is 150 A (J_{op} = 375 A/mm^2; J_{Cu} = 937.5 A/mm^2), no degradation is observed after quench if v_{th} is below 175 mV; the maximum hot-spot temperature is less than 300 K if v_{th} is below 75 mV.

In this section, the derived conditions for the successful quench detection and protection of short samples are presented; they are I_{op}, τ, and v_{th}. Based on the experimental results shown above, the applicable case studies of the conventional quench detection and protection scheme are subsequently performed.

4.6 Case Studies Applicable to Real Magnets

One concern regarding the applicability of the conventional quench detection and protection scheme is whether the detection voltage can be set to several tens or hundreds of millivolts in real RE-123 coils on a practical scale because of possible noise. In a previous study of the author, the detection voltage was set to 50 mV in a conduction-cooled magnet composed of an RE-123 coated conductor whose total length, rated current, and inductance were 3044 m, 200 A, and 3.3 H, respectively [4.27]. The magnet was operated successfully in a noisy circumstance near a synchrotron. Accordingly, the detection voltage of 50–100 mV is considered feasible.

In this study, the feasibility of replacing the Nb–Ti magnets for a carbon rotating gantry (inductance and operating current of 5–12 H and 130–230 A, respectively) [4.28] with REBCO magnets is investigated. The following conditions are considered in selecting the combination of magnet inductance, magnet operating current, and dump resistor.

1) The maximum terminal voltage must be maintained below 1 kV to avoid electrical breakdown [4.29].
2) The maximum terminal voltage is expressed as the product of the operating current and the resistance of the dump resistor when assuming an exponential current decay.
3) The time constant of current decay is expressed as the ratio of magnet inductance to the resistance of the dump resistor.

Table 4.2 lists examples of feasible magnets whose inductance (L), operating current (I_{op}), overall current density of the coated conductor (J_{op}), and resistance of the dump resistor (R_d) are shown in the first, second, third, and fourth columns, respectively. The maximum terminal voltage (V_{max}), which can be calculated by I_{op} and R_d ($V_{max} = I_{op}/R_d$), is shown in the fifth column. The time constant of current decrease (τ), which can be calculated by L and R_d ($\tau = L/R_d$), is shown in the sixth column. With I_{op}, τ, and v_{th} (detection voltage) listed in the seventh column, the estimated maximum hot-spot temperature (T_{max}) using the data shown in Figures 3.12 and 3.13, is listed in the eighth column. The transverse thermal diffusion conditions of magnets listed in Table 4.2 are assumed to be similar to those of short-

sample experiments. The T_{max} value of all the magnets listed in Table 4.2 can be maintained to less than 300 K using the conventional quench detection and protection scheme.

TABLE 4.2
EXAMPLES OF FEASIBLE MAGNETS WOUND WITH SCS4050 [4.23] © 2019 IEEE

L (H)	I_{op} (A)	J_{op} (A/mm^2)	R_d (Ω)	V_{max} (kV)	τ (s)	v_{th} (mV)	T_{max} (K)
30	100	250	10	1	3	100	< 300
8	125	312.5	8	1	1	100	< 300
20	125	312.5	8	1	2.5	20	< 300
6	150	375	6	0.9	1	75	< 300
6	160	400	6	0.96	1	20	< 300

*Delay time before current decrease = 0.1 s

**J_{op} = operating current / cross-section of coated conductor

4.7 Chapter Summary

With the use of conduction-cooled coated conductors, the increase in the thickness of plated copper was experimentally confirmed to reduce the propagation velocity and suppress the hot-spot temperature. The former can be caused by the reduction in the overall current density, and the latter may result from decreasing the copper current density. The heat capacity of the substrate has a remarkable impact on the hot-spot temperature. The hot-spot temperature values of the coated conductor with a 40-μm-thick plated copper were fundamentally lower than those of the coated conductor with a 20-μm-thick plated copper at the same overall current densities.

The results of the fast-turnaround experiments using short samples of SCS4050 of SuperPower Inc. suggested the applicability of conventional quench detection (using voltage) and protection (with a dump resistor) to RE-123 magnets if the appropriate time constant of current decay and voltage threshold for quench detection were selected. For example, if the hot-spot temperature of 300 K is used, then a magnet wound with a 20-μm copper-plated coated conductor (inductance and operating current (tape current density) are 8 H and 125 A (312.5 A/mm^2), respectively) can be protected. This can be achieved if its quench can be detected at 100 mV, and its energy is dumped to an 8-Ω resistor for which the time constant of current decay is 1 s. In terms of scale, this magnet is similar to Nb–Ti magnets for a carbon rotating gantry, which is operated for real treatments. Notably, the critical current did not affect the hot-spot temperature.

[References]

[4.1] G. Celentano *et al*., "Quench behavior of a conduction cooled $YBa_2Cu_3O_{7-x}$ tape pancake coil," *IEEE Trans. Appl. Supercond.*, vol. 23, no. 3, Jun. 2013, Art no. 4600704.

[4.2] W. J. Lu, J. Fang, D. Li, C. Y. Wu, and L. J. Guo, "The experimental research and analysis on the quench propagation of YBCO coated conductor and coil," *Phys. C*, vol. 484, pp. 153–158, Jan. 2013.

[4.3] F. Trillaud, H. Palanki, U. P. Trociewitz, S. H. Thompson, H. W. Weijers, and J. Schwartz, "Normal zone propagation experiments on HTS composite conductors," *Cryogenics*, vol. 43, no. 3–5, pp. 271–279, 2003.

[4.4] S. Hahn, D. K. Park, J. Bascunan, and Y. Iwasa, "HTS pancake coils without turn-to-turn insulation," *IEEE Trans. Appl. Supercond.*, vol. 21, no. 3, pp. 1592–1595, Jun. 2011.

[4.5] T. Oki *et al.*, "Evaluation on quench protection for no-insulation REBCO pancake coil," *IEEE Trans. Appl. Supercond.*, vol. 26, no. 4, Jun. 2016, Art no. 4702905.

[4.6] T. Lecrevisse, A. Badel, T. Benkel, X. Chaud, P. Fazilleau, and P. Tixador, "Metal-as-insulation variant of no-insulation HTS winding technique: pancake tests under high background magnetic field and high current at 4.2K," *Supercond. Sci. Technol.*, vol. 31, no. 5, May 2018, Art no. 055008.

[4.7] A. Mierau *et al.*, "Testing of series superconducting dipole magnets for the SIS100 synchrotron," *IEEE Trans. Appl. Supercond.*, vol. 29, no. 5, p. 7, Aug 2019, Art no. 4003907.

[4.8] G. Flanagan *et al*., "Evaluation and implementation of high performance real-time signal processing for Rayleigh scattering based quench detection for high field superconducting magnets," in *Proc. Iny. Part. Accel. Conf. 2012*, New Orleans, LA, USA, 2012, pp. 3602–3604.

[4.9] F. Scurti, S. Ishmael, G. Flanagan, and J. Schwartz, "Quench detection for high temperature superconductor magnets: a novel technique based on Rayleigh-backscattering interrogated optical fibers," *Supercond. Sci. Technol.*, vol. 29, no. 3, Mar. 2016, Art no. 03lt01.

[4.10] A. Ishiyama, H. Ueda, Y. Aoki, K. Shikimachi, N. Hirano, and S. Nagaya, "Quench behavior and protection in cryocooler-cooled YBCO pancake coil for SMES," *IEEE Trans. Appl. Supercond.*, vol. 21, no. 3, pp. 2398–2401, Jun. 2011.

[4.11] X. Wang, U. P. Trociewitz, and J. Schwartz, "Critical current

degradation of short $YBa_2Cu_3O_{7-\delta}$ coated conductor due to an unprotected quench," *Supercond. Sci. Technol.*, vol. 24, no. 3, Mar. 2011, Art no. 035006.

[4.12] S. Awaji *et al*., "Hot spot behavior of Y123 coated conductors," *IEEE Trans. Appl. Supercond.*, vol. 22, no. 3, Jun. 2012, Art no. 6601004.

[4.13] H. H. Song, K. Gagnon, and J. Schwartz, "Quench behavior of conduction-cooled $YBa_2Cu_3O_{7-\delta}$ coated conductor pancake coils stabilized with brass or copper," *Supercond. Sci. Technol.*, vol. 23, no. 6, Jun. 2010, Art no. 065021.

[4.14] X. Wang, U. P. Trociewitz, and J. Schwartz, "Self-field quench behaviour of $YBa_2Cu_3O_{7-\delta}$ coated conductors with different stabilizers," *Supercond. Sci. Technol.*, vol. 22, no. 8, Aug. 2009, Art no. 085005.

[4.15] T. Minagawa, Y. Fujimoto, and O. Tsukamoto, "Study on protection of HTS coil against quench due to temperature rise of long part of HTS wires," *IEEE Trans. Appl. Supercond.*, vol. 23, no. 3, Jun. 2013, Art no. 4702004.

[4.16] H. Ueda *et al*., "Quench detection and protection of cryocooler-cooled YBCO pancake coil for SMES," *IEEE Trans. Appl. Supercond.*, vol. 22, no. 3, Jun. 2012, Art no. 4702804.

[4.17] Y. Iwasa, H. Lee, J. R. Fang, and B. Haid, "Quench and recovery of YBCO tape experimental and simulation results," *IEEE Trans. Appl. Supercond.*, vol. 13, no. 2, pp. 1772–1775, Jun. 2003.

[4.18] A. L. Mbaruku, U. P. Trociewitz, X. Wang, and J. Schwartz, "Relationships between conductor damage, quenching and electromechanical behavior in YBCO coated conductors," *IEEE Trans. Appl. Supercond.*, vol. 17, no. 2, pp. 3044–3049, Jun. 2007.

[4.19] Y. Fu, O. Tsukamoto, and M. Furuse, "Copper stabilization of YBCO coated conductor for quench protection," *IEEE Trans. Appl. Supercond.*, vol. 13, no. 2, pp. 1780–1783, Jun. 2003.

[4.20] A. P. Malozemoff, S. Annavarapu, L. Fritzemeier, Q. Li, V. Prunier, M. Rupich, C. Thieme, W. Zhang, A. Goyal, M. Paranthaman, and D. F. Lee, "Low-cost YBCO coated conductor technology," *Supercond. Sci. Technol.*, vol. 13, no. 5, pp. 473–476, May 2000.

[4.21] A. P. Malozemoff, S. Fleshler, M. Rumpich, C. Thieme, X. Li, W. Zhang, A. Otto, J. Maguire, D. Folts, J. Yuan, H-P. Kraemer, W. Schmidt, M. Wohlfart, and H- W. Neumueller, "Progress in high temperature superconductor coated conductors and their applications," *Supercond. Sci. Technol.*, vol. 21, no. 3, Mar. 2008, Art. no. 034005.

[4.22] M. W. Rupich, X. Li, S. Sathyamurthy, C. L. H. Thieme, K. DeMoranville, J. Gannon, and S. Fleshler, "Second generation wire development at AMSC," *IEEE Trans. Appl. Supercond.*, vol. 23, no. 3, Jun. 2013, Art. no. 6601205.

[4.23] X. Luo, S. Inoue, and N. Amemiya, "Experimental study on quench detection and protection conditions of copper-stabilized coated conductors using short samples," *IEEE Trans. Appl. Supercond*., vol. 29, no. 8, Dec. 2019, Art. no. 4703511.

[4.24] X. Luo, S. Inoue, N. Amemiya, "Quench experiments of conduction-cooled coated conductors with various copper-stabilizer thicknesses," *IEEE Trans. Appl. Supercond*., vol. 30, no. 4, Jun. 2020, Art. no. 4700705.

[4.25] M. Daibo, S. Fujita, M. Haraguchi, Y. Iijima, and T. Saitoh, "Evaluation of the normal-zone propagation characteristics of REBCO coated conductors with laminated Cu tape," *IEEE Trans. Appl. Supercond.*, vol. 21, no. 3, pp. 2428–2431, Jun. 2011.

[4.26] X. Luo, S. Inoue, and N. Amemiya, "Experimental study on detection voltage and current-decay time constant enabling protection of conduction-cooled RE-123 coils against quench initiated by transient and local thermal disturbance," Abstracts of CSSJ Conference, vol. 98, p. 4, May 2019.

[4.27] N. Amemiya *et al*., "Test of cryocooler-cooled RE-123 magnet on HIMAC beam line in S-Innovation program," *IEEE Trans. Appl. Supercond.*, vol. 29, no. 5, Aug. 2019, Art no. 4600305.

[4.28] Y. Iwata *et al.*, "Development of curved combined-function superconducting magnets for a heavy-ion rotating-gantry," *IEEE Trans. Appl. Supercond.*, vol. 24, no. 3, Jun. 2014, Art no. 4400505.

[4.29] M. N. Wilson, "Protection by an external resistor," in *Superconducting Magnets*, Oxford, U.K.: Clarendon, 1983, pp. 219–221.

Chapter 5 Protection Conditions Against Thermal Runaway Induced by Continuous Joule Heating

5.1 Chapter Background and Objective

Intrinsically, local defects reduce local critical currents and are unavoidable in a coated conductor even with the use of the most advanced manufacturing technology [5.1]–[5.6]. Additionally, because the magnitude and direction of the magnetic field vary along the length of a coated conductor in a coil, its critical current, which depends on these parameters, also varies [5.7], [5.8]. Further, the local critical current is suppressed by the magnetic field at some parts of the conductor (I_c suppression by magnetic field). Owing to local defects and I_c suppression, the critical current along a conductor in a real coil can be distributed, as shown in Figure 5.1 in which low I_c parts appear. An unexpected temperature rise caused by the cooling system or heating by radiation can occur in the coil in the case of accelerator or fusion magnets. The critical current decreases, and thermal runaway may be initiated at the weakest point at which I_c is lower than the current in other parts of the coil, as shown in Figure 5.1.

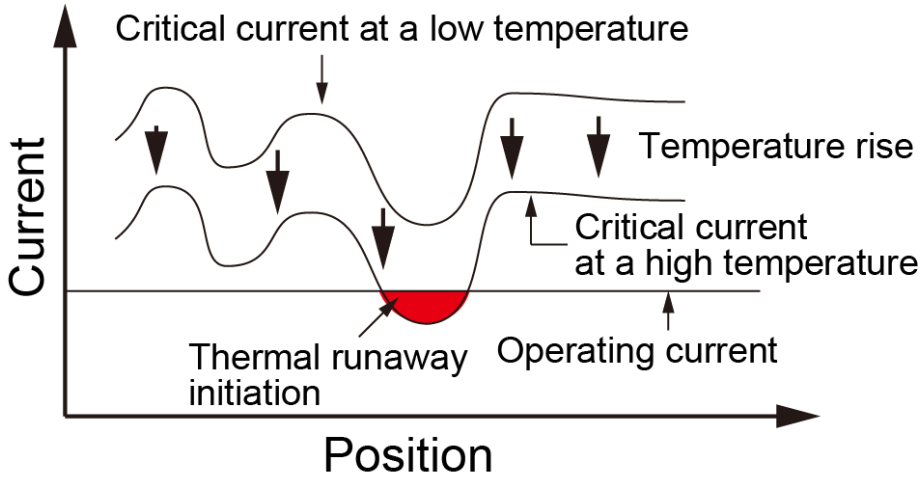

Figure 5.1 Possible distribution of critical current along conductor in real coil and initiation of thermal runaway [5.9] © 2022 IEEE.

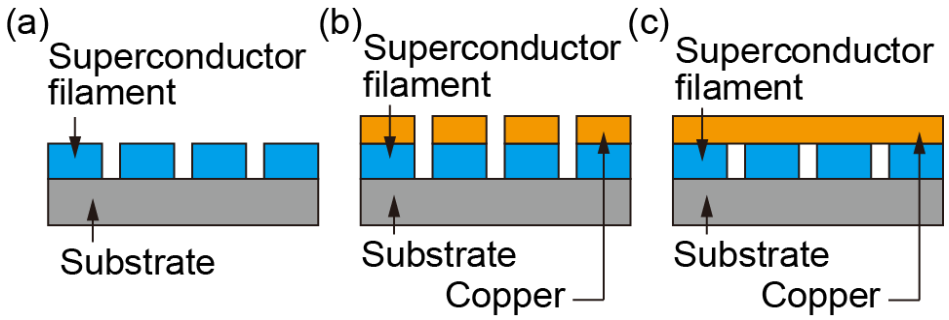

Figure 5.2 Cross-sections of three variations of multifilament coated conductors. (a) Without copper layer; (b) With copper layer on each filament; (c) With copper layer on entire group of filaments [5.9] © 2022 IEEE.

To reduce AC losses and shielding current-induced fields in a coated conductor [5.10]–[5.13], three variations of multifilament coated conductors have been proposed, as shown in Figure 5.2: (a) multifilament coated conductor without copper layer; (b) multifilament coated conductor with copper layer on each filament; (c) multifilament coated conductor with copper layer on the entire group of filaments. When local defects are present in multifilament coated conductors, the current in the filaments with defects is blocked in the coated conductors, as shown in Figure 5.2, (a) and (b). The current can bypass the defects through the copper layer and sound filaments in the coated conductor, as shown in Figure 5.2(c). This study focuses on the thermal runaway of multifilament coated conductor, which is preferable from the viewpoint of current sharing among filaments, as shown in Figure 5.2(c). However, the Joule loss generated in the copper layer by bypassing the current is a concern when compared with monofilament coated conductors because it may initiate thermal runaway and affect protection after detecting thermal runaway.

Numerical and experimental studies on the initiation of thermal runaway in monofilament coated conductors have been conducted [5.14]–[5.22]. However, the initiation of thermal runaway in multifilament coated conductors has not been experimentally studied. Furthermore, previous experimental studies on thermal runaway did not directly discuss the conditions under which the conventional quench detection and protection scheme (*i.e.*, detecting quench/thermal runaway using VTs and dumping the stored energy in an external dump resistor) could be applied [5.23]–[5.33].

The objective of this study is to clarify and compare the behaviors (voltage, current, temperature, etc.) of monofilament and multifilament coated conductors during the following process:

1) initiation process of thermal runaway;
2) detection of and protection against thermal runaway.

In the initiation process of thermal runaway, the voltage/current (in the longitudinal and transverse directions) and thermal runaway currents on the monofilament and multifilament were measured and compared. In the detection and protection process against thermal runaway, the *protectable currents* (below which the conductor can be protected) of monofilament and multifilament coated conductors were determined and compared as thresholds for protecting coated conductors from degradation.

5.2 Sample Information and Experimental Method

5.2.1 Sample Information

The monofilament coated conductors used in this study were the standard SCS4050 copper-plated coated conductors of SuperPower Inc. The multifilament coated conductors used were developed by Furukawa Electric Co., Ltd. and SuperPower Inc. These conductors were based on SCS4050 in which the superconductor layer was divided into five filaments by laser striation and subsequently plated with copper (thickness: 20 μm) [5.10], [5.11]. The detailed specifications of the monofilament and multifilament coated conductors are listed in Table 5.1.

The thermal runaway behaviors (voltage, current, temperature, etc.) of multifilament coated conductors with a copper layer on the entire group of filaments (Figure 5.2(c)) may differ from those of monofilament coated conductors. In a monofilament coated conductor, when a local defect is close to one edge, as shown in Figure 5.3(a), the current can bypass the local defect within its superconductor layer. In this case, no Joule loss occurs because the current only flows in the superconductor layer. However, in the multifilament coated conductor with a copper layer on the entire group of filaments (Figure 5.2(c)), the current may bypass the local defect through the copper layer and sound filaments on the other side if a local defect in a filament is close to one edge, as shown in Figure 5.3(b). The transverse part of the bypass current flowing through the copper layer may generate additional Joule loss and subsequently initiate thermal runaway.

TABLE 5.1
SAMPLE SPECIFICATIONS [5.9] © 2022 IEEE

Properties	SCS4050 (Monofilament)	SCS4050 (Multifilament)
Manufacturer	SuperPower	Furukawa/SuperPower
Number of filaments	1	5
Width	4 mm	4 mm
Entire thickness	0.1 mm	0.1 mm
Plated-copper thickness	20 μm	20 μm
Thickness of silver protective layer	~3.8 μm	~3.8 μm
Thickness of Hastelloy substrate	50 μm	50 μm
Critical current (temperature, magnetic field)	~ 240 A (30 K, 2 T)	~ 240 A (30 K, 2 T)

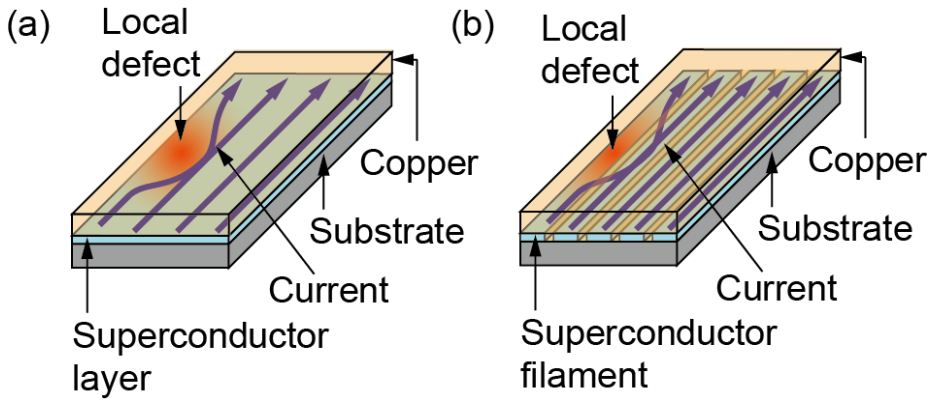

Figure 5.3 Current distribution in coated conductor with local defect: (a) Monofilament coated conductor; (b) Multifilament coated conductor [5.9] © 2022 IEEE.

5.2.2 Experimental Method

This section explains the common experimental methods employed for the experiments presented in **Sections 5.3** and **5.4**.

Instead of using expensive coils, the experiments are conducted using short samples of monofilament and multifilament coated conductors. The effective length between the two copper terminals injecting current is 180 mm, as shown in Figure 5.4. In all the experiments, the samples are conduction-cooled by a cryocooler, and their temperature is PID-controlled at 30 K according to the temperature measured by sensors CX1 and CX2 (Figure 5.4) and the heaters (Figure 3.3) near the copper terminals. The side closer to the superconductor layer

of the tape-shaped coated conductor faces a vacuum, and the other side is attached to a GFRP sample holder using epoxy resin and polyimide tape. In this study, all VTs were made on the side close to the superconductor layer. A magnetic field perpendicular to the wide face of the sample was applied to control the critical current.

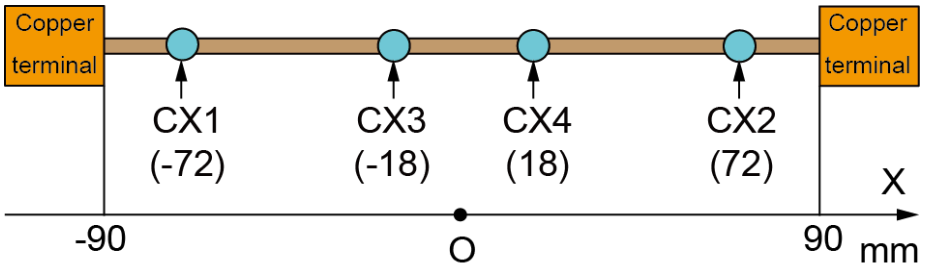

Figure 5.4 Sample layout and temperature sensor positions (CX*i*: Cernox temperature sensor). Numbers in parentheses indicate relative positions to longitudinal center of short sample (unit: mm) [5.9] © 2022 IEEE.

To simulate the thermal runaway initiating at the weakest point (I_c is lower than the current in other parts) in a real coil (Figure 5.1) using a short sample, a local defect is artificially created at the longitudinal center of the sample; the details are explained in **Sections 5.3** and **5.4**.

A thermal runaway is initiated by increasing the current stepwise. The current was increased and then held constant for a certain time (holding time: 300 s or 30 min) to verify whether thermal runaway occurred. Otherwise, the current is repeatedly increased until thermal runaway is detected. Thermal runaway has occurred if the voltage across the entire sample exceeds 20 mV. Here, the thermal runaway current is discussed using *300 s-thermal runaway current* or *30 min-thermal runaway current*, which is defined as the current at which thermal runaway initiates in 300 s or 30 min after the current reaches this value.

5.3 Initiation of Thermal Runaway in Monofilament and Multifilament Coated Conductors

5.3.1 Purpose of Experiments

In a multifilament coated conductor, the manufacturing process may cause local defects in certain filaments. Here, the focus is a multifilament coated conductor with a copper layer on the entire group of filaments (Figure 5.2(c)) in which the current can bypass the local defects through the copper layer and sound filaments. Compared with a monofilament coated conductor, the Joule loss generated in the

copper layer by the bypassing current (transverse current through the copper layer) is a concern because it may affect the initiation of thermal runaway.

The objectives of the experiments presented in this section are as follows:

1) to confirm the bypass of current through the copper layer and prevent the defect from blocking the current;
2) to determine how the additional Joule loss caused by bypassing the current through the copper layer affects the initiation of thermal runaway in a multifilament coated conductor.

5.3.2 Sample Layout and Experimental Procedure

To create a local defect in the filament close to one edge of the sample, as shown in Figure 5.3, and to initiate thermal runaway at the longitudinal center of the sample, the monofilament/multifilament samples are pressed using a drill bit near the a3–a4 VT section, as shown in Figure 5.5 (the area of the degraded superconductor layer might be larger than the Ø0.7-mm section shown in Figure 5.5 because the superconductor layer near the pressed area might also suffer some stress). The purpose of creating a local defect was to simulate the situation in Figure 5.3 (caused by the manufacturing process) and not to study the conductor with this particular damage.

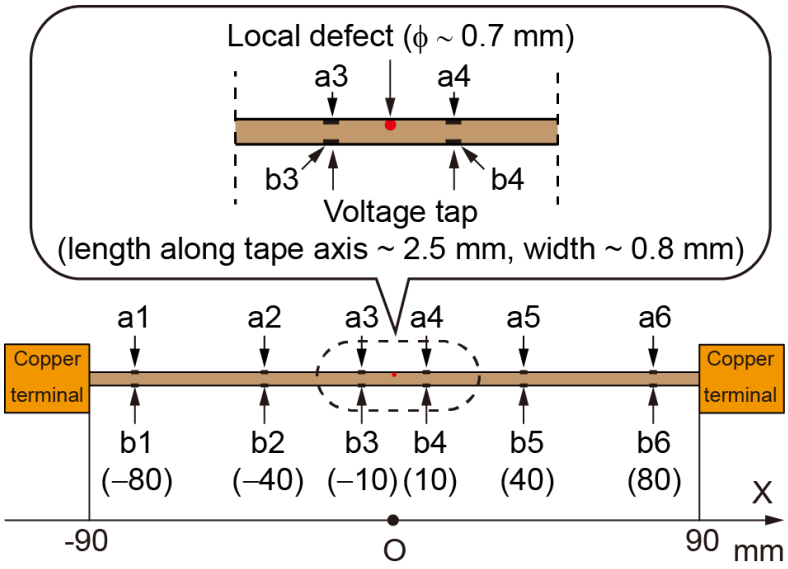

Figure 5.5 Positions and geometry of voltage taps attached to edges of sample (a*i*/b*i*: voltage tap). Numbers in parentheses are relative positions to longitudinal center of short sample (unit: mm) [5.9] © 2022 IEEE.

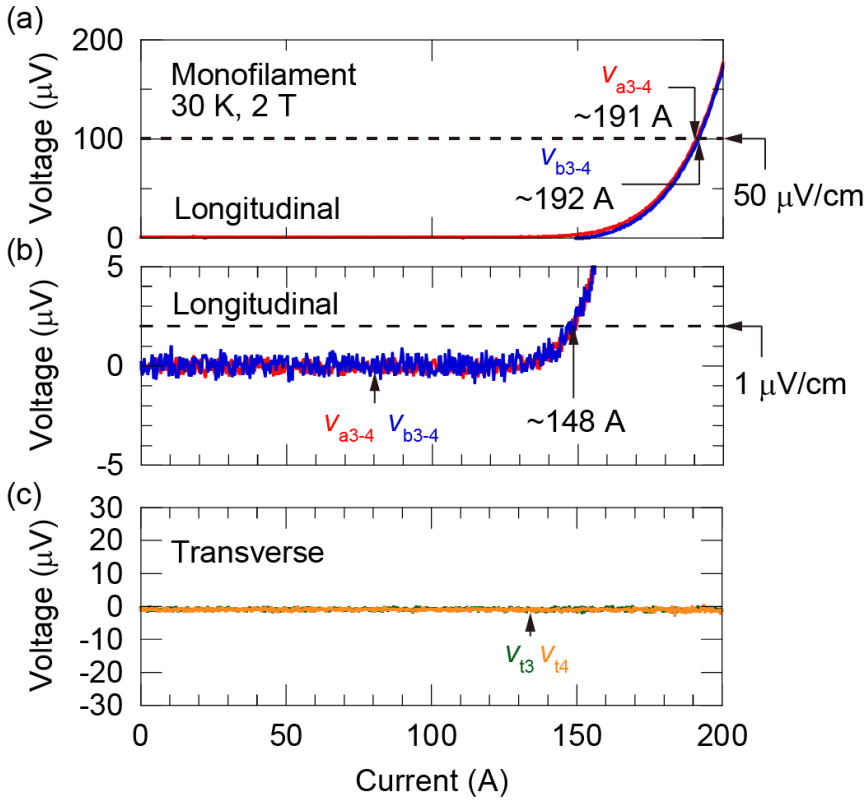

Figure 5.6 Voltage–current characteristics of monofilament sample with local defect at 30 K and 2 T. (a) Voltage in longitudinal direction. (b) Voltage in longitudinal direction (enlarged). (c) Voltage in transverse direction. ($v_{am–n}$: voltage between tap a*m* and a*n*; $v_{bm–n}$: voltage between tap b*m* and b*n*; v_{ti}: voltage between tap a*i* and b*i*) [5.9] © 2022 IEEE.

The position of the voltage taps of monofilament/multifilament samples in this part of the experiments are shown in Figure 5.5. The taps were attached to the edges of samples (from a1 to a6 on one side and from b1 to b6 on the opposite side) to measure the longitudinal voltages, $v_{am–n}$ and $v_{bm–n}$ (i.e., between taps a*m* and a*n* and between b*m* and b*n*, respectively), as well as transverse voltage, v_{ti} (between taps a*i* and b*i*). The length and width of each voltage tap's length along the tape axis were ~2.5 and its width was ~0.8 mm, respectively. In principle, an instrument for voltage measurements detects the potential (voltage) at the location where the fine signal wire from the instrument is attached. Note that a small wire cross-section and high input impedance of the instrument are important because the entire volume of the signal wire must be equipotential. If the signal wire is attached to a large solder spot or a large metal tip (if any) on a sample, then the instrument measures the potential (voltage) at the solder spot or metal tip where the signal wire is attached rather than the sample potential. In this case, the measured voltage might be affected by the voltage drop caused by the current flowing inside the solder spot

or metal tip. Therefore, a smaller solder spot (without any metal tip) is better for more precise measurements. The transverse current in multifilament coated conductors is calculated from the transverse voltage and transverse conductance of filaments. The process for deriving the transverse conductance is described in **Section 5.8 (Appendix)**.

All the experiments presented in **Section 5.3** have been conducted at 30 K and 2 T. The voltage–current (V–I) characteristics of a monofilament sample with local defects are illustrated in Figure 5.5 As shown in Figure 5.6, (a) and (b), the longitudinal voltages, $v_{a3–4}$ and $v_{b3–4}$, on the opposite side are virtually the same. In Figure 5.6(c), the transverse voltages, v_{t3} and v_{t4}, are approximately zero, suggesting that no current flows in the copper layer in the transverse direction of the monofilament sample.

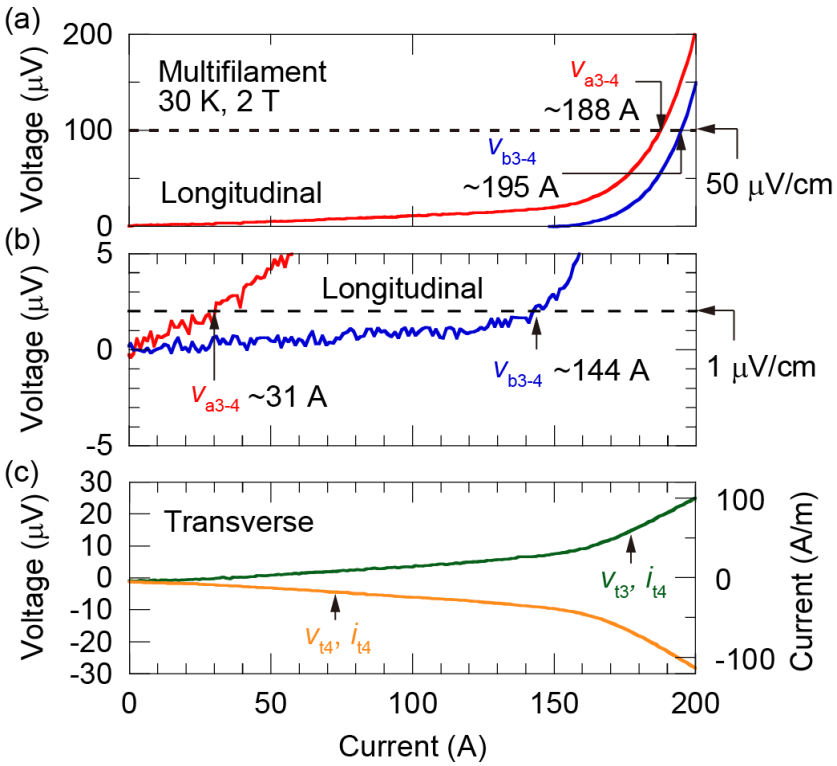

Figure 5.7 Voltage–current characteristics of multifilament sample with local defect at 30 K and 2 T. (a) Voltage in longitudinal direction. (b) Voltage in longitudinal direction (enlarged). (c) Voltage/current in transverse direction. ($v_{am–n}$: voltage between taps am and an; $v_{bm–n}$: voltage between taps bm and bn; v_{ti}/i_{ti}: voltage/current between taps ai and bi) [5.9] © 2022 IEEE.

The V–I characteristics of the multifilament sample with local defects are shown in Figure 5.7. As shown in Figure 5.7, (a) and (b), the longitudinal voltage, $v_{a3–4}$ between taps a3 and a4 (close to the local defect), is higher than longitudinal voltage

v_{b3-4} on the opposite side. In other words, the conductor is not equipotential laterally. In the transverse direction, the voltages, v_{t3} and v_{t4}, shown in Figure 5.7(c) suggest that transverse currents flow through the copper layer in the a3→b3 and b4→a4 directions. The sample currents when the electric fields between a3–a4 and b3–b4 reach 1 μV/cm (the standard criterion for defining critical current) are 31 and 144 A, respectively. In this case, because the concept of critical current implicitly assumes that a conductor is equipotential in its lateral cross-section, we might be not able to define a unique critical current in this case. As a reference, currents reaching a higher electric field of 50 μV/cm, for example, are less dependent on the arrangements of voltage taps (188 A and 195 A, respectively), because the large electric field appeared in the entire cross section of the conductor, and the contribution of the transverse voltage became negligible. The axis on the right in Figure 5.7(c) is the scale of the transverse current in the unit length along the coated conductor calculated from v_{t3}, v_{t4}, and transverse conductance (4.03×10^9 S/m) across four striations among the filaments (**Section 5.8, Appendix**).

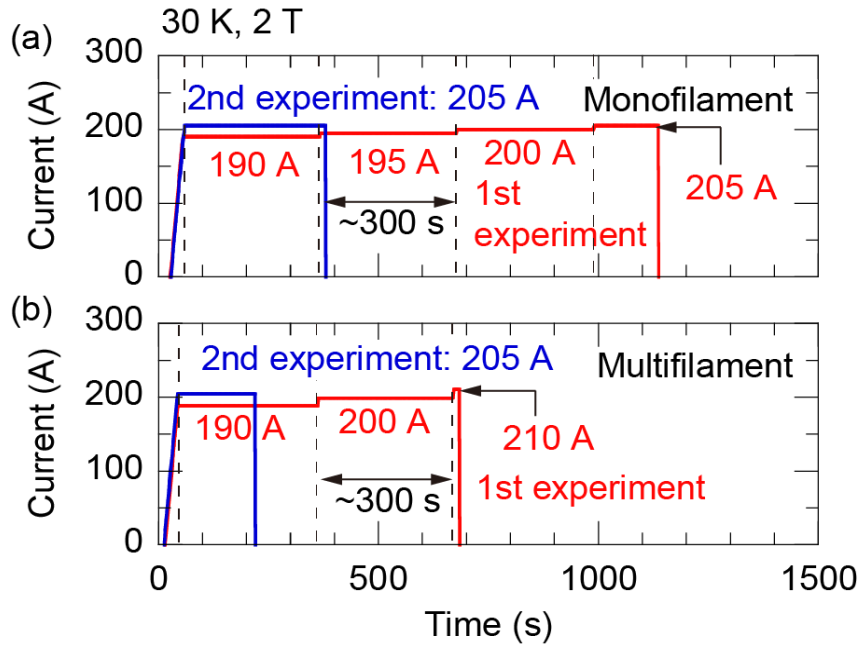

Figure 5.8 Processes for determining *300-s thermal runaway currents*: (a) Monofilament sample; (b) Multifilament sample [5.9] © 2022 IEEE.

To clarify how the additional Joule loss (generated by the transverse current through the copper layer) affects the initiation of thermal runaway in a multifilament coated conductor, the *300-s thermal runaway current* of a multifilament coated conductor is compared with that of a monofilament coated conductor. Note that the local defect was created close to the edge of each sample. The process for determining the *300-s thermal runaway current* values is shown by

the first experiment in Figure 5.8. After determining these values, the second experiment in the same figure was repeatedly conducted at the determined *300-s thermal runaway current* (or a slightly lower current value) to examine the thermal runaway process in detail. Depending on the cooling condition, the thermal runaway current may differ in a real coil.

5.3.3 Experimental Results

Figures 5.9 and 5.10 show the voltage/current examples of monofilament and multifilament samples when no thermal runaway is detected in 300 s (after the current reaches 190 A (Figure 5.8) in the first experiment), respectively. In both monofilament and multifilament samples, the longitudinal voltages, $v_{a3–4}$ and $v_{b3–4}$, are virtually stable after the current reaches 190 A, as shown in Figures 5.9(a) and 5.10(a), respectively. This suggests that the temperatures at the longitudinal centers of these two samples are stable. Transverse voltages/currents (several tens of amperes per meter) are observed in the multifilament sample, as shown in Figure 5.10(b). In this case, the effect of the additional Joule loss generated by the transverse current through the copper layer was removed by the cryocooler; consequently, thermal runaway was not initiated in the multifilament sample.

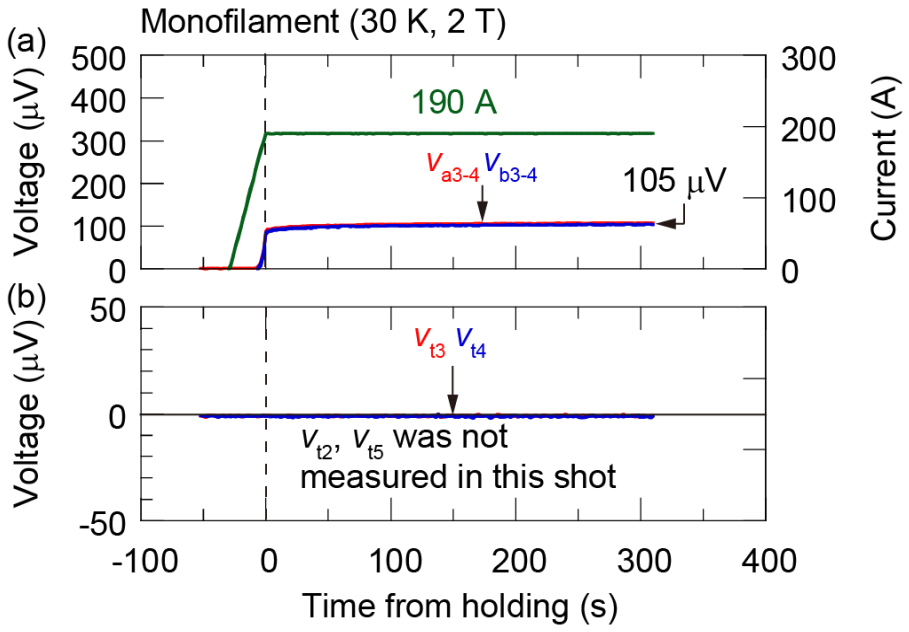

Figure 5.9 Example of voltage and current of monofilament sample with local defect at 190 A, 30 K, and 2 T (no thermal runaway initiates in 300 s): (a) Voltage in longitudinal direction; (b) Voltage in transverse direction. (after current reaches 190 A in Figure 5.8(a), first experiment; $v_{am–n}$: voltage between taps a*m* and a*n*; $v_{bm–n}$: voltage between taps b*m* and b*n*; v_{ti}: voltage between taps a*i* and b*i*) [5.9] © 2022 IEEE.

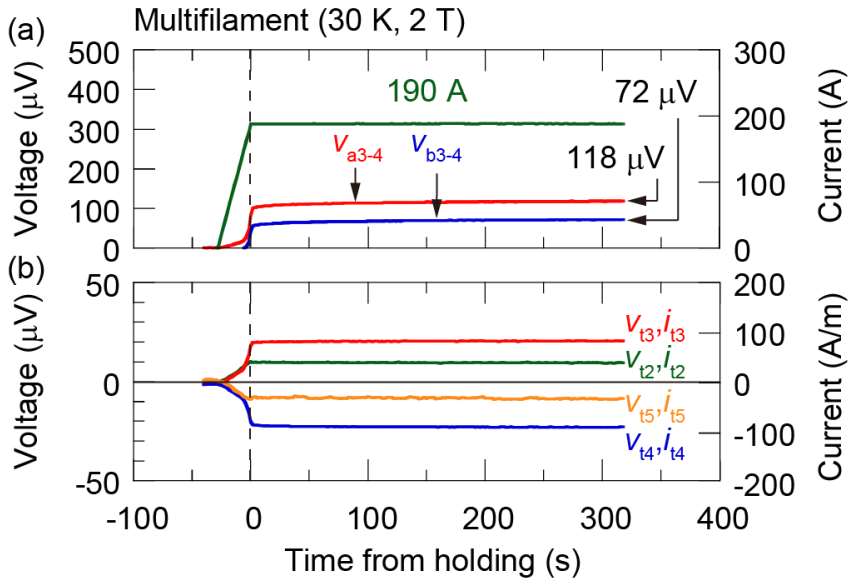

Figure 5.10 Example of voltage and current of multifilament sample with local defect at 190 A, 30 K, and 2 T (no thermal runaway initiates in 300 s). (a) Voltage in longitudinal direction. (b) Voltage and current in transverse direction (after current reaches 190 A in Figure 5.8(b), first experiment; v_{am-n}: voltage between taps a*m* and a*n*; v_{bm-n}: voltage between taps b*m* and b*n*; v_{ti}/i_{ti}: voltage/current between taps a*i* and b*i*) [5.9] © 2022 IEEE.

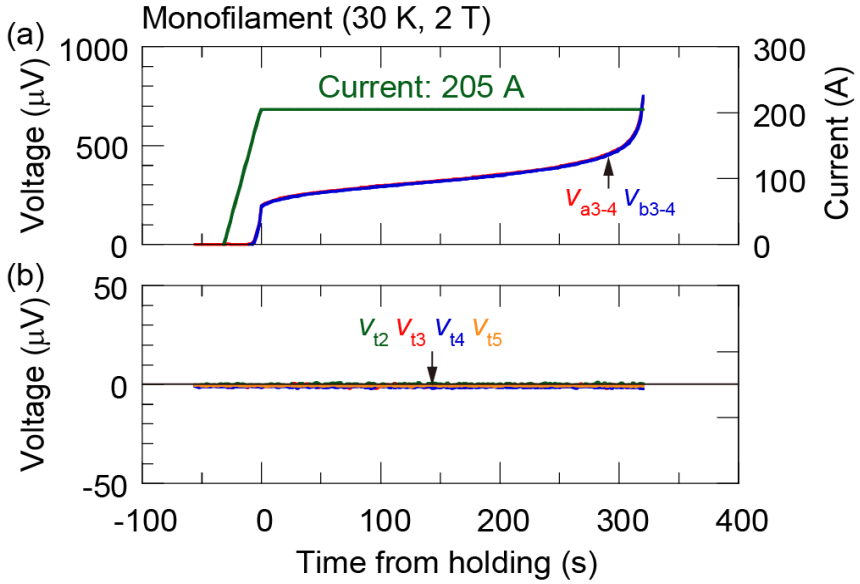

Figure 5.11 Example of voltage and current of monofilament sample with local defect at 205 A, 30 K, and 2 T (thermal runaway initiated). (a) Voltage in longitudinal direction; (b) Voltages in transverse direction (one shot of repeated experiments shown in Figure 5.8(a), second experiment; v_{am-n}: voltage between taps a*m* and a*n*; v_{bm-n}: voltage between taps b*m* and b*n*; v_{ti}: voltage between taps a*i* and b*i*) [5.9] © 2022 IEEE.

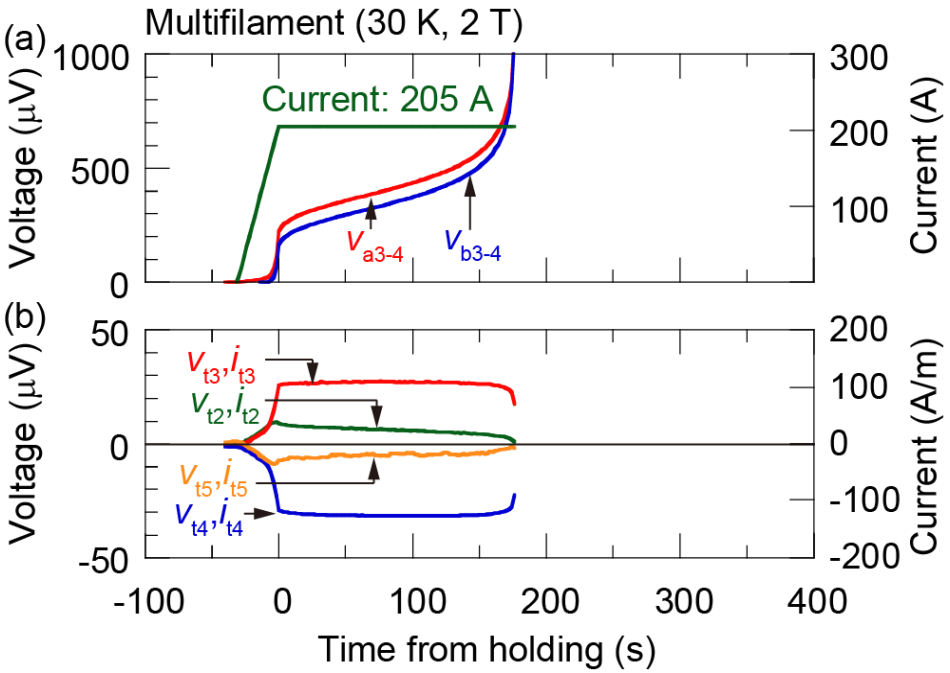

Figure 5.12 Example of voltage and current of multifilament sample with local defect at 205 A, 30 K, and 2 T (thermal runaway initiated). (a) Voltages in longitudinal direction; (b) Voltages/currents in transverse direction (after current reaches 205 A in Figure 5.8(b), second experiment; v_{am-n}: voltage between taps a*m* and a*n*; v_{bm-n}: voltage between taps b*m* and b*n*; v_{ti}/i_{ti}: voltage/current between taps a*i* and b*i*) [5.9] © 2022 IEEE.

Figures 5.11 and 5.12 show the examples of voltages/currents of monofilament and multifilament samples when thermal runaway is detected (operating current: 205 A), respectively. In the monofilament (Figure 5.11) and multifilament (Figure 5.12) samples, thermal runaway was initiated at approximately 300 and 200 s after the current reached 205 A, respectively. The transverse voltages/currents (v_{t2}/i_{t2}, v_{t3}/i_{t3}, v_{t4}/i_{t4}, and v_{t5}/i_{t5}) shown in Figure 5.12(b) suggest that before thermal runaway is detected, the transverse current flows through the copper layer (several tens of amperes per meter) in the multifilament sample. The additional Joule loss generated by this transverse current might have caused the earlier initiation of thermal runaway in the multifilament coated conductor.

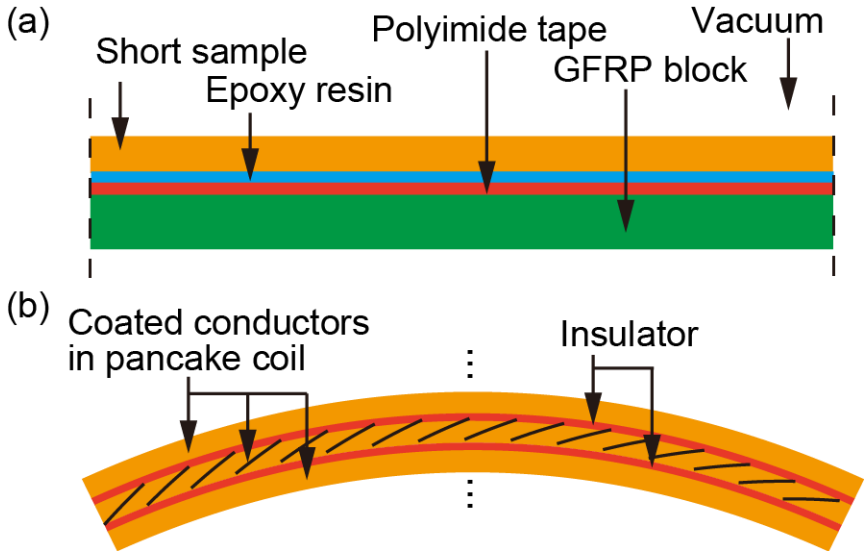

Figure 5.13 Construction of short samples and coated conductors in pancake coil across their thicknesses: (a) Short sample; (b) Coated conductors in middle turns of pancake coil [5.9] © 2022 IEEE.

The initiation of thermal runaways in short samples may differ from that in real coils. The cooling conditions of conductors in short samples and real coils may also vary. For example, as shown in Figure 5.13, (a) in a short sample, the conductor is mainly cooled by another side through epoxy resin, polyimide tape, and GFRP sample holder because one side of the tape-shaped conductor faces a vacuum. (b) In an insulated pancake coil, the tape-shaped conductor in the middle turns can be cooled from two sides through insulators and other turns of the conductor. In real coils wound with multifilament coated conductors, the Joule loss generated by the transverse current among filaments might differ from that in short samples. The possible current distribution in a multifilament coated conductor with a local defect is shown in Figure 5.14. In real coils, the bypassing current diffuses in longer parts because the conductors are considerably longer than those in short samples, as shown in Figure 5.14(b). Moreover, the transverse current density is smaller than that in short samples. Because the transverse resistance is lower in a longer conductor, the total Joule loss in real coils is smaller than that in short samples when bypassing the same amount of current. Compared with short samples, because both the localized Joule loss (determined by transverse current density) and total Joule loss should be smaller, the bypassing current does not significantly affect the thermal runaway current in real coils.

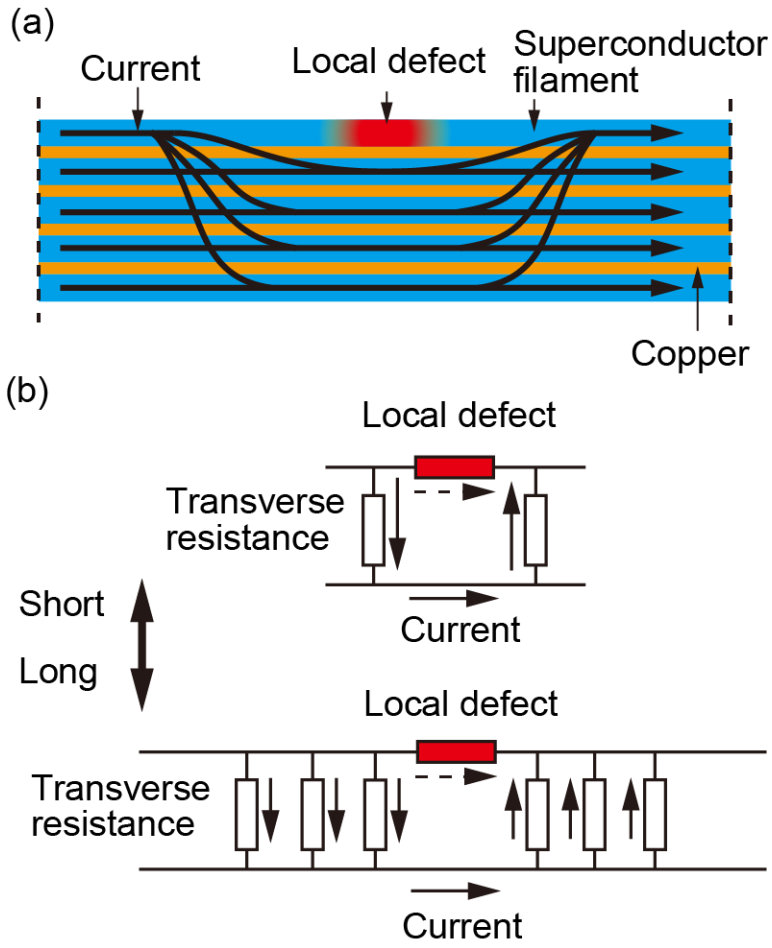

Figure 5.14 Possible current distribution in multifilament coated conductor with local defect: (a) Current distribution among superconductor filaments; (b) Equivalent circuit [5.9] © 2022 IEEE.

5.4 Detection and Protection Against Thermal Runaway in Monofilament and Multifilament Coated Conductors

5.4.1 Purpose of Experiments

The conventional quench/thermal runaway detection and protection processes are widely used in superconducting coils. The voltage across a superconducting coil is monitored by VTs. If this voltage exceeds a certain voltage threshold (i.e., detection voltage), then a circuit breaker is activated. Subsequently, the coil current is transferred to the external dump resistor and decays exponentially with a time constant equal to the coil inductance/resistance of the dump resistor [5.26].

In a real coil, the initiation of thermal runaway is determined by whether the Joule loss power is greater than the cooling power. Under certain cooling conditions, the thermal runaway current is determined by the critical current, which depends on the temperature and magnetic field distribution in a real coil. This is because the

amount of Joule loss is determined by the amount of current flowing in the copper layer (operating current – critical current based on the current-sharing model). In the experiments, the detection of and protection against thermal runaway at various currents influenced by critical currents are investigated.

The purpose of this chapter is to determine whether significant differences in the threshold for protecting monofilament and multifilament coated conductors against degradation exist. This is achieved by comparing the hot-spot temperature and *protectable current* between these two conductors using the conventional detection and protection method.

5.4.2 Sample Layout and Experimental Procedure

The positions and geometry of VTs of monofilament samples are shown in Figure 5.15, whereas those of the multifilament are the same as those shown in Figure 5.3. In the monofilament samples (Figure 5.15), the length and width of each VT along the tape width are ~4 and ~1 mm, respectively. To determine the location at which thermal runaway initiates and easily controls the *300-s thermal runaway current*, a local and uniform defect is created across the width of a coated conductor by bending the samples using a rod, as shown in Figure 5.16. Note that all the defects in the sample were created by bending to control the critical current easily instead of pressing using a drill bit (Figure 5). With respect to thermal runaway detection and protection, the samples with different types of defects are not expected to differ because most of the current flows in the copper layer after thermal runaway.

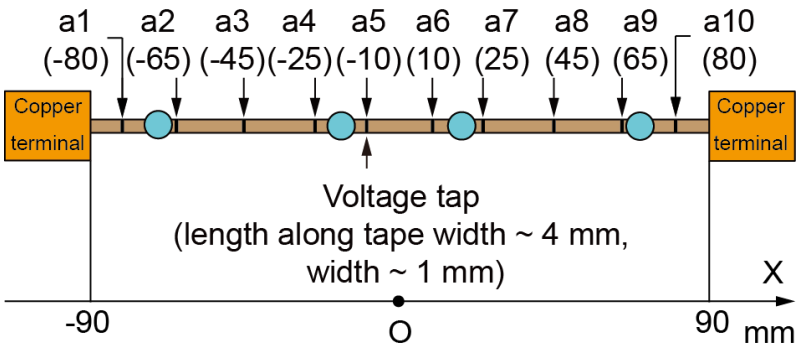

Figure 5.15 Positions and geometry of voltage taps of monofilament sample in thermal runaway detection and protection experiments (a*i*: voltage tap). Numbers in parentheses are relative positions to longitudinal center of short sample (unit: mm) [5.9] © 2022 IEEE.

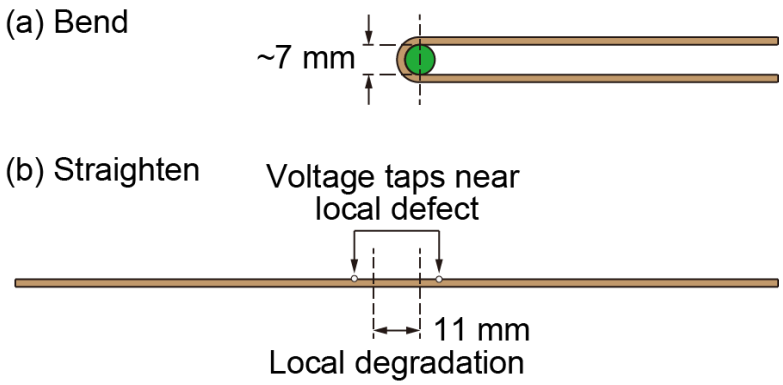

Figure 5.16 Side view of sample with local defect (by bending): (a) Sample bent to generate local and uniform defect across its width (~11 mm long); (b) Straight sample [5.9] © 2022 IEEE.

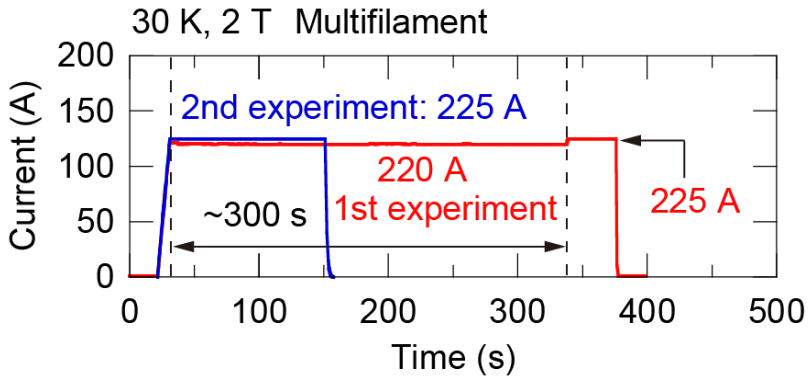

Figure 5.17 Example of processes to determine *300-s thermal runaway currents* in multifilament sample in thermal runaway detection and protection experiments (30 K and 2 T) [5.9] © 2022 IEEE.

Thermal runaway currents were determined using the method introduced in **Section 5.2.2**. The holding times were different in the experiments using monofilament conductors (~30 min) and multifilament conductors (300 s). Although the difference in holding time influences the thermal runaway currents, it is controlled by varying the applied magnetic fields, which change the critical currents. As shown in Figure 5.17, for a multifilament sample, after determining the thermal runaway current in the first experiment, the second experiment is conducted at the determined thermal runaway current to determine whether the conductor can be protected at this current. In the second experiment, an FPGA was used to monitor the voltage and control the output of power supply [5.26]. Once the monitored voltage across the entire sample ($v_{a1\text{-}10}$ in monofilament sample, $v_{a1\text{-}6}$ in multifilament sample) reached a detection voltage (v_{th} = 100 mV, simulating thermal runaway / quench detection), after a period of delay (t_d = 100 ms,

simulating the time required for detection in a real coil and for activating the circuit breaker), the sample current decreased exponentially (τ = 1 s, simulating current decay by the dump resistor while neglecting the normal resistance of the coated conductor). The critical current and n values before and after thermal runaway were compared to determine whether the sample was successfully protected.

The hot-spot temperature during the detection of and protection against quench/thermal runaway was calculated from the voltage at the center of the sample ($v_{a5–6}$ in the monofilament sample and $v_{a3–4}$ in the multifilament sample, assuming RRR = 50). It is based on the current-sharing model and the temperature dependence of the resistivity of plated copper as introduced in a previous study [5.26].

5.4.3 Experimental Results

Figures 5.18 and 5.19 show examples of the voltages/currents/temperatures of the thermal runaway detection and protection of monofilament and multifilament samples, respectively. The total voltage values across the entire sample (used for detection) and operating current (exponentially decreases when thermal runaway is detected) are shown in Figures 5.18(b) and 5.19(b), respectively. The experiments were conducted using the same detection and protection conditions (v_{th} = 100 mV, t_d = 100 ms, and τ = 1 s), which were reasonable for real magnets [5.26]. In the two experiments, the maximum temperatures in the monofilament and multifilament samples are approximately 250 K, as shown in Figures 5.18(d) and 5.19(d), respectively. After the experiments, the degradation of critical currents and n values was not observed for both conductors.

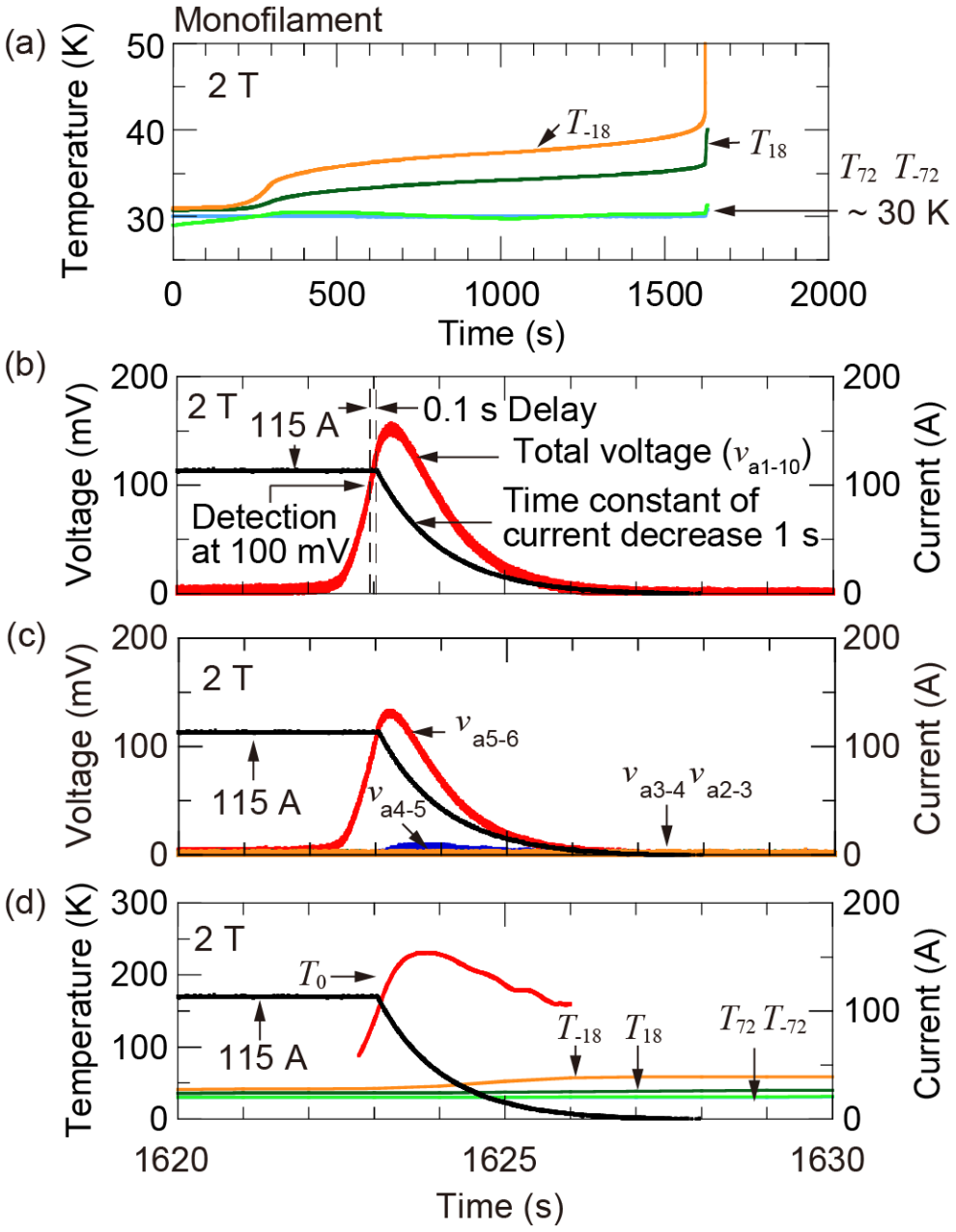

Figure 5.18 Example of voltage/current/temperature of thermal runaway detection and protection processes (monofilament sample) at 2 T (115 A): (a) Temperature when current starts thermal runaway flow; (b) Total voltage when thermal runaway is initiated; (c) Voltage on plus side when thermal runaway is initiated; (d) Temperature when thermal runaway is initiated. (v_{am-n}: voltage between taps am and an; v_{bm-n}: voltage between taps bm and bn; v_{ti}: voltage between taps ai and bi; T_x: temperature at position x) [5.9] © 2022 IEEE.

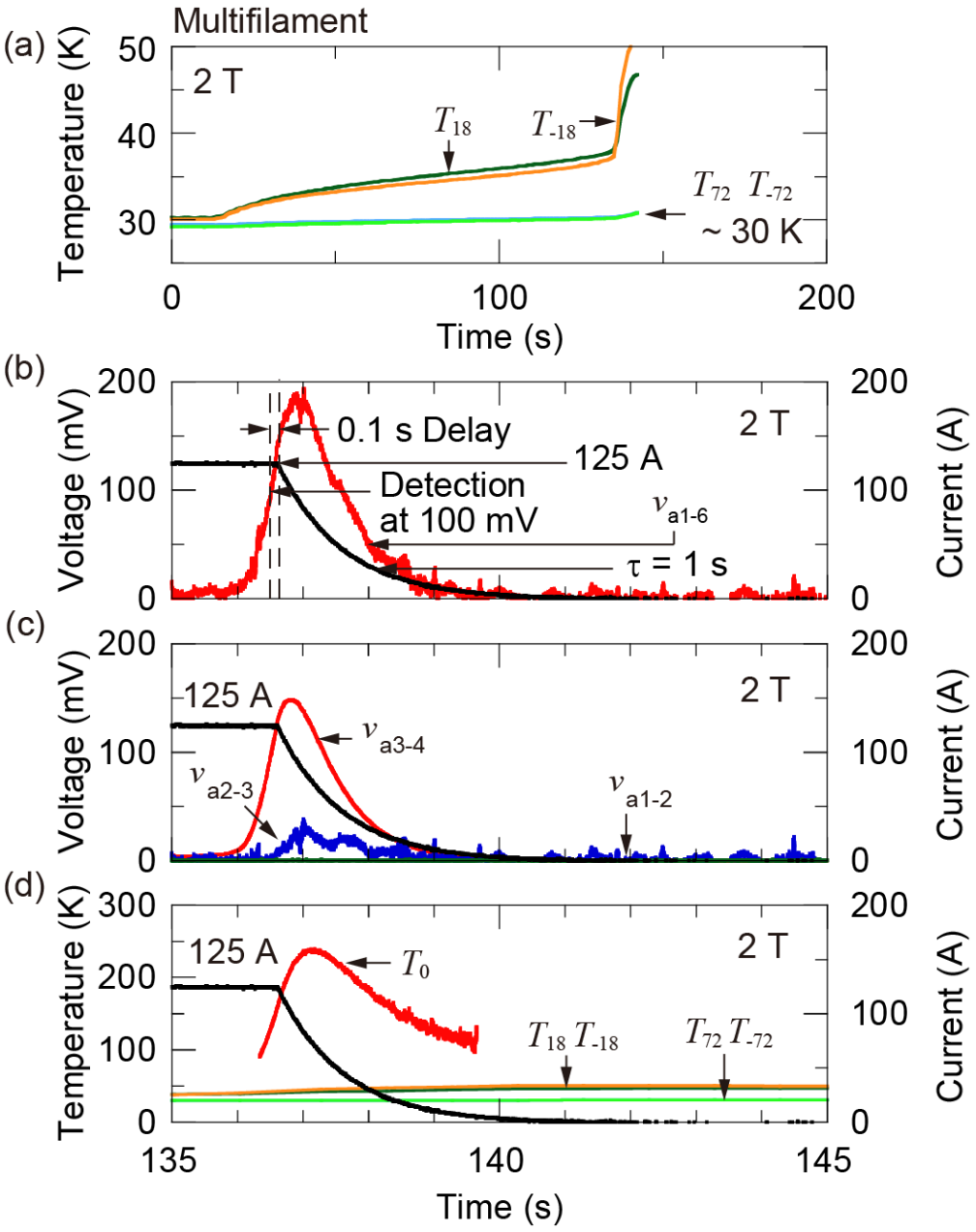

Figure 5.19 Example of voltage/current/temperature of thermal runaway detection and protection processes (multifilament sample) at 2 T (125 A): (a) Temperature when current starts thermal runaway flow; (b) Total voltage when thermal runaway is initiated; (c) Voltage on plus side when thermal runaway is initiated; (d) Temperature when thermal runaway is initiated. ($v_{am–n}$: voltage between taps am and an; $v_{bm–n}$: voltage between taps bm and bn; v_{ti}: voltage between taps ai and bi; T_x: temperature at position x) [5.9] © 2022 IEEE.

The magnetic field is varied to modify the critical current and then change the thermal runaway current. The experimental results on thermal runaway detection and protection conducted at various thermal runaway currents are summarized in Figure 5.20. The white bars in the figure represent thermal runaway after which no degradation of the critical current/n value is observed; the red bars represent thermal runaway after which the samples are degraded. In other words, the current in the white bars is under the *protectable current*, below which the applied conditions (v_{th} = 100 mV, t_d = 0.1 s, and τ = 1 s) can protect the coated conductors. These experimental results suggest that the *protectable current* of monofilament/multifilament samples against thermal runaway is approximately 150 A. The critical currents and maximum hot-spot temperatures are also shown in the figure. The details of thermal runaway experiments (holding time, critical current before and after thermal runaway, etc.) are listed in Table 5.2.

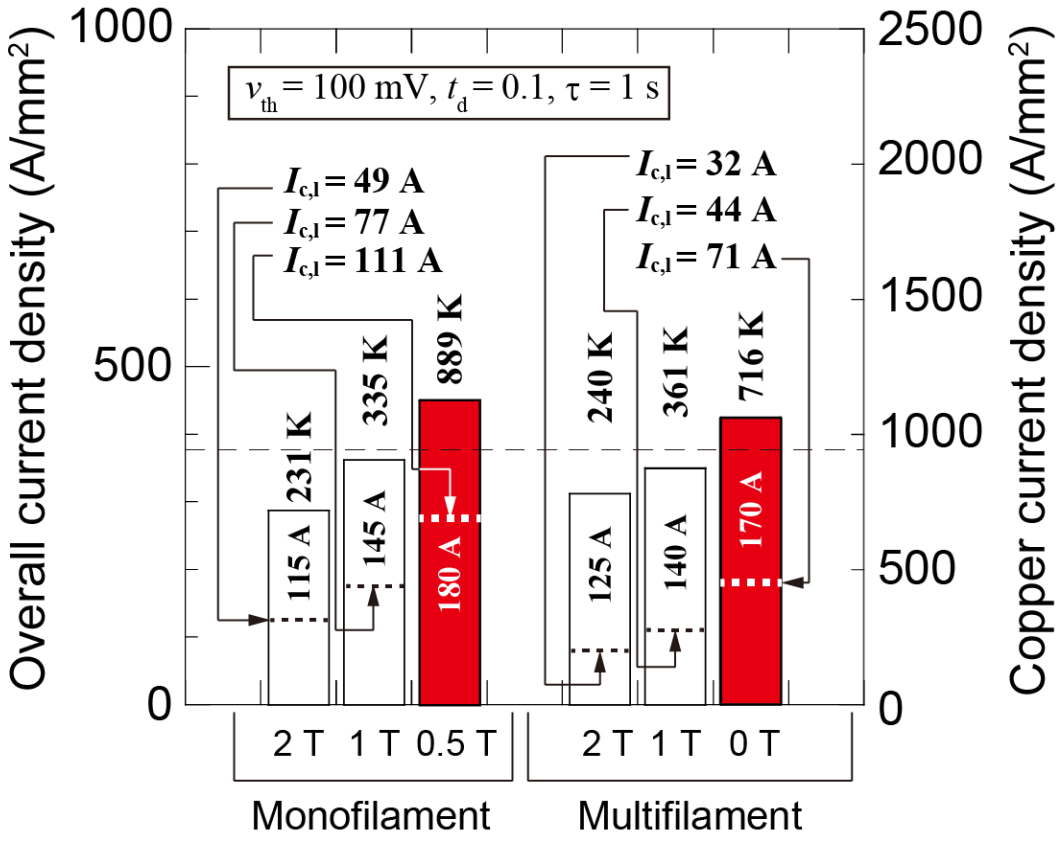

Figure 5.20 Summary of thermal runaway detection and protection experiments. White bar: degradation not observed; Red bar: samples are degraded; $I_{c,l}$: critical current at local defect measured between a5 and a6 in monofilament samples and between a3 and a4 in multifilament samples (length: 20 mm; electric field: 100 μV/m) [5.9] © 2022 IEEE.

TABLE 5.2
SUMMARY OF DETECTION OF AND PROTECTION AGAINST THERMAL RUNAWAYS INITIATED AT LOCAL BENDING DEFECT [5.9] © 2022 IEEE

Sample	I_t (T, B)	Holding time until thermal runaway	$I_{c,l}$ before and after thermal runaway	n before and after thermal runaway
Mono-filament (one sample)	115 A (30 K, 2 T)	~ 30 min	before: 49 A after: 49 A	before: 16 after: 15
	145 A (30 K, 1 T)	~ 30 min	before: 77 A after: 79 A	before: 17 after: 18
	180 A (30 K, 0.5 T)	~ 10 min	before: $I_{c,l}$ = 111 A, n = 20 after: burnt out	
Multi-filament (one sample)	125 A (30 K, 2 T)	~ 2 min	before: 32 A after: 32 A	before: 10 after: 9
	140 A (30 K, 1 T)	~ 4 min	before: 44 A after: 43 A	before: 8 after: 9
	170 A (30 K, 0 T)	~ 3 min	before: $I_{c,l}$ = 71 A, n = 5 after: linear V-I	

Detection and protection conditions: v_{th} = 100 mV, t_d = 0.1 s, τ = 1 s;
$I_{c,l}$: critical current at local defect measured between a5 and a6 in monofilament sample and between a3 and a4 in multifilament sample (length: 20 mm, electric field: 100 μV/m).

5.5 Protectable Current Against Quench and Thermal Runaway

Figure 5.21 compares the quench/thermal runaway detection and protection experimental results, including the critical currents and the maximum hot-spot temperatures at each operating current using monofilament coated conductors (SCS4050). In a previous study [5.26], the *protectable current* of a monofilament coated conductor (attached to the same sample holder used in this study) is evaluated against the quench induced by local and transient thermal disturbances (using a quench heater). The *protectable currents* of monofilament and multifilament samples against the quench induced by local and transient thermal disturbances is 160 A (the copper current density and overall current density are 1000 and 400 A/mm^2, respectively), which approximates that against thermal runaway, as shown in Figure 5.21. This suggests that the *protectable current* does not depend on the cause of the quench/thermal runaway.

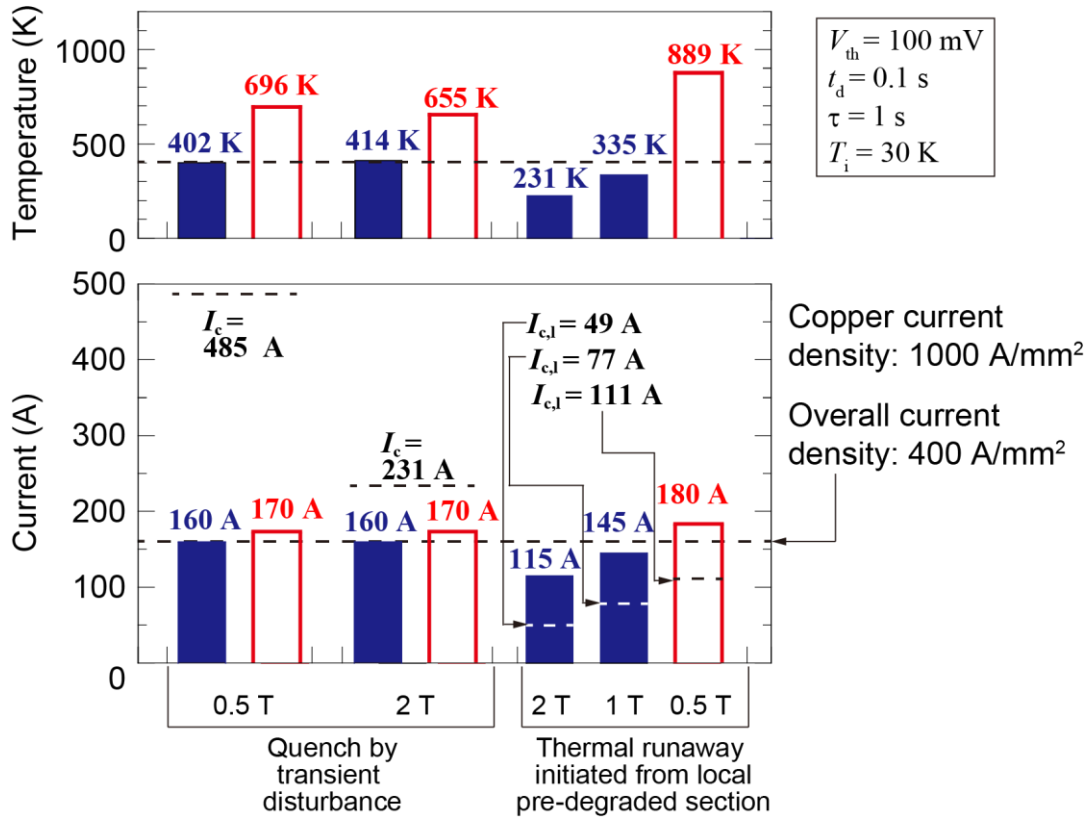

Figure 5.21 Comparison of quench/thermal runaway detection and protection experimental results using monofilament coated conductors (SCS4050). Blue bar: degradation not observed; Red bar: samples degraded; $I_{c,l}$: critical current at local defect (length: 20 mm; electric field: 100 μV/m).

5.6 Chapter Summary

The thermal runaways of copper-plated multifilament coated and monofilament coated conductors, which were conduction-cooled by a cryocooler, were experimentally investigated. In the copper-plated multifilament coated conductor, a copper layer covered the entire group of filaments, allowing current sharing among them to improve stability and protection. When an artificial local defect was created close to one edge of this multifilament conductor, the current was successfully bypassed through the copper and sound filaments on the other side. Although this bypassing current generated additional Joule loss in the copper layer, its effect on the initiation of thermal runaway was not remarkable. The thermal runaway in the multifilament coated conductor was initiated at virtually the same operating current in the monofilament coated conductor. However, thermal runaway was initiated earlier in the multifilament coated conductor. Once thermal runaway is initiated, it is important to determine whether it can be protected. When the conventional quench detection and protection scheme (detecting voltage and dumping energy by a resistor, *i.e.*, exponentially decreasing the current) was applied, the threshold currents for the successful protection (*protectable currents*) of the monofilament and multifilament coated conductors were virtually at the same level.

5.7 Appendix: Transverse Conductance among Superconductor Filaments

The transverse conductance among the superconductor filaments was also estimated. This was accomplished by comparing the experimentally determined coupling time constant of the multifilament coated conductor with that obtained from numerical analyses when the transverse conductance was varied [5.19]. The derived transverse conductance per unit length across one striation (at 77 K, g_{s1-77K}) was 2.7×10^9 S/m.

The experiments were conducted at 30 K using a five-filament (i.e., four striations) coated conductor. By considering the resistivity–temperature relationship of copper, the transverse conductance across four striations among the filaments can be given as follows:

$$g_{s4-30\,K} = \frac{1}{4} \cdot \frac{\rho_{77\,K}}{\rho_{30\,K}} \cdot g_{s1-77\,K}, \tag{5.1}$$

where ρ_{77K} (2.27×10^{-9} Ω m) and ρ_{30K} (3.80×10^{-10} Ω m) are the resistivity values of copper at 77 and 30 K, respectively [5.34]. The obtained transverse conductance across four striations among the filaments ($g_{s4-30\,K}$) was 4.03×10^9 S/m.

[References]

[5.1] L. Ren, S. Guo, G. Chen, L. Su, Y. Xu, J. Shi, and L. Chen, "Experimental research on critical current behavior of various commercial HTS tapes," *IEEE Trans. Appl. Supercond.*, vol. 30, no. 4, Jun. 2020, Art. no. 6601006.

[5.2] F. Gömöry, J. Šouc, M. Adámek, A. Ghabeli, M. Solovyov, and M. Vojenčiak, "Impact of critical current fluctuations on the performance of a coated conductor tape," *Supercond. Sci. Technol.*, vol. 32, Oct. 2019, Art. no. 124001.

[5.3] H. Ha, G. Kim, H. Noh, J. Lee, S. Moon, and S. Oh, "Fabrication of 1 m long multi layered superconducting coated conductor with high engineering critical current density," *Supercond. Sci. Technol.*, vol. 33, Feb. 2020, Art no. 044007.

[5.4] C. Pop, B. Villarejo, F. Pino, B. mundet, S. Ricart, M. de Palau, T. Puig, and X. Obradors, "Growth of all-chemical high critical current $YBa_2Cu_3O_{7-\delta}$ thick films and coated conductors," *Supercond. Sci. Technol.*, vol. 32, Nov. 2018, Art. no. 015004.

[5.5] U. Bong, J. Kim, J. Bang, J. Park, K.J. Han, and S. Hahn, "'Defect-irrelevant-winding' no-insulation (RE)$Ba_2Cu_3O_{7-x}$ pancake coil in conduction-cooling operation," *Supercond. Sci. Technol.*, vol. 34, Jun. 2021, Art. no. 085003.

[5.6] Y. Zhu, W. Chen, H. Zhang, L. Liu, X. Pan, X. Yang, and Y. Zhao, "Study of the inhomogeneity of critical current under in-situ tensile stress for YBCO tape," *Supercond. Sci. Technol.*, vol. 31, Feb. 2018, Art. no. 035007.

[5.7] Z. Yue, Z. Sun and Z. Liu, "Design and Magnetic Field Simulation of 3.0T MRI Superconducting Magnet," *IEEE Trans. Appl. Supercond.*, vol. 29, no. 2, March 2019, Art no. 4901106.

[5.8] E. Seiler, F. Gömöry, R. Ries, and M. Vojenčiak, "Analysis of critical current anisotropy in commercial coated conductors in terms of the maximum entropy approach," *Supercond. Sci. Technol.*, vol. 32, Jul. 2019, Art no. 095004.

[5.9] X. Luo, Y. Zhao, Y. Sogabe, H. Sakamoto, S. Yamano, and N. Amemiya, "Thermal runaway of conduction-cooled monofilament and multifilament coated conductors," *IEEE Trans. Appl. Supercond*., 2022. DOI: 10.1109/TASC.2022.3141970

[5.9] N. Amemiya, N. Tominaga, R. Toyomoto, T. Nishimoto, Y. Sogabe, S. Yamano, and H. Sakamoto, "Coupling time constants of striated and copper-plated coated conductors and the potential of striation to reduce shieldingcurrent-induced fields in pancake coils," *Supercond. Sci. Technol.*, vol. 31, Jan. 2018, Art no. 025007.

[5.11] N. Amemiya, Y. Sogabe, S. Yamano, and H. Sakamoto, "Shielding current in a copper-plated multifilament coated conductor wound into a single pancake coil and exposed to a normal magnetic field," *Supercond. Sci. Technol.*, vol. 32, Oct. 2019, Art no. 115008.

[5.12] F. Grilli, and A. Kario, "How filaments can reduce AC losses in HTS coated conductors: a review," *Supercond. Sci. Technol.*, vol. 29, Jul. 2016, Art no. 083002.

[5.13] E. Pardo, M. Kapolka, J. Kováč, J. Šouc, F. Grilli, and A. Piqué, "Three-dimensional modeling and measurement of coupling AC loss in soldered tapes and striated coated conductors," *IEEE Trans. Appl. Supercond.*, vol. 26, no. 3, Apr. 2016, Art. no. 4700607.

[5.14] F. Gömöry, and J. Šouc, "Stability of DC transport in HTS conductor with local critical current reduction," *Supercond. Sci. Technol.*, vol. 34, Jan. 2021, Art no. 025005.

[5.15] H. Mochida, Y. Suetomi, T. Takao, H. Maeda and Y. Yanagisawa, "Continuous Heating Criteria to Avoid Thermal Runaway of Insulated HTS Coils in High Fields," *IEEE Trans. Appl. Supercond.*, vol. 29, no. 5, Aug. 2019, Art no. 4301306.

[5.16] L. Ren, G. Chen, Y. Xu, D. Pu, J. Xu, S. Yan, J. Shi, and L. Chen, "Experimental analysis of quench characteristic in HTS tapes and coils," *IEEE Trans. Appl. Supercond.*, vol. 29, no. 5, Aug. 2019, Art no. 4700606.

[5.17] H. Miyazaki, S. Iwai, T. Tosaka, K. Tasaki, S. Hanai, M. Urata, S. Ioka, and Y. Ishii, "Thermal stability of conduction-cooled YBCO pancake coil," *IEEE Trans. Appl. Supercond.*, vol. 21, no. 3, pp. 2453–2457, Jun. 2011.

[5.18] Y. Yanagisawa, T. Fukuda, K. Sato, H. Nakagome, T. Takao, H. Kamibayashi, M. Takahashi, and H. Maeda, "Use of a thermal grid to increase thermal runaway current for REBCO pancake coils operated at 77 K," *IEEE Trans. Appl. Supercond.*, vol. 23, no. 3, Jun. 2013, Art. no. 4603505.

[5.19] Y. Yanagisawa, E. Okuyama, H. Nakagome, T. Takematsu, T. Takao, M. Hamada, S. Matsumoto, T. Kiyoshi, A. Takizawa, M. Takahashi, and H. Maeda, "The mechanism of thermal runaway due to continuous local disturbances in the YBCO-coated conductor coil winding," *Supercond. Sci. Technol.*, vol. 25, Jun. 2012, Art no. 075014

[5.20] S. Takayama, K. Koyanagi, T. Tosaka, K. Tasaki, T. Kurusu, Y. Ishii, N. Amemiya, K. Suzuki, T. Ogitsu, Y. Iwata, and K. Noda, "Thermal Stability of Conduction-Cooled HTS Magnets for Rotating Gantry," *IEEE Trans. Appl. Supercond*,. vol. 26, no. 4, Jun. 2016, Art no. 4402404.

[5.21] A. Badel, B. Rozier, K. Takahashi and S. Awaji, "Simulation of Local Dissipation Phenomena in the REBCO Insert of the 25-T CSM Magnet: Understanding and Preventing Destructive Thermal Runaway," *IEEE Trans. Appl. Supercond.*, vol. 29, no. 5, Aug. 2019, Art no. 4600605.

[5.22] J. Ruuskanen, A. Stenvall, V. Lahtinen, J. van Nugteren, G. Kirby and J. Murtomäki, "How to Computationally Determine the Maximum Stable Operation Current of an HTS Magnet," *IEEE Trans. Appl. Supercond.*, vol. 29, no. 5, Aug. 2019, Art no. 4701204.

[5.23] A. Badel, B. Rozier, B. Ramdane, G. Meunier, and P. Tixador, "Modeling of 'quench' or the occurrence and propagation of dissipative zones in REBCO high temperature superconducting coils," *Supercond. Sci. Technol.*, vol. 32, Jul. 2019, Art. no. 094001.

[5.24] M. A. Green, "Quench protection solutions for magnets fabricated with insulated HTS tape conductors," *IEEE Trans. Appl. Supercond.*, vol. 28, no. 3, April 2018, Art no. 4700705.

[5.25] R. Matsuo, N. Matsuda, Y. Fuchida, A. Kojima, A. Nomoto, T. Takao, K. Nakamura, and O. Tsukamoto., "Study on hot-spot temperature limits of epoxy-impregnated coil wound with Bi/Ag sheathed wire to be safe from damage caused by quenches," *IEEE Trans. Appl. Supercond.*, vol. 28, no. 4, Jun. 2018, Art no. 4703605.

[5.26] X. Luo, S. Inoue, N. Amemiya, "Experimental study on quench detection and protection conditions of copper-stabilized coated conductors using short samples," *IEEE Trans. Appl. Supercond.*, vol. 29, no. 8, Dec. 2019, Art. no. 4703511.

[5.27] H. Toriyama, A. Nomoto, T. Ichikawa, T. Takao, K. Nakamura, O. Tsukamoto, and M. Furuse, "Quench protection system for an HTS coil that uses Cu tape co-wound with an HTS tape," *Supercond. Sci. Technol.*, vol. 32, Oct. 2019, Art. no. 115016.

[5.28] M. N. Wilson, “Protection by an external resistor,” in *Superconducting Magnets*, Oxford, U.K.: Clarendon, 1983, pp. 219–221.

[5.29] T. Minagawa, Y. Fujimoto, and O. Tsukamoto, “Study on protection of HTS coil against quench due to temperature rise of long part of HTS wires,” *IEEE Trans. Appl. Supercond.*, vol. 23, no. 3, Jun. 2013, Art no. 4702004.

[5.30] G. Celentano *et al*., “Quench behavior of a conduction cooled $YBa_2Cu_3O_{7-x}$ tape pancake coil,” *IEEE Trans. Appl. Supercond.*, vol. 23, no. 3, Jun. 2013, Art no. 4600704.

[5.31] A. Ishiyama, H. Ueda, Y. Aoki, K. Shikimachi, N. Hirano, and S. Nagaya, “Quench behavior and protection in cryocooler-cooled YBCO pancake coil for SMES,” *IEEE Trans. Appl. Supercond.*, vol. 21, no. 3, pp. 2398–2401, Jun. 2011.

[5.32] H. Ueda, A. Ishiyama, K. Muromachi, T. Suzuki, K. Shikimachi, N. Hirano, and S. Nagaya, “Quench detection and protection of cryocooler-cooled YBCO pancake coil for SMES,” *IEEE Trans. Appl. Supercond.*, vol. 22, no. 3, Jun. 2012, Art no. 4702804.

[5.33] Y. Iwasa, H. Lee, J. R. Fang, and B. Haid, “Quench and recovery of YBCO tape experimental and simulation results,” *IEEE Trans. Appl. Supercond.*, vol. 13, no. 2, pp. 1772–1775, Jun. 2003.

[5.34] G. Manfreda, “Review of ROXIE's material properties database for quench simulation” CERN Internal Note 2011-24, EDMS Nr: 1178007.

Chapter 6 Relevance of Short-Sample Experiments to Real Coils

6.1 Chapter Background and Objective

In **Chapter 3**, the short-sample experiment is introduced. Short coated conductor pieces instead expensive superconducting coils are burned to study the detection of and protection against quench/thermal runaway. However, considering that the condition of a short sample differs from that of a real coil, the experiments could not simulate all features of the coil. Accordingly, the relevance of the short-sample experiments to real coils is discussed herein.

The objective of this chapter is to study the differences between short samples and conductors in a real magnet in terms of the following:

1) transverse thermal diffusion and longitudinal thermal conduction;
2) conductor length;
3) temperature rise and degradation.

6.2 Transverse Thermal Diffusion and Longitudinal Thermal Conduction in Short-Sample Experiments

This section discusses the influence of transverse thermal diffusion and longitudinal thermal conduction through 1D quench simulations based on the experimental results (using SCS4050 when B = 2 T, T_i = 30 K, I_{op} = 150 A, V_{th} = 100 mV, τ = 1 s, and t_d = 100 ms, as shown in Figure 4.7).

The 1D heat conduction equation of a coated conductor under adiabatic condition (*i.e.*, no transverse thermal diffusion around it) is given by

$$\gamma C_c \frac{\partial T}{\partial t} = \frac{\partial}{\partial x}\left(k_c \frac{\partial T}{\partial x}\right) + g + \frac{p_{ds}}{L_{ds} w t_c}, \tag{6.1}$$

where T denotes temperature, and x is the coordinate along the coated conductor. The other parameters in the equation are summarized and explained in Table 6.1; the thicknesses of components of the coated conductor are listed in Table 6.2 as case 1. The thermal disturbance represented by the parameters listed in Table 6.3 initiated quench. Voltage is calculated based on the temperature dependency of the resistance of copper layer, as follows: $V(x, t) = R(x, T) \times I(t)$. When the total voltage exceeds V_{th}, and after a delay time (t_d), the current, $I(t)$, is decreased with the time constant, τ.

As shown in Figure 6.1(a), the calculated and measured voltage values of $v_{5–6}$ and current are compared. An extremely small measured value of $v_{5–6}$ suggests that

the transverse thermal diffusion to the epoxy resin, polyimide tape, and GFRP block (Figure 3.2) substantially influences the quench process. In order to consider such transverse thermal diffusion in the 1D quench simulation, we simply attached some amount of GFRP to add the heat capacity to that of the coated conductor and used the following equation instead of (6.1):

$$\left(\gamma C_{\mathrm{c}} + \gamma C_{\mathrm{g}} \frac{t_{\mathrm{g}}}{t_{\mathrm{c}}}\right) \frac{\partial T}{\partial t} = \frac{\partial}{\partial x}\left(k_{\mathrm{c}} \frac{\partial T}{\partial x}\right) + g + \frac{p_{\mathrm{ds}}}{L_{\mathrm{ds}} w t_c}. \tag{6.2}$$

TABLE 6.1
Parameters of ID Heat Conduction Equation [6.1] © 2019 IEEE

t_{c}	thickness of coated conductor
t_{s}	thickness of superconductor
t_{H}	thickness of Hastelloy substrate
t_{Ag}	thickness of silver
t_{Cu}	thickness of copper
γC_{c}	specific heat of coated conductor
γC_{H}	specific heat of Hastelloy substrate
γC_{Ag}	specific heat of silver
γC_{Cu}	specific heat of copper
k_{c}	thermal conductivity of coated conductor
k_{H}	thermal conductivity of Hastelloy substrate
k_{Ag}	thermal conductivity of silver
k_{Cu}	thermal conductivity of copper
g	Joule heat generation
p_{ds}	power of thermal disturbance
L_{ds}	length of thermal disturbance
w	width of thermal disturbance

$t_{\mathrm{c}} = t_{\mathrm{s}} + t_{\mathrm{H}} + t_{\mathrm{Ag}} + t_{\mathrm{Cu}}$
$\gamma C_{\mathrm{c}} = [\gamma C_{\mathrm{H}}(t_{\mathrm{s}} + t_{\mathrm{H}}) + \gamma C_{\mathrm{Ag}} t_{\mathrm{Ag}} + \gamma C_{\mathrm{Cu}} t_{\mathrm{Cu}}] / t_{\mathrm{c}}$
$k_{\mathrm{c}} = [k_{\mathrm{H}}(t_{\mathrm{s}} + t_{\mathrm{H}}) + k_{\mathrm{Ag}} t_{\mathrm{Ag}} + k_{\mathrm{Cu}} t_{\mathrm{Cu}}] / t_{\mathrm{c}}$

TABLE 6.2
THICKNESS OF COMPONENTS IN QUENCH SIMULATION [6.1] © 2019 IEEE

Thickness	Case 1	Case 2	Case 3
t_c (mm)	0.0948	0.0948	0.1448
t_s (mm)	0.001	0.001	0.001
t_H (mm)	0.05	0.05	0.1
t_{Ag} (mm)	0.0038	0.0038	0.0038
t_{Cu} (mm)	0.04	0.04	0.04
t_G (mm)	0	0.285	0.16

TABLE 6.3
PARAMETERS OF THERMAL DISTURBANCE [6.1] © 2019 IEEE

p_{ds}	2.5 W
L_{ds}	8 mm
w	4 mm

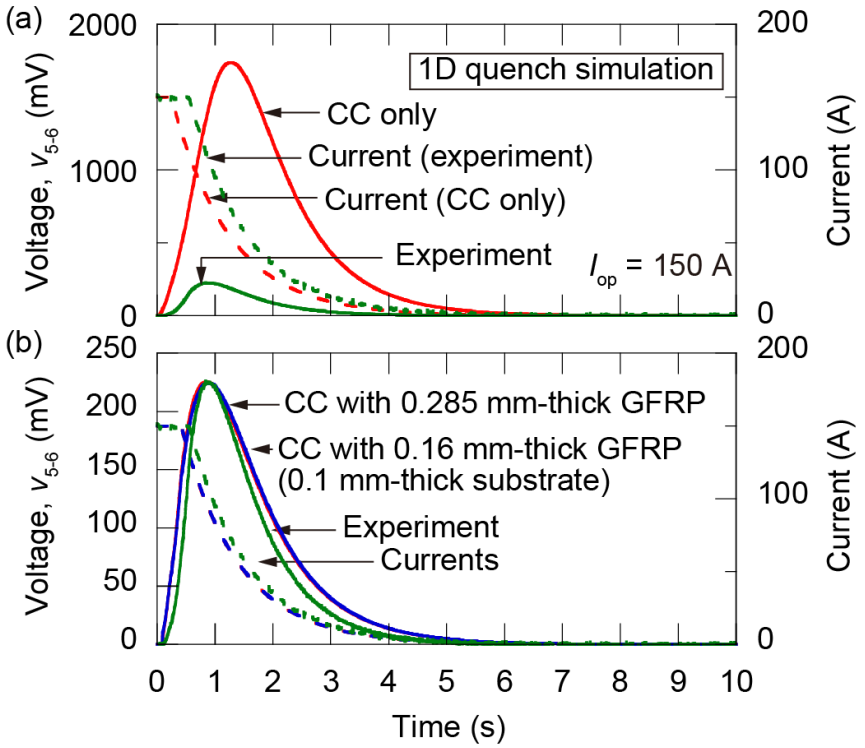

Figure 6.1. Voltage $v_{5–6}$ and currents in 1D quench simulation and experiment (T_i = 30 K, B = 2 T, I_{op} = 150 A, v_{th} = 100 mV, t_d = 100 ms, and τ = 1 s; CC: coated conductor): (a) $v_{5–6}$ and currents in 1D quench simulation (CC only) and experiment; (b) $v_{5–6}$ and currents in 1D quench simulations (with 0.285-mm-thick GFRP, with 0.16-mm-thick GFRP, and 0.1-mm-thick Hastelloy substrate) and experiment [6.1] © 2019 IEEE.

The additional parameters are listed and explained in Table 6.2. The thickness (t_G) of the attached GFRP was varied to ensure consistency between the calculated and measured voltage values of $v_{5–6}$. Similar to the experiment, the Hastelloy substrate thickness (t_H) was assumed to be 0.05 mm (case 2 in Table 6.2) or 0.1 mm (case 3 in Table 6.2). The calculated and measured values of $v_{5–6}$ agree when t_G = 0.285 mm in case 2 and when t_G = 0.16 mm in case 3, as shown in Figure 6.1(b). The use of a 0.16-mm-thick GFRP between turns may not be possible. Alternatively, a 0.025-m-thick polyimide tape wrapped around a coated conductor and 0.03-mm-thick epoxy resin between turns may be possible; this can be equivalent to a 0.16-mm-thick GFRP: 0.025 mm × 4 + 0.03 mm × 2.

To determine the influence of longitudinal thermal conduction, zero-dimensional (0D) quench simulations for case 3 (Table 6.2) are implemented using the following heat balance equation (the calculation is based on the integration approach introduced in equations (2.3)–(2.5)):

$$\left(\gamma C_c + \gamma C_g \frac{t_g}{t_c}\right)\frac{\partial T}{\partial t} = g + \frac{p_{\mathrm{ds}}}{L_{\mathrm{ds}} w t_c}. \tag{6.3}$$

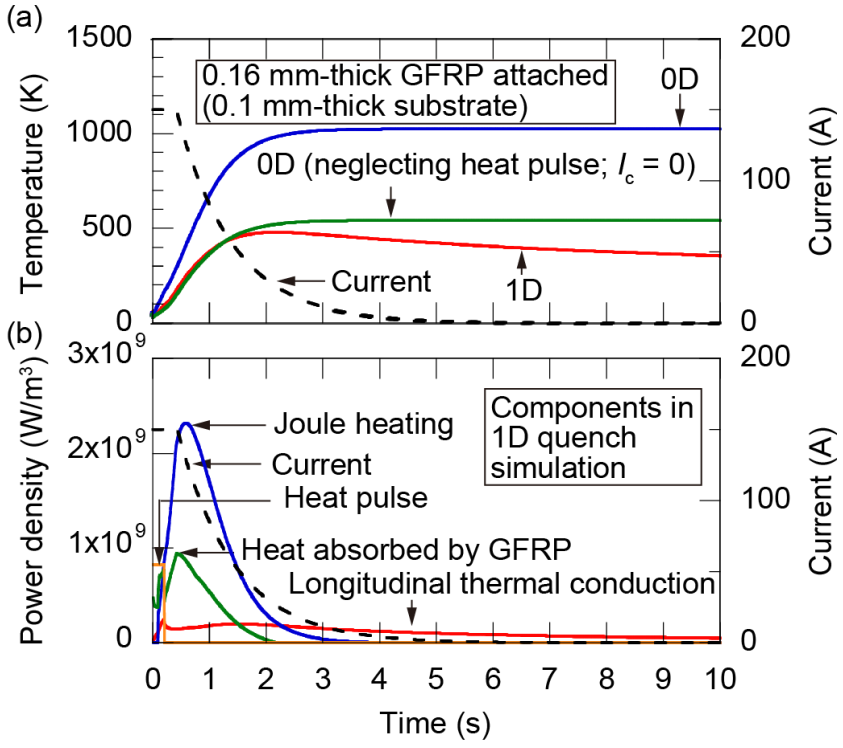

Figure 6.2. Maximum temperature and power density of components in quench simulation with 0.16-mm-thick GFRP (0.1-mm-thick substrate): (a) maximum temperature in 1D and 0D simulations (using current data of 1D simulation); (b) power density of components in 1D quench simulation [6.1] © 2019 IEEE.

As shown in Figure 6.2(a), the hot-spot temperatures given by the 1D and 0D quench simulations are plotted against time. The hot-spot temperature in the former is considerably lower than that in the latter, although the longitudinal thermal conduction (the first term on the right side of (2)) is not remarkable when compared with the other terms, as shown in Figure 6.2(b). However, by examining the initial phase of quench shown in Figure 6.3, the contribution of the longitudinal thermal conduction is more remarkable than that shown in Figure 6.2(b). The longitudinal thermal conduction may suppress the temperature rise due to the local thermal disturbance; then, it may suppress Joule heat generation. This effect may finally suppress the hot-spot temperature in the later phase.

The hot-spot temperature calculated using equation (6.3) is also plotted, as shown in Figure 6.2(a). However, the local thermal disturbance (the second term on the right side of the equation) and critical current (when calculating g (the first term on the right side of the equation)) are neglected (in 0D, heat pulse is neglected; $I_c = 0$). The foregoing is similar to equation (2.5), presented in **Section 2.1.1**.

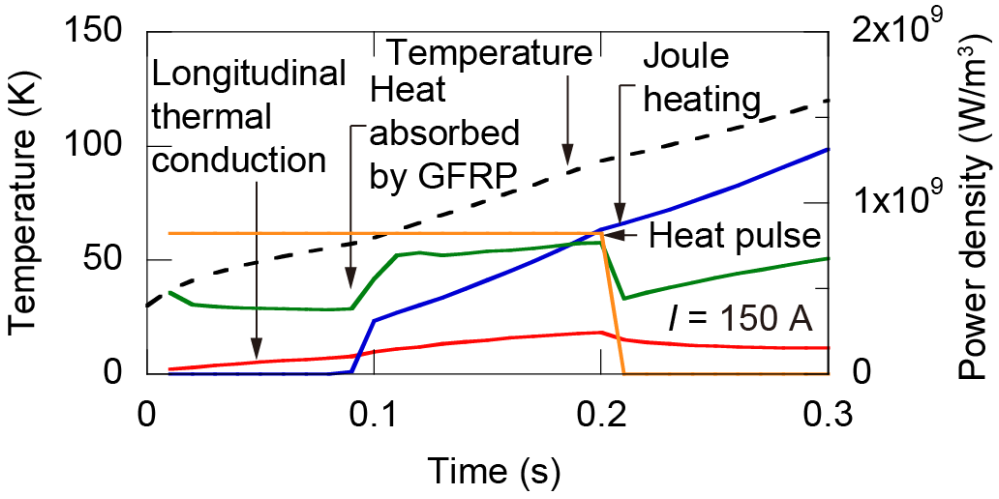

Figure 6.3. Enlarged view of maximum temperature and power density of components in 1D quench simulation with 0.16-mm-thick GFRP (0.1-mm-thick substrate) [6.1] © 2019 IEEE.

6.3 Conductor Length in Short-Sample Experiments and Real Magnets

The short samples and coated conductors in coils differ in lengths. The short length (effective length: 180 mm) of the samples may have affected the results because the copper current terminals with large heat capacities may have served as a heat sink with constant temperature. The temperatures measured before quench using

CX1, CX3, CX4, and CX2 are shown in Figure 6.4. By extrapolating these temperature values, the estimated temperature at the copper terminal is approximately 29 K. Furthermore, the temperature increased by approximately 5 K at TC1 and TC2 during quench. From these values and the separation between TC1, TC2, and copper current terminals (15 mm), the thermal conduction to the copper terminals using the thermal conductivity of the sample at 30 K (1920 W/m·K) was estimated. The estimated thermal conduction to both current terminals is 0.52 W, which is considerably smaller than the Joule heat generation (approximately 10 W) in the sample during quench. This result suggests that cooling using the copper current terminals does not significantly affect temperature increase.

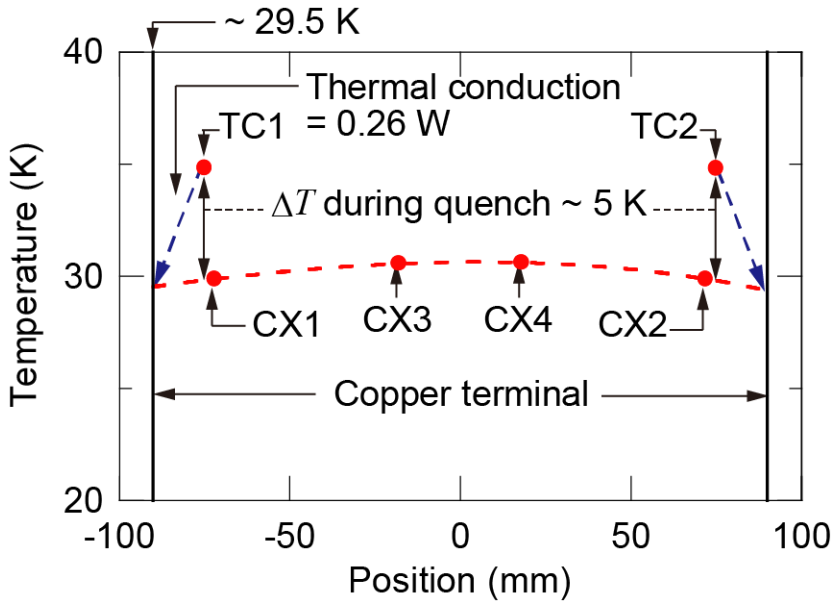

Figure 6.4 Temperature distribution before quench and calculated thermal conduction at ends of short sample during quench based on temperatures measured by TC1 and TC2 [6.1] © 2019 IEEE.

To study the effect of short length, the temperatures of samples with different lengths are compared using the 1D simulation introduced in **Section 6.2.1**. Figures 6.5 and 6.6 show the hot-spot temperature (temperature at the center of the conductor) and temperature distribution in coated conductors of various lengths, respectively. In the 1D simulation, the temperatures at the ends of the coated conductor are set to be constant (30 K, which simulates the effect of copper current terminals). The parameters of coated conductors are set as those of case 3 listed in Table 6.3. The parameters of thermal disturbances are listed in Table 6.4. The hot-spot temperatures when the operating current is 150 A are shown in Figure 6.5. When the conductor is extremely short (*e.g.*, 50 mm), its length affects the hot-spot

temperature; when the conductor is sufficiently long (> 100 mm), the length does not affect the hot-spot temperature. In other words, the hot-spot temperature is independent of length when the conductor is longer than 100 mm. Figure 6.6 shows the temperature distribution along the conductors of various lengths at 5 s after the start of thermal disturbance (when t = 5 in Figure 6.5). When the conductor is sufficiently long (> 100 mm), its length does not affect the temperature distribution near the center of the conductor. The experimental and numerical calculation results shown in Figures 6.4 and 6.5, respectively. Figure 6.6, suggests that the conductor length in the short-sample experiments (180 mm) is sufficiently long to be used in the study of hot-spot temperature during the protection process of conductors in real coils.

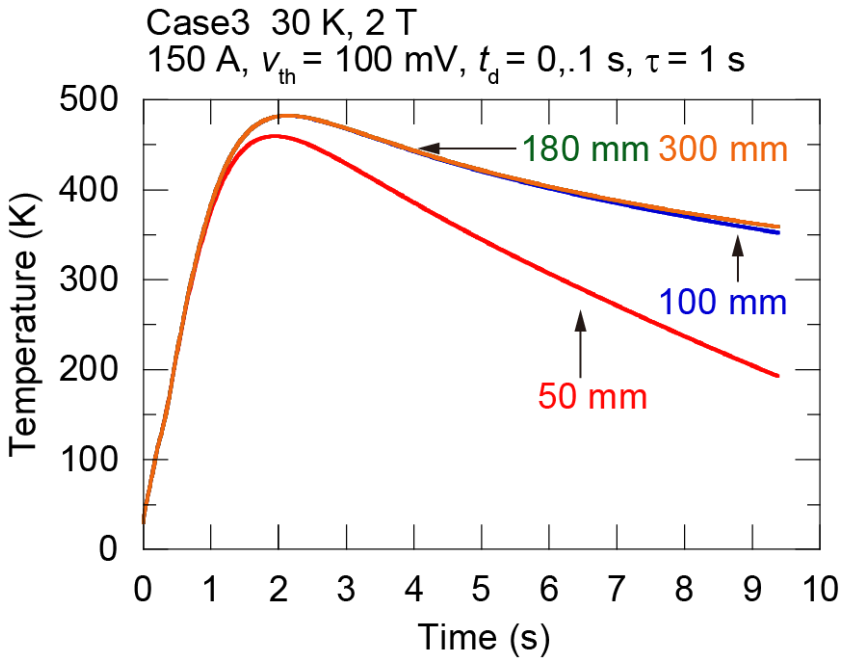

Figure 6.5 Temperatures at center of coated conductors of various lengths (parameters of conductor are those of case 3 (Table 6.2); thermal disturbance values are as listed in Table 6.3; detection voltage, v_{th}: 100 mV; delay time, t_d: 0.1 s; time constant of current decrease, τ: 1 s).

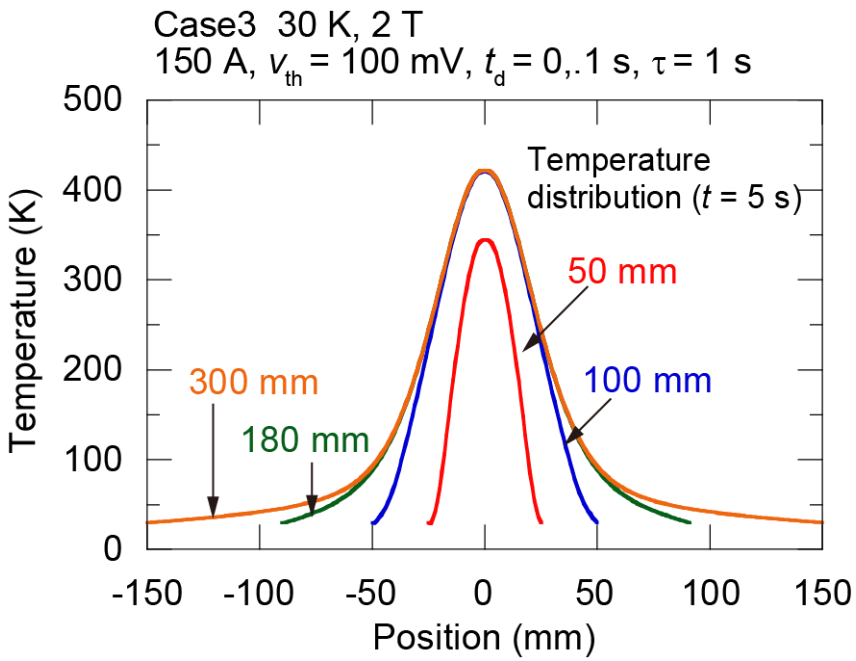

Figure 6.6 Temperature distribution along coated conductors of various lengths (5 s after start of thermal disturbance; parameters of conductor are as those of case 3 (Table 6.2); thermal disturbance values are as listed in Table 6.3; detection voltage, v_{th}: 100 mV; delay time, t_d: 0.1 s; time constant of current decrease, τ: 1 s).

6.4 Relevance of Temperature Rise to Degradation

High temperatures during quench frequently degrade superconductor coils; they can thermally or mechanically damage the coated conductor. Mechanical degradation is more severe in coils wound with coated conductors. For REBCO coated conductor, the axial strain effect [6.2], [6.3] exists but may be secondary. The threat is the peeling stress in the multilayer structure due to the mismatch of thermal expansion among different materials; this may be one reason for delamination [6.4]. In this study, straight samples were attached to the GFRP block using polyimide tape and epoxy resin without bending. Bending may lead to a higher maximum allowable temperature than that of coated conductors in real coils. Although a coil might be degraded at lower temperatures, 300 K is used as a criterion because some previous studies have reported that the degradation risk is high at this temperature [6.5], [6.6].

6.5 Chapter Summary

The calculated results of 1D simulation suggest that the transverse thermal conduction in short-sample experiments is equivalent to that in conductors in a coil

in which 0.025-m-thick polyimide tape is wrapped around the coated conductor with 0.03-mm-thick epoxy resin between turns. For example, consider the experimental results discussed in **Chapter 4**. That chapter presents a magnet wound with a 20-μm copper-plated coated conductor with a 100-μm-thick Hastelloy substrate. It is insulated using half-wrapped 25-μm-thick polyimide and surrounded by 30-μm-thick epoxy resin (with inductance and operating current (tape current density) of 8 H and 125 A (312.5 A/mm^2), respectively). This magnet can be protected if its quench can be detected at 100 mV, and its energy is dumped to an 8-Ω resistor for which the time constant of the current decay is 1 s.

A summary of the relevance of short-sample experiments to real coils is as follows.

1) The transverse thermal diffusion influences the quench process of short-sample experiments; however, but it may be at a possible level in real coils.
2) Longitudinal thermal conduction may suppress the temperature rise (caused by heat pulse) and then Joule heat generation. This effect may finally suppress the hot-spot temperature in a later phase.
3) The short sample length does not affect the temperature during quench.
4) In real coils, the allowable temperature may be lower than that in short-sample experiments.

[References]

[6.1] X. Luo, S. Inoue, and N. Amemiya, "Experimental study on quench detection and protection conditions of copper-stabilized coated conductors using short samples," *IEEE Trans. Appl. Supercond*., vol. 29, no. 8, Dec. 2019, Art. no. 4703511.

[6.2] L. Ye, P. Li, J. Jaroszynski, J. Schwartz, and T. M. Shen, "Strain control of composite superconductors to prevent degradation of superconducting magnets due to a quench: I. Ag/$Bi_2Sr_2CaCu_2O_x$ multifilament round wires," *Supercond. Sci. Technol.*, Feb 2017, Art no. 025005.

[6.3] T. Shen, L. Ye, and H. Higley, "Strain control of composite superconductors to prevent degradation of superconducting magnets due to a quench: II. High-strength, laminated Ag-sheathed Bi-2223 tapes," *Supercond. Sci. Technol.*, vol. 31, no. 1, Jan 2018, Art no. 015012.

[6.4] T. Shen, X. Wang and S. Yin, "Strain control of HTS superconductors to prevent degradation of superconducting magnets during a quench," presented at *The 31st International Symposium on Superconductivity*, Tsukuba, Japan, Dec. 12-14, 2018.

[6.5] Y. Yanagisawa *et al*., "The mechanism of thermal runaway due to

continuous local disturbances in the YBCO-coated conductor coil winding," *Supercond. Sci. Technol.*, vol. 25, no. 7, Jul. 2012, Art no. 075014.

[6.6] Y. Iwasa, "Temperature-induced strains," in *Case Studies in Superconducting Magnets* 2nd ed. New York, NY, USA: Springer-Verlag, 2009, pp. 470–471.

Chapter 7 Factors Not Affecting Protection

7.1 Chapter Background and Objective

As discussed in **Section 2.3**, the rising temperature after quench/thermal runaway fundamentally induces degradation. Because the current density in the conductor of a superconducting magnet is extremely large, Joule heating is considered as dominating the hot-spot temperature of a conductor during the protection process. In other words, the factors (such as the operating current (**Chapters 4** and **5)** and copper thickness (**Chapter 5**)) affecting the extent of Joule heating considerably influence the quench/thermal runaway protection. In contrast, factors, such as the power of thermal disturbance inducing quench that are not supposed to affect Joule heating and initial temperature are also not expected to affect protection. The objective of this chapter is to present the experimental confirmation that the following factors do not affect the maximum hot-spot temperature in the conventional quench/thermal runaway detection and protection processes:

1) thermal disturbance power that induces quench;
2) initial temperature (*i.e.*, operating temperature) before quench;
3) critical current of conductor/magnetic field.

7.2 Power of Thermal Disturbance Inducing Quench

Certain values of the heater power in the short-sample experiments are of concern because the real magnet may suffer thermal disturbance to various extents. To determine whether the thermal disturbance power can affect quench detection and protection, experiments at varying heater power values are conducted; then, the hot-spot temperatures are compared.

Figure 7.1 shows the waveforms of hot-spot temperature and current of an SCS4050 sample when the heater power is varied. The experiments were performed at 100 A, with the following quench detection and protection conditions: detection voltage = 100 mV, delay before current decrease = 0.1 s, and time constant of current decrease = 1 s. The hot-spot temperatures were different at the onset of quench, which may be affected by heater power. However, the maximum hot-spot temperatures, which may be governed by Joule heating, in these experiments are virtually the same.

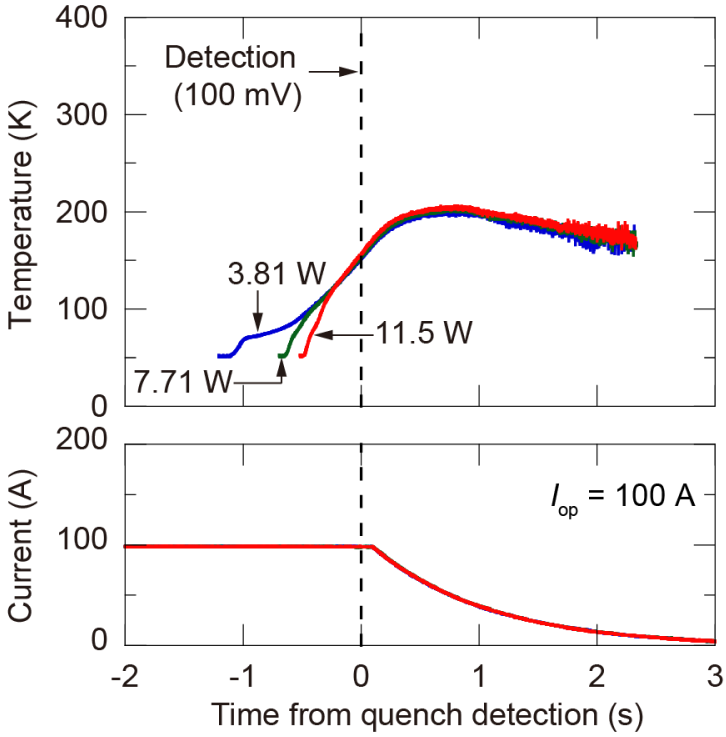

Figure 7.1 Hot-spot temperature and current waveforms during quench detection and protection processes when heater power is varied (B = 2 T, T_i = 30 K, v_{th} = 100 mV, t_d = 100 ms, and τ = 1 s) [7.1] © 2019 IEEE.

7.3 Initial Temperature Before Quench/Thermal Runaway

In the short-sample experiments, the initial temperature (the temperature before quench/thermal runaway) was maintained at certain values. However, in real conduction-cooled coils, the temperature of conductors depends on heat transfer. Short-sample experiments were performed at various initial temperatures using the same sample to determine whether different operating temperatures could affect quench detection and protection.

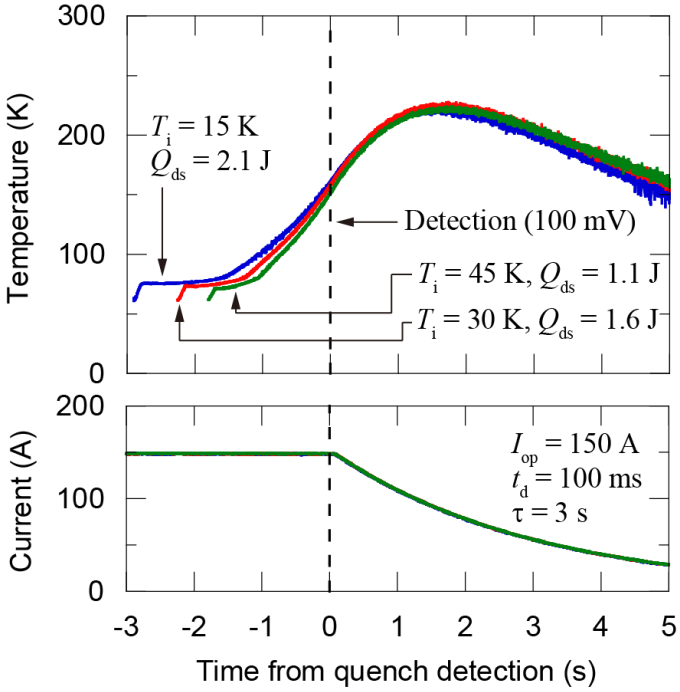

Figure 7.2 Hot-spot temperature and current at various initial temperatures (FYSC-SCH04(40), I_{op} = 150 A, v_{th} = 100 mV, t_d = 100 ms, and τ = 3 s) [7.2] © 2020 IEEE.

Figure 7.2 displays the waveforms of hot-spot temperature and the current of FYSC-SCH04(40) when the initial temperature is varied. The experiments were performed at 150 A with the same time constant of current decrease (3 s). No significant difference is observed among the hot-spot temperatures after quench detection, suggesting that the initial temperature only has a slight impact on quench detection and protection.

In Figure 7.2, the energy values of thermal disturbance causing quench are 2.1 J at 15 K, 1.6 J at 30 K, and 1.1 J at 45 K. By ignoring thermal conduction, the enthalpy margin can be calculated at various temperatures using the following equation:

$$H(T_0) = \int_{T_0}^{T_i} \gamma C(T) \mathrm{d}T, \tag{6.4}$$

Where T_i is the temperature at which the electric field reaches 100 μV/m (62 K in this case), and $\gamma C(T)$ is the volumetric specific heat of the conductor averaged over its cross-section. The calculated enthalpy margins are 2.3 × 10^7 J/m^3 at 15 K, 2.1 × 10^7 J/m^3 at 30 K, and 1.5 × 10^7 J/m^3 at 45 K. The energy values of thermal disturbance causing quench in the experiments and the enthalpy margin suggest that the initial temperature does not considerably impact the energy that induces quench at low temperatures.

7.4 Critical Current of Coated Conductor/Magnetic Field

The critical current of a coated conductor varies depending on the manufacturing method and operating temperatures/external magnetic fields. In this research, conductors manufactured by SuperPower Inc. and Fujikura Ltd. are used to study the quench/thermal runaway detection and protection at certain temperatures/fields. To determine whether the short-sample experimental results are applicable to real coils considering critical current, quench detection and protection experiments are implemented using samples with different critical currents (varied by external magnetic fields).

Figure 7.3 shows the hot-spot temperature and current waveforms of a sample when its critical currents are varied by applying different magnetic fields (243 A at 2 T and 485 A at 0.631 T). Although the 485-A critical current is approximately equal to twice of 243 A, significant differences in the hot-spot temperature waveforms at different critical currents are not observed.

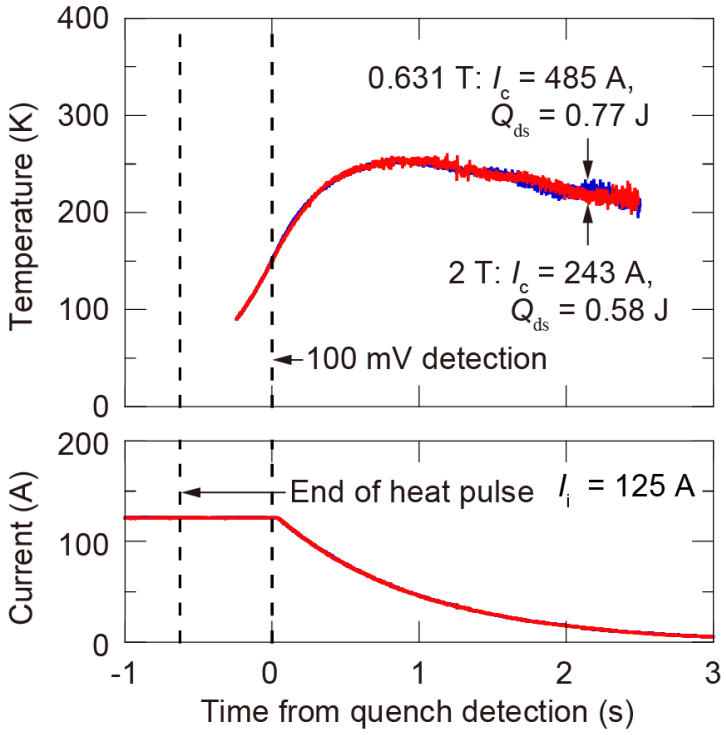

Figure 7.3 Hot-spot temperature and current waveforms when I_c = 485 A (I_{op}/I_c = 0.26, B = 0.631 T) and I_c = 243 A (I_{op}/I_c = 0.51, B = 2 T) (T_i = 30 K, v_{th} = 100 mV, t_d = 100 ms, and τ = 1 s; due to insufficient I_c–T data at 0.631 T, temperature is calculated from 90 K, which is considered as exceeding critical temperature; two quench shots implemented with same short sample) [7.1] © 2019 IEEE.

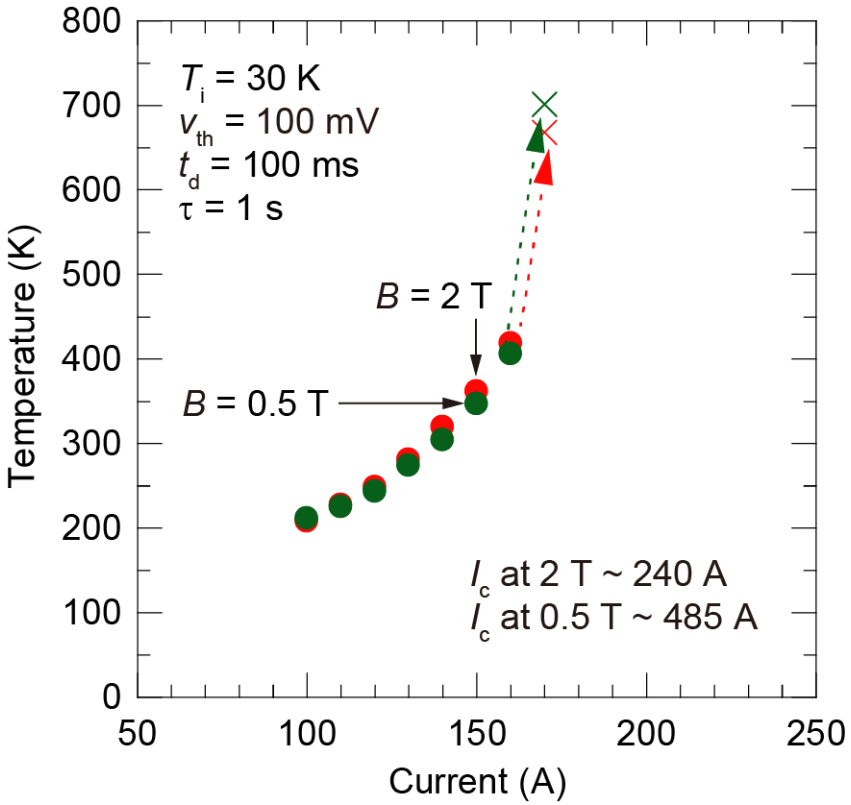

Figure 7.4 Maximum hot-spot temperatures vs operating currents when I_c = 240 A (B = 2 T) and I_c = 485 A (B = 0.5 T). Closed symbols represent quench not leading to degradation, and crosses represent quench leading to degradation; different colors represent various critical currents (different samples) [7.1] © 2019 IEEE.

The operating current was increased, and the hot-spot temperature was measured. For the experiments, two samples, whose critical currents were 240 A at 2 T and 485 A at 0.5 T, were used. As shown in Figure 7.4, the maximum hot-spot temperatures, which are virtually unaffected by the critical current, increase with the operating current. No degradation was observed below 160 A, but both samples degraded at 170 A.

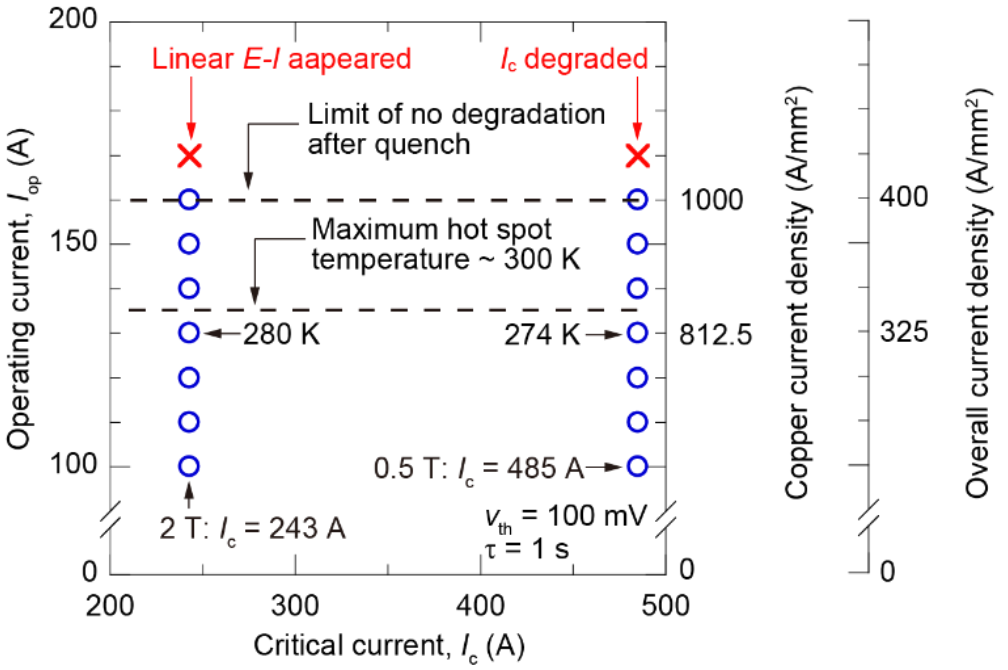

Figure 7.5 Quench experiments at different critical currents when detection voltage and time constant of current decrease are fixed at 100 mV and 1 s, respectively. Circles represent quench not leading to degradation, and crosses represent quench leading to degradation [7.1] © 2019 IEEE.

In Figure 7.5, the operating currents (represented by circles and crosses) utilized in the quench experiments are plotted against the critical current, which is varied by changing the applied magnetic field (τ = 1 s and v_{th} = 100 mV in all quench experiments). Notably, the critical current does not affect I_{nd} and I_{300K}. This is reasonable considering that the hot-spot temperature is determined by the copper current density that governs Joule heating.

7.5 Chapter Summary

The experimental results suggest that thermal disturbance power, initial temperature, and critical current do not affect the maximum hot-spot temperature using the conventional quench detection and protection method. In other words, the factors that do not affect Joule heating must not also affect the protectable conditions (*i.e.*, conditions under which no degradation appears after quench/thermal runaway) using the conventional quench detection and protection method.

[References]

[7.1] X. Luo, S. Inoue, and N. Amemiya, “Experimental study on quench detection and protection conditions of copper-stabilized coated conductors using short samples,” *IEEE Trans. Appl. Supercond*., vol. 29, no. 8, Dec. 2019, Art. no. 4703511.

[7.2] X. Luo, S. Inoue, and N. Amemiya, “One-dimensional quench analyses combined with quench experiments of conduction-cooled RE-123 coated conductors,” International Symposium on Superconductivity 2019, Kyoto, Japan.

Chapter 8 Conclusion

The REBCO coated conductor is expected to be the suitable conductor for high-temperature superconducting magnets because its critical current density is considerably higher than those of common LTSs (e.g., Nb–Ti and Nb_3Sn) at the same operating temperature and external magnetic field. However, quench/thermal runaway detection and protection can be more difficult in superconducting magnets wound with REBCO coated conductors than those wound with LTSs because of the slow NZPV. Some novel quench/thermal runaway detection methods (such as Rayleigh-backscattering interrogated optical fibers) or protection methods (such as non-insulation winding coils) are proposed. However, these methods are complex or only applicable to certain types of superconducting magnets wound with REBCO coated conductors. The conventional quench/thermal runaway detection and protection method, *i.e.*, detecting quench using VTs and dumping the stored energy in an external dump resistor, is an attractive option because it is simple, and its hardware is well-established. However, the applicability of the conventional quench/thermal runaway detection and protection method to the superconducting magnet wound with REBCO coated conductor was not clarified well. To apply the conventional quench/thermal runaway detection and protection method to a superconducting magnet wound with REBCO coated conductor, the protectable conditions (i.e., conditions under which no degradation appears after quench/thermal runaway), which are necessary to design the quench/thermal runaway detection and protection system in a superconducting magnet, are studied.

In this study, short-sample experiments were conducted to study the quench/thermal runaway detection and protection instead of burning expensive superconducting coil. To simulate the quench/thermal runaway detection and protection processes in superconducting magnets, an FPGA module was used to monitor the voltage in short samples and control the power supply. In this case, quench is detected by voltage, and protection is provided by decreasing the operating current exponentially (simulating the current decay using an external resistor). The hot-spot temperature during the protection process, which directly affects protection, is calculated based on voltage and the temperature–resistivity relationship of copper and current-sharing model. The fast-turnaround short-sample experiments enabled the collation of data on hot-spot temperatures under various conditions in addition to the conditions for successful/failed quench detection and protection.

The quench in a superconducting magnet is caused by thermal disturbances, such as the friction induced by electromagnetic force, which cannot be completely avoided. To simulate the quench induced by local and transient thermal disturbances, a resistive heater was used to initiate quench. The experimental results of the short-sample experiments suggest the applicability of conventional quench detection using voltage and protection using a dump resistor to superconducting magnets wound with REBCO coated conductor. This is possible if the appropriate time constant of current decay (depending on the coil inductance and resistance of external resistor) and voltage threshold for quench detection are selected.

The thermal runaway in a superconducting magnet initiates at the weakest point (low critical current). Because of local defects during manufacturing and the magnitude/detection of the magnetic field, the critical current distributes along the conductor in superconducting magnets. When unexpected temperature rise occurs due to the cooling system or heating by radiation (such as that in the case of accelerators or fusion magnets), the critical current decreases, and thermal runaway may initiate at the weakest point. The thermal runaway in a superconducting magnet was experimentally studied from two viewpoints: (a) the initiation of thermal runaway and (b) the detection of and protection from thermal runaway.

The initiations of thermal runaway in monofilament and multifilament coated conductors were compared experimentally. The effect of additional Joule heating in multifilament coated conductors was not remarkable. To determine the applicable quench/thermal runaway detection and protection method against thermal runaway, short-sample experiments were conducted using the monofilament and multifilament coated conductors with local defects (simulating the weakest point in a superconducting magnet). The thermal runaway detection and protection experiments were implemented at various operating currents. The thresholds for protecting monofilament and multifilament coated conductors from degradation were derived by comparing the hot-spot temperatures and protectable currents. The experimental results suggest that the thresholds for successful protection against thermal runaway of monofilament and multifilament coated conductors were virtually at the same level. Furthermore, the protectable currents against thermal runaway approximated those of quench when the conventional quench/thermal runaway detection and protection method was applied.

Finally, to ascertain whether the results of the short-sample experiments can be applied to quench/thermal runaway detection and protection of a real superconducting magnet, the relevance of short-sample experiments to real coils is determined by numerical calculation and experiments considering the following perspectives: (a) transverse thermal diffusion and longitudinal thermal conduction;

(b) effect of short length; (c) degradation in a short sample and real coil. The experimental and calculated results suggest that the length of the short sample is sufficiently long to simulate a coil. The behaviors of the short sample during the protection process may be similar to those of conductors insulated with a polyimide tape in a real magnet from the viewpoint of thermal conduction. The factors that should not affect Joule heating (including heater power, initial temperature, and critical current/magnetic field) were discussed experimentally; these should not affect the maximum hot-spot temperature. Accordingly, the results of the quench/thermal runaway detection and protection processes using short samples can be relevant to the protection of a real superconducting magnet using the conventional quench/thermal runaway detection and protection method.

The results of this study indicate that the conventional quench/thermal runaway detection and protection method is applicable to a superconducting magnet wound with REBCO coated conductors. The conditions for providing successful protection could be estimated using short samples in experiments instead of burning expensive coils. These experiments provide guides to solve the problem of designing the protection system of a superconducting magnet wound with REBCO coated conductors. Although this study focused on the conditions for providing protection against quench/thermal runaway using the conventional detection and protection method, other detection and protection methods can be evaluated using a similar setup. Moreover, short-sample experiments can be conducted not only to study the protection of magnets wound with REBCO coated conductors but also to investigate the characteristics of various conduction-cooled superconductors.

The discussion of this thesis focus on the quench and thermal runaway of a single straight coated conductor. Other conductors, such as spiral conductors (coated conductor wound around a metal core), are proposed for large-current applications (*e.g.*, high-energy accelerator system). However, their characteristics as regards quench/thermal runaway detection and protection remain unclear. The experimental methods and ideas in the short-sample experiments are anticipated to be beneficial to the study of such conductors and advance the potential use of REBCO coated conductors.

● Journal Papers

■ Publications of the contents of this thesis

1. X. Luo, S. Inoue, and N. Amemiya, "Experimental study on quench detection and protection conditions of copper-stabilized coated conductors using short samples," *IEEE Trans. Appl. Supercond*., vol. 29, no. 8, Dec. 2019, Art. no. 4703511.
2. X. Luo, S. Inoue, N. Amemiya, "Quench experiments of conduction-cooled coated conductors with various copper-stabilizer thicknesses," *IEEE Trans. Appl. Supercond*., vol. 30, no. 4, Jun. 2020, Art. no. 4700705.
3. X. Luo, Y. Zhao, Y. Sogabe, H. Sakamoto, S. Yamano, and N. Amemiya, "Thermal runaway of conduction-cooled monofilament and multifilament coated conductors," *IEEE Trans. Appl. Supercond*., vol. 32, no. 4, Jun. 2022, Art no. 6600609.

■ Others

1. N. Amemiya, S. Inoue, X. Luo, Y. Sogabe, S. Takayama, Y. Ishii, T. Ogitsu, Y. Iwata, K. Noda, and M. Yoshimoto, "Test of Cryocooler-Cooled RE-123 Magnet on HIMAC Beam Line in S-Innovation Program," *IEEE Trans. Appl. Supercond*., vol. 29, no. 5, Jan. 2019, Art. no. 4600305.

● International Conference

1. X. Luo, S. Inoue, Y. Sogabe, and N. Amemiya, "Experimental study on quench protection conditions of copper-stabilized coated conductors using short sample pieces," Applied Superconductivity Conference 2018, 2LPo2F-06, Seattle, the U.S.
2. X. Luo, S. Inoue, and N. Amemiya, "One-dimensional quench analyses combined with quench experiments of conduction-cooled RE-123 coated conductors," International Symposium on Superconductivity 2019, APP1-2, Kyoto, Japan.
3. X. Luo, S. Inoue, and N. Amemiya, "Relevance of current density in copper stabilizer for quench protection of coated conductors," International Conference on Magnet Technology 26, Tue-Mo-Po2.10-03, Vancouver, Canada.
4. X. Luo, T. Shen, X. Wang, N. Amemiya, H. Higley, and T. Ogitsu, "A fast turnaround experimental and modeling platform for investigating quench

initiation and detection of REBCO coated conductors for high-field magnet applications," International Conference on Magnet Technology 26, Wed-Mo-Po3.11-03, Vancouver, Canada.
5. X. Luo, N. Amemiya, X. Wang, T. Shen, T. Ogitsu, J. D. Weiss, and D. van der Laan, "Quench experiments of conduction-cooled CORC® cable during quench detection and protection procedure," Applied Superconductivity Conference 2020, Wk1LPo2A-03, online.
6. X. Luo, Y. Zhao, T. Hirano, and N. Amemiya, "Experimental study on quench and protection characteristics of coated conductor spirally wound on metal core," International Symposium on Superconductivity 2020, AP6-3, online.
7. X. Luo, Y. Zhao, G. Xu, Y. Sogabe, and N. Amemiya, "Effect of core on quench protection of spiral coated conductors," The 15th European Conference on Applied Superconductivity, EUCAS2021-247, online.
8. X. Luo, Y. Zhao, G. Xu, Y. Sogabe, and N. Amemiya, "Thermal runaway experiments of copper-plated multifilament coated conductors," The 15th European Conference on Applied Superconductivity, EUCAS2021-252, online.
9. X. Luo, Y. Zhao, Y. Sogabe, and N. Amemiya, "Comparison of protection characteristics of copper-plated multifilament and monofilament coated conductors subject to laterally-uniform thermal disturbances," International Symposium on Superconductivity 2021, AP8-9, online.

● Domestic Conference

1. 羅熙捷　井上覚　曽我部友輔　雨宮尚之，短尺線材を用いた模擬的実験による薄膜線材で巻かれた伝導冷却マグネットのクエンチ保護についての検討（2），2018 年春季低温工学・超電導学会，3B-a05，May 2018.
2. 羅熙捷　井上覚　曽我部友輔　雨宮尚之，短尺線材を用いた模擬的実験による局所的劣化に起因する伝導冷却薄膜線材マグネットのクエンチに対する保護の検討，2018 年秋季低温工学・超電導学会，3C-a10，Nov. 2018.
3. 羅熙捷　井上覚　雨宮尚之，過渡的・局所的擾乱により発生したクエンチに対して伝導冷却薄膜線材コイルを保護可能な検出電圧・電流減衰時定数の実験的調査，2019 年春季低温工学・超電導学会，1A-a04，May 2019.
4. 羅熙捷　王寧　陳妙鑫　曽我部友輔　雨宮尚之，多芯化薄膜高温超伝導線材の短い結合時定数を測定するための磁化損失測定システムの改良，2020 年春季低温工学・超電導学会，1P-p06，Jul. 2020.
5. 羅熙捷　趙一帆　雨宮尚之，伝導冷却された CORC®導体の劣化しないクエンチ検出・保護条件の実験的研究，2020 年秋季低温工学・超電導学会，1A-p07，Dec. 2020.
6. 羅熙捷　趙一帆　平野貴之　曽我部友輔　雨宮尚之，低交流損失・ロバスト高温

超伝導ケーブル（SCSC ケーブル）の研究開発の初期結果 (7)：スパイラル導体のコアがクエンチ保護に与える影響, 2021 年春季低温工学・超電導学会, 1A-p07, May. 2021.

● Awards

1. The 18th Young Scientists Lecture on Cryogenic and Superconductivity, Young Scientist Encouragement Prize of Cryogenic and Superconductivity.
   (第 18 回 低温工学・超伝導若手合同講演会　低温工学・超伝導若手奨励賞)
2. Cryogenics and Superconductivity Society of Japan, Awards for Excellent Presentation in 2020.
   (低温工学・超電導学会　令和 2 年度　優良発表賞)

● Acknowledgement

First, I would like to thank Prof. Naoyuki Amemiya, Associate Prof. Itsuhiro Kakeya, and Senior Lecturer Takeshi Mifune for their supervision during my Ph.D. course. I also wish to express my gratitude to the members of Prof. Amemiya's group, specifically Assistant Professor Yusuke Sogabe, Dr. Yang Li, Guangwei Xu, and Yifan Zhao, for their cooperation in the conduct of experiments and numerical calculations. I want to thank Prof. Toru Ogitsu (KEK, Japan), Dr. Tengming Shen, and Dr. Xiaorong Wang (LBNL, the U.S.) for their advice regarding my research. I am grateful to Satoshi Yamano (SuperPower Inc.) and Hisaki Sakamoto (Furukawa Electric Co.) for providing the samples.

I want to express my special thanks to Tatsuya Ikeda and Satoru Inoue for their cooperation during the development of the measurement method. Finally, I wish to express my gratitude to my family and friends for their moral support and warm encouragement.